

Lehrstuhl für Fluidmechanik und Prozessautomation  
der Technischen Universität München

## Mechanical Effects in Human Oral Texture Perception

**Julia Annette Straßburg**

Vollständiger Abdruck der von der Fakultät Wissenschaftszentrum Weihenstephan für Ernährung, Landnutzung und Umwelt der Technischen Universität München zur Erlangung des akademischen Grades eines

**Doktor-Ingenieurs (Dr.-Ing.)**

genehmigten Dissertation.

Vorsitzender: Univ.-Prof. Dr. rer. nat. Michael Schemann

Prüfer der Dissertation:

1. Univ.-Prof. Dr.-Ing. habil. Antonio Delgado,  
Friedrich-Alexander-Universität Erlangen-Nürnberg
2. Univ.-Prof. Dr.-Ing. Eberhard Geiger
3. Univ.-Prof. Dr. rer. nat. techn. Dietrich Knorr,  
Technische Universität Berlin (schriftliche Beurteilung)

Die Dissertation wurde am 04.08.2006 bei der Technischen Universität München eingereicht und durch die Fakultät Wissenschaftszentrum Weihenstephan für Ernährung, Landnutzung und Umwelt am 02.11.2006 angenommen.



To my parents



## Acknowledgments

I would like to thank the "Food Structuration" group at the Nestlé Research Center (NRC), Lausanne, who made me feel very welcome and with whom I shared a lot of precious moments.

Of course I also want to thank all the other colleagues and friends who participated in the sensory studies and were willing to do the unusual task of sucking on Teflon films. In this context I also would like to thank the suppliers of the films, i.e. Klöckner Pentaplast, GE Plastics, and DuPont Research, who generously provided me with the material and offered lots of patience and understanding when I only wanted an A4 sheet of materials, which are normally sold in tons. In this context Igor Bodnar from Nizo Food Research has to be mentioned because he invented the whey protein films, who finally made the confirmation of my hypothesis possible.

Furthermore, at the Nestlé Research Center I owe many thanks to Nicolas Antille, who supported me with statistical knowledge for the trial set-up and evaluation. Many thanks also goes to Lars Lundquist, who always had an open door for me and never felt offended when I abused his packaging materials, i.e. I never ever wrapped anything in them.

Moreover I am very thankful to Frederic Ougey from the workshop, who has not only once helped me with an "emergency modification" of a piece of equipment. This is valid in the same way for Jorge Fernandez but for the IT support. Thanks!

Besides that I would like to thank Colin Servais, who helped me with enriching and critical discussions but also eye-opening experiments (i.e. squeezing my tongue in a texture analyzer!) especially at the beginning of my project. Thank you also to Alexandre Romoscanu from whom I received support for the modeling of the disk bending and who also got me started on Mathematica.

Furthermore I would like to thank Professor Michael Schemann for taking the responsibility of the thesis committee and the conduction of all formalities; also Professor Dietrich Knorr and Professor Eberhard Geiger for their participation in the thesis evaluation. Great thanks also goes to Professor Karl Sommer for his spontaneous engagement in the thesis defense.

I would also like to thank Johanna Claude, who “forced” and taught me to speak French and with whom I really had a good time in the lab before she decided to emigrate to the US, and my colleagues Roberto King and Elisabeth Pilloud, who always had a supportive smile and encouraging words when things were rather gloomy.

Many thanks I also owe to Heribert Watzke, who gave me the possibility to carry out this work in his department. He always made it possible for me to have the necessary resources and possibilities and trusted me, especially when I needed it the most...

An enormous thank you goes to my colleagues and very good friends Jan Engmann and Hanjo Limbach: Jan always had a critical eye, helpful advice, a lot ! of patience, and a great way of explaining things. He hung in the whole story with me until the very end (a really, really big thank you for that!). Hanjo is the other part of the Mathematica and LaTeX “helpline”, who assured that things did not become “too German” and that it sometimes helps just to take things easy, for which I want to thank him a lot. Ihr zwei, ich weiss, es (ich) war nicht immer einfach, aber ich weiss wirklich sehr zu schätzen was Ihr für mich all die Zeit getan habt!!!

I am of course very thankful to my supervising professor Antonio Delgado, who at the very beginning made the decision to conduct this project with me. He gave me the necessary guidance from the academic side and helped me to complete all administrative hurdles.

Deep thanks goes to my “part-time” supervisor Christoph Hartmann, who from the very beginning was very interested and motivated for the project even when he was exposed to certain geographic “fluctuations”. He was always there for me as a helpful and critical guidance as well as a friend, who always knows the right thing to say. Inch’allah, Mohammed! Aywa?

The greatest thanks I owe to Adam Burbidge, my full-time supervisor on the spot, who always gave me all his support and especially patience and encouragement. Although it was not always easy (since with him I jumped into a field, which was really his but far away from my world) I am glad he forced me to learn the things I learned during this time. He taught me how to sometimes take a different look at things and to defend what you see (this resulting in being a bit of a “rebel” from time to time :-)). I will never forget all the great discussions we had. Friday facts such as weather frogs, tiger ducks, and the maggi plant are only a few precious examples. “Anyway**S**” ... right, Adam?

I would also really like to thank my friends and family for being understanding, encouraging and supportive throughout this time.

I am grateful for the support of my thesis, funded in the framework of the Nestlé Research Center PhD scholarship.

# Contents

<b>Kurzfassung</b>	<b>x</b>
<b>Abstract</b>	<b>xi</b>
<b>List of notations</b>	<b>xiii</b>
<b>1 Introduction: Mechanoreception in the human mouth</b>	<b>1</b>
1.1 Motivation of the work . . . . .	1
1.2 Former studies and the associated problems . . . . .	3
1.3 Complexity of the perception of texture in comparison with taste . . . . .	6
1.4 Direction and aim of the project . . . . .	7
1.4.1 Geometrical size sensitivity . . . . .	10
1.4.2 Perception of suspensions . . . . .	10
<b>2 Geometrical resolution limits in the human mouth</b>	<b>15</b>
2.1 Materials & methods . . . . .	16
2.1.1 Sensory test procedure . . . . .	16
2.1.2 Subjects . . . . .	16
2.1.3 Materials (films) . . . . .	17
2.1.3.1 Thinning of standard films . . . . .	18

2.1.3.2	Whey protein-glycerol films (WP/G) . . . . .	19
2.1.4	Geometrical sensitivity experiments . . . . .	20
2.1.4.1	Introductory trials for determination of the feasibility . . . . .	20
2.1.4.2	Thickness determination (main study) . . . . .	24
2.1.5	Data processing . . . . .	25
2.1.6	Mathematical model . . . . .	26
2.2	Results . . . . .	34
2.2.1	Preliminary trials . . . . .	34
2.2.2	Sensitivity to thickness differences (main study) . . . . .	37
2.3	Discussion . . . . .	43
<b>3</b>	<b>Perception of suspensions by the tongue-palate system (model)</b>	<b>51</b>
3.1	Introduction to the mathematical model . . . . .	51
3.2	Mathematical methods . . . . .	57
3.2.1	Newtonian fluid between parallel moving plates: <i>Stefan model</i> . . . . .	58
3.2.2	Point force: <i>Faxen's first law</i> . . . . .	65
3.2.3	Point force (particle) in a fluid: <i>Green functions</i> . . . . .	70
3.2.3.1	Free space Green function . . . . .	71
3.2.3.2	Bounded Green function . . . . .	73
3.2.4	Particular consideration of the two Green functions for a particle above the origin . . . . .	76
3.2.4.1	Free space Green function . . . . .	76
3.2.4.2	Bounded Green function . . . . .	80
3.2.5	Superposition of the estimated stresses . . . . .	82
3.2.5.1	Stress superposition for the free space situation . . . . .	82

3.2.5.2	Stress superposition for the bounded situation . . . . .	86
<b>4</b>	<b>Experimental validation of the fluid mechanical model</b>	<b>93</b>
4.1	Introduction to the experiments . . . . .	93
4.2	Materials & methods . . . . .	94
4.2.1	Experimental set-up . . . . .	94
4.2.2	Tekscan pressure sensor . . . . .	95
4.2.3	Fluid and particle materials . . . . .	98
4.2.4	Technical improvements of the system . . . . .	99
4.2.5	Calibration & equilibration . . . . .	100
4.2.6	Trial procedure . . . . .	109
4.3	Trials . . . . .	110
4.3.1	Dimensional analysis . . . . .	111
4.4	Results & discussion of the trials . . . . .	116
4.4.1	Equilibration and calibration trials (A - C1) . . . . .	116
4.4.2	Squeeze flow trials (1 - 11) . . . . .	118
<b>5</b>	<b>Conclusions and future aspects</b>	<b>129</b>
<b>A</b>	<b>Mathematica code for the fluid mechanical model</b>	<b>140</b>
<b>B</b>	<b>MATLAB code for the theoretical equilibration</b>	<b>153</b>
<b>C</b>	<b>Specification of the films</b>	<b>169</b>
<b>D</b>	<b>Elastic modulus of flexible films</b>	<b>171</b>
	<b>References</b>	<b>183</b>

## Kurzfassung

Das Kernziel dieser Arbeit war es, mehr Einsicht in die Prozesse der Texturwahrnehmung zu gewinnen und diese letztendlich soweit zu verstehen, wie es derzeit für Geschmackswahrnehmung der Fall ist.

Hierfür wurde zunächst im ersten Teil der Arbeit die Sensibilität der Wahrnehmung bezüglich Scheibchen unterschiedlicher Grösse, d.h. Scheibchen im mm Bereich bezüglich des Durchmessers und  $\mu\text{m}$  Bereich für die Dicke, im Mund zwischen Zunge und Gaumen als paarweiser Vergleich evaluiert. Nachdem die Sensibilität bestimmt worden war, d.h. 1 mm für Unterschiede im Durchmesser und 25  $\mu\text{m}$  in der Dicke, wurden die Erkennungsmechanismen untersucht.

Aufgrund eines unerwarteten unsicheren Bereiches, in dem die Sensibilität bezüglich der Dicke kleiner als 25  $\mu\text{m}$  ist, wurde eine Hypothese über die Existenz zweier unterschiedlicher von der Scheibendicke und -härte abhängiger Erkennungsmechanismen aufgestellt: Durchbiegen für dünne und Eindrücken in die Zunge für dicke Scheiben. Es wurden mathematische Modelle entwickelt und verifiziert.

Im zweiten Teil der Arbeit wurde die Empfindung von Griessigkeit in flüssigen Lebensmitteln untersucht. Da auf Zunge und Gaumen nur Drucksensoren, aber keine texturspezifischen Rezeptoren existieren, wurde angenommen, dass das Gefühl von Griessigkeit auf Spannungsfeldschwankungen zurückzuführen ist. Diese werden durch in der Flüssigkeit enthaltene Partikel verursacht. Ein theoretisches fluidmechanisches Modell wurde diskutiert und danach experimentell verifiziert.

Die Evaluierung des flüssigen Lebensmittels wurde als Quetschströmung zwischen Zunge und Gaumen dargestellt. Zu Beginn wurden Quetschströmungen von reinen Fluiden untersucht, deren Druckverteilung mit Hilfe der Steffan-Gleichung berechnet werden kann. Die von den Partikeln verursachte Punktkraft wurde mit Hilfe von Faxens Gesetz beschrieben. Die Green Funktionen schliessen diese Punktkraft ein, so dass das resultierende Geschwindigkeits- und Spannungsfeld im Fluid mit Partikel bestimmt werden können. Ziel war es, die durch das Partikel verursachten Druckfeldvariationen im mechanischen Modell aufzuzeigen. Das Modell bestand aus einem blattförmigen Tekscan Drucksensor, der an der unteren von zwei parallelen Platten angebracht war, und so die Variationen im Normaldruck messen konnte. Der Sensor wies jedoch eine geringere als die vom Hersteller angegebene Auflösung auf, sodass die erwähnten Störungen des Druckfelds nicht registriert werden konnten. Im Falle positiver Versuchsergebnisse wäre es möglich, mit Hilfe der dargestellten Dimensionsanalyse Rückschlüsse über die Druckfeldvariationen im Mund und damit die Empfindung von Sandigkeit zu ziehen.

## Abstract

The main aim of this work was to gain more insight into the processes of human oral texture perception with the final aim being to understand texture perception to the same extent that taste perception has been understood today.

As a first step to this end the geometrical resolution limits for objects in the human mouth were determined. For this, disks of varying diameter (in mm range) and thickness (in  $\mu\text{m}$  range) were evaluated in pair comparisons, where the larger respectively thicker sample had to be identified.

Possible detection processes were discussed, and a hypothesis about the existence of two different detection processes, i.e. bending for thin disks (below  $120\ \mu\text{m}$ ) and impressing into the tongue for thick discs (above  $200\ \mu\text{m}$ ), was established. These limiting values leave an undetectable range in which both processes fail. The findings are consistent with the anatomical and neurological knowledge. Mathematical models were applied. The hypothesis about the existence of two detection processes was validated using softer materials in order to show that the insecure range disappears because bending is possible even for thicker discs.

The perception of grittiness was the focus of the second part of this project. Since there are no specific texture receptors it was assumed, that perception of grittiness in liquid foods is due to the perception of stress field variations in the fluid caused by the presence of particles, which are of the same order of magnitude as the previously determined discrimination limit for the disks ( $25\ \mu\text{m}$ ). These stress field variations were investigated with a theoretical fluid mechanical model and then verified experimentally.

The model assumed tongue and palate as two parallel plates, which by the means of squeeze flow evaluate the (particle containing) fluid. The pressure form of the Stefan equation was used to describe pure squeeze flow. The force acting on a particle in the fluid was calculated with the help of Faxen's law, before the stress and velocity field variations were determined by the means of the Green functions. Once these stress field variations had been determined the aim was to show these variations experimentally in a particle containing squeeze flow by attaching a sheet form pressure sensor with a resolution of  $1\ \text{mm}$  (the same spacing as the mechanoreceptors in the mouth) to the bottom plate. Unfortunately the sensor did not have the resolution claimed by the supplier and despite calibration and equilibration no disturbances due to the particle could be registered. With an appropriate sensor and the presented dimensional analysis conclusions about the stress field perception in mouth are possible.

## Publications, Posters proceedings, Oral presentations

### Publications

- Strassburg, J., Burbidge, A., Hartmann, C., Delgado, A., Geometrical resolution limits in the oral cavity, *Journal of Biomechanics* (submitted)
- Strassburg, J. Burbidge, A. Hartmann, C., Delgado, A., Mechanisms and sensitivity of object dimensional perception through human touch, *Journal of Comparative Physiology A* (submitted)
- Strassburg, J., Ziegler, G., Beckett, S., When are chocolates really finished?, *New Food*

### Oral Presentations and Proceedings

- Strassburg, J., Burbidge, A., Servais, C., Hartmann, C., Delgado, A., “Mechanics of oral texture perception”, *MS 2004, 1st International Workshop on Materials and Sensations*, 27-29 October 2004, Pau, France  
(Oral presentation & proceedings)
- Strassburg, J.A., Burbidge, A.S., Hartmann, C., Delgado, A., “Sandigkeitsempfindung im Mund - Texturempfindung in der Mundhöhle”, *VDI-GVC Fachausschusssitzung "Lebensmittelverfahrenstechnik"*, 7-9 March 2005, Berlin, Germany  
(Oral presentation)
- Strassburg, J., Burbidge, A., Hartmann, C., Delgado, A., “Geometrical resolution limits in the human mouth”, *International Symposium on Food Rheology and Structure ISFRS*, 19-23 February 2006, Zurich, Switzerland  
(Oral presentation & proceedings)

# List of notation

## Symbols

### Roman

$a$	sphere radius (Faxen's law)	m
$A$	point on the disk	
$b$	offset between coordinate systems (free space Green function)	
$b$	intersection with the y-axis (bounded Green function)	m
$b$	probability to obtain $x$ correct answers (data analysis)	
$B$	probability to obtain $x$ or more correct answers (data analysis)	
$B$	point on the axis through the origin (disk modeling)	
$d$	plate distance	m
$\dot{d}(t)$	plate velocity	m/s
$D$	flexural rigidity	N m <sup>2</sup>
$E$	elastic modulus	Pa
$F$	force	kg/m s <sup>2</sup>
$h$	thickness of the disk (disk trials/modeling)	m
$h$	particle distance from the plate surface (bounded Green function)	m
$H_0$	null hypothesis	
$H_1$	alternative hypothesis	
p-value	measure of evidence which exists against the null hypothesis	
$m$	particle mass	kg
$M_r$	momentum acting along circumferential sections of the disk	Nm
$M_t$	momentum acting along diametral section of the disk	Nm
$N$	the number of trials (panelists x repetitions)	
$p$	hydrostatic pressure (Green functions)	Pa
$P$	fluid pressure (Stefan model)	Pa
$P(r)$	distributed load in dependence of the radius (disk modeling)	Pa
$P(0)$	distributed load at the center of the plate (disk modeling)	Pa
$P(R_0)$	distributed load at the edge of the disk (disk modeling)	Pa
$Q$	applied load on an element of a disk (disk modeling)	
$r$	radial distance (disk trials and cylindrical polar coordinates)	m
$r$	position of the real particle (squeeze flow modeling)	

$R$	position of the image particle (squeeze flow modeling)	
$R_0$	radius of the disk (disk trials/modeling)	m
$R_C$	radius of curvature	m
$R_P$	plate radius (Stefan model)	m
$SP$	sample point	
$t$	time	s
$v$	velocity	m/s
$w$	deflection of the disk in dependence of the radius	m
$x$	the number of correct answer in the data	
$X$	random variable representing number of correct answers	

## Greek

$\alpha$	angle of segment of a circle	°
$\delta_{ij}$	Kronecker delta	
$\eta$	dynamic viscosity	Pas
$\dot{\gamma}$	shear rate	1/s
$\lambda$	deflection at the center of the disc	m
$\nu$	kinematic viscosity (squeeze flow)	m <sup>2</sup> /s
$\nu$	Poisson's ratio (disk modeling)	
$\rho$	density	kg/m <sup>3</sup>
$\sigma_{ij}$	total stress tensor	
$\tau_{ij}$	deviatoric stress tensor	
$\varphi$	angle between normals on a disk surface	

## Dimensionless Numbers

Eu	Euler number
Re	Reynolds number
$\varepsilon$	scaling parameter $\frac{d}{R_P}$

## Abbreviations

no.	number
FEP	fluorocarbon film, Teflon
FM	fluid mechanical
ML	MATLAB
MRI	magnetic resonance imaging
PCI	peripheral component interconnect
PET	polyethylene terephthalate
PSP	parallel steel plates
rel	relative (e.g. velocity)
WPI	whey protein isolate
2D	two-dimensional
3D	three-dimensional

## Sub/superscripts

0	disk radius
C	curvature of the palate
fl	fluid
g	gravitational
r	circumferential direction (disk trials)
r	direction in cylindrical polar coordinates
t	diametral direction
$\boldsymbol{x}$	vector $\boldsymbol{x}$
$\theta$	direction in cylindrical polar coordinates
P	plates (in the Stefan model)
p	particle
*	dimensionless numbers
$i$	vectorial index
$j$	vectorial index
$ij$	tensorial index
$k$	differential index
$q$	differential index
$r$	radial direction in cylindrical polar coordinates
rel	relative (e.g. velocity)
$z$	direction in cylindrical polar coordinates



# Chapter 1

## Introduction: Mechanoreception in the human mouth

### 1.1 Motivation of the work

Texture evaluation of foods, be these liquid or solid, is a matter of routine in food quality control and is carried out with the help of a sensory panel or instrument. Therefore, the quality of the correlation between sensory impression and objective measurements is of great importance. The term “texture” is rather vague, but commonly refers to all the mechanical, geometrical, and surface attributes of a product perceptible by means of the mechanical, tactile, and where appropriate, visual and auditory receptors (Association Francaise de Normalisation, 1995a). Due to the multi-parameter nature of texture Szczesniak (2002) suggests consideration and evaluation on molecular, microscopic and macroscopic scales. This complicates the characterization even further. For this work only the mechanical and geometrical attributes, i.e. those related to the reaction of the product to stress and those related to the size, shape, and arrangement of particles within a product, will be considered. Texture can either be evaluated by sensory or instrumental analysis, whereas the latter is known as the more “objective measurement”. From the term “objective” it should not be concluded that the instru-

ments available allow for an absolute measurement of the mechanical stress. Objective in this sense refers to the repeatability, which is usually more accurate for machines than for human beings concerning sensory matters since factors such as learning, personal preferences, or varying performance are not relevant, and hence, there are less variations in the measurement system. According to Hiiemae (2004) there are several reasons why an objective measurement is more advantageous than a sensory test with a panel. Among others this author refers to lower cost, shorter training times, improved flexibility, reduced ambiguity in the results, and little or no need for statistical interpretation. In addition to this the results are culturally and individually independent, which permits international standardization (Bourne et al., 2002). For this reason the prediction of sensory impression by the means of measurements would be very advantageous (Corradini et al., 2001). Understanding what makes a product texturally desirable and identification of the negative aspects of texture would be useful in the development of new and improvement of existing products (Yates et al., 2001).

Textural perception of solid and liquid foodstuffs is one area where perception of object size is of importance. Texture is mostly taken for granted and consumers do not comment on it unless expectations are violated or non-food associations are triggered. Texture is often used as an indicator for freshness (shriveled apples) or quality (lumps in a sauce) (Szczesniak, 2002), therefore its perception mechanisms have to be understood to guarantee consumer satisfaction. The importance of textural perception was shown by Wilkinson et al. (2000) who blended food products and found that only 40 % of the products could be identified correctly once they did not have their characteristic texture properties anymore. Jones et al. (1994) pointed out another reason to investigate perception of texture, particles in particular. For dental restoration it is important to know the sensitivity for roughness, this is equivalent to grittiness in the sensory field, to assure most comfort for the patient when artificial parts are added to the natural and especially smooth tooth environment.

## 1.2 Former studies and the associated problems

Generally there seem to be three ways of approaching the above mentioned problem. The first possibility is to directly establish correlations between sensory and instrumental measurements such as those that have been reported by for example De Wijk & Prinz (2005). They investigated the rheology, i.e. viscosity due to starch content, of vanilla custard desserts before correlating it with the sensory impression of “thick”, “melting”, “creamy-soft” and “rough”. Also the study carried out by Kilcast & Clegg (2002), who related particle and bubble sizes to the perception of creaminess. Earlier studies stated an inverse relation between shear thinning of a liquid and the perception of sliminess, such as the one conducted by Wood (1974). Cutler et al. (1983) tried to link thickness and dynamic viscosity. These studies all referred to liquids but similar studies have taken place for solids. Finney & Meullenet (2005) for example compared the sensory impression of hardness with instrumental compression tests, where either the resulting force (distance-controlled) or final distance (force-controlled) between the plates was determined.

When carrying out studies like those mentioned above researchers face many problems, the main one being the discrepancies between the operating conditions of texture measuring instruments and the ambient conditions present in the mouth. For example, most compression tests have been performed at cross-head speeds that are not representative of first bite velocities (Finney & Meullenet, 2005). Also the question how to simulate the high strain rates experienced in the mouth with traditional rheometers, a consideration very important with viscoelastic materials (i.e. most food products), has not yet been answered (Szczeniak, 2002). In addition, history dependent behavior, as described by Pollen et al. (2005) such as shear-thinning, is difficult to simulate with a rheometer (Cutler et al., 1983). The changes that occur for most fluid foodstuffs due to tongue movement are very irregular and hard to imitate. Furthermore, instrumental measurements of food properties are usually obtained as single events whereas texture perception is a dynamic sensory monitoring of changes made to a food by processes in the mouth (Wilkinson et al., 2000; Terpstra et al., 2005). Additionally for a long

time the influence of saliva, i.e. its diluting and mouth-coating properties, has been ignored (Bourne et al., 2002). Only fairly recent studies such as Engelen et al. (2003b) investigated salivary flow-rates as a function of the stimulus and compared the influence saliva and other liquids have on textural perception when added to liquid foods (Engelen et al., 2003a). Dunnewind et al. (2005) were among the first to carry out dynamic imitations such as repeated parallel plate compression tests. Physiological in-mouth conditions were tried to be taken into account by covering the bottom plate with a rough surface imitating the tongue and wetting it with saliva. Another mistake quite frequently made is that measurements are carried out at room temperature. Dickie & Kokini (1983) made a first step in the right direction by conducting their trials at 30.5 °C, this being the average between room and body temperature, hence, considering the warming effect of the oral cavity on the introduced food.

All these studies clearly show the complexity of perception. The perception of “juiciness” is another very hands-on example for the difficulties scientists are facing. Juiciness seems to be a fairly self-explanatory term referring to the amount of juice released upon mastication as stated by Szczesniak (2002). The author then added further dimensions such as the force with which the juice squirts out of the product, the rate of juice release, the total amount released during chewing, the flow properties of the expressed fluid, contrast in consistency between liquid and suspended cell debris, and the effect of saliva production. Despite the number of descriptive terms this was not sufficient to give a uniform definition of juiciness. This is an example for the considerable gap between the methods that food scientist use to gauge the perception of food texture in the human mouth and those which oral physiologists employ to investigate ingestion, mastication and swallowing (Lucas et al., 2004). It also shows that bulk rheology alone does not provide a complete characterization of in-mouth sensory properties (Malone et al., 2003). Another example was given by Malone et al. (2003), who proved that subjects could distinguish between 0 % and 1 % fat emulsions, whereas the measured lubricant properties were identical. An inverse situation was described by Corradini et al. (2001), who modified samples of tomato paste, yogurt, and strawberry jam and could clearly identify these modifications with instrumental analysis but not with sensory analysis. Sometimes seemingly obvious relationships

between human assessments and mechanical variables could not be found at all (Peyron et al., 1997).

As has just been demonstrated, due to the complexity of the in-mouth situation it is not easy to establish a direct connection between instrumental measurements and sensory impression. This leads to a second approach consisting of the discovery and understanding of the mechanisms and conditions of oral processing. The third approach results from the second one and relies on the prediction of sensory properties with the help of predictive mechanical models and data. First trials were made in this domain by Dickie & Kokini (1983) and more recently by Terpstra et al. (2005). Mathmann et al. (2006) also work in this field. They try to understand the perception of grittiness with the help of numerical simulations. The work is based on previous work by Nirschl (1997) and Hartmann & Delgado (2003), who also dealt with particle containing fluids.

When dealing with texture perception it has to be decided if solid or liquid foods should be in the center of interest (Bourne, 2002). Many of the studies carried out so far focused on solid foods requiring biting. Mioche et al. (2002) for example identified four different stages for the oral treatment of solids in the oral cavity, and Peyron et al. (1996) stated that the number of chewing cycles influences the duration of each cycle. Both could detect repeating patterns among test subjects. This was also proven in the framework of this work when evaluating magnetic resonance images (MRI) from the Insel Spital in Bern, Switzerland. Here the jaw and tongue movements of subjects eating a mint were recorded (Lindinger, 2003). Processes seem to be fairly well characterized for solid foods, but not for liquids. These processes require primarily tongue movements, which have proven to be difficult to monitor instrumentally without restricting masticatory movements (De Wijk et al., 2003a).

### 1.3 Complexity of the perception of texture in comparison with taste

Considering that texture and taste are usually perceived at the same time it is not surprising that, when dealing with texture perception in the oral cavity, information about taste perception is found as well. It becomes evident very quickly, many more taste investigations have taken place. It was not until the late 1950s that texture began to be looked at as a subject in itself (the way flavor had been studied for some time (Szczesniak, 2002)). The reason for the limited existence of textural studies lies in the complexity of textural perception in comparison with the perception of taste. Perception of sweet, sour, bitter and salty has long been related to specialized taste buds as can be seen for example in the work of van Ruth et al. (2001), who conducted trials in order to discover the interaction of different aroma compounds with saliva; not so for texture perception. Different types of mechanoreceptors are known (Johnson, 2001), which capture stimuli that are transmitted to the brain and processed into information (Szczesniak, 2002). Still the question remains **as to how perceived texture relates to the structures in the mouth**. It is not known if the mechanoreceptors are stimulated by force, deformation or strain energy density. It seems reasonable to assume, that texture is perceived holistically through the unconscious measurement of stresses and/or strains resulting from the manipulation of the “textured” material in the mouth while it is flowing through the mouth from the entrance of the oral cavity to the pharynx.

Therefore, texture has to be perceived by the means of flow, see Figure 1.1. This is in contrast to the perception of taste as demonstrated in the first flow schema of this Figure. For taste the process is fairly static, a molecule needs to dock to a sensor before this causes a stimulus, but no active movement is needed as it is the case for the perception of texture. Szczesniak (2002) postulated that some redundancies are felt when the food is placed in the mouth, others are just sensed when the food is deformed, therefore, for textural perception a certain movement seems necessary.

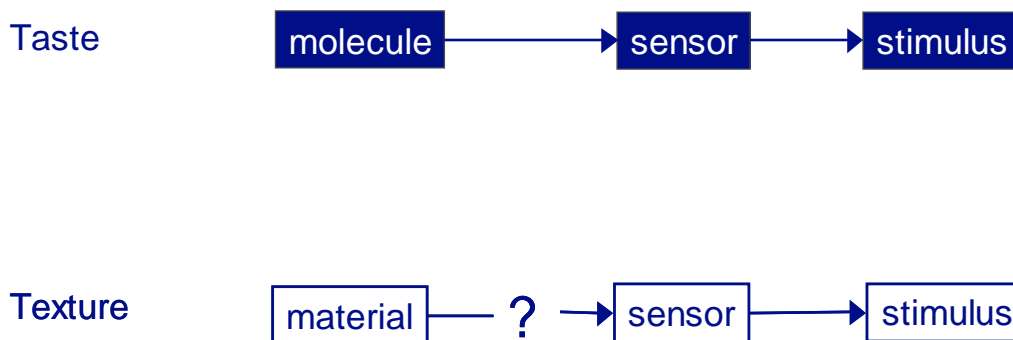


Figure 1.1: Differences in the creation of a stimulus between taste and texture perception.

## 1.4 Direction and aim of the project

The emphasis during this work is on **liquid foods** in order to avoid processes such as biting, which complicate in-mouth processing since the main goals of the process are reduction of particle size and resistance against food deformation. For solid foods a bolus is only formed and manipulated as a very last step after other more predominant processes, i.e. when perceived resistance is sufficiently low and particles are sufficiently small and lubricated (Prinz & Lucas, 1997). Apart from that, when dealing with biting and chewing, the dental situation (number and condition of dental units) and especially the differences between subjects becomes important (Hatch et al., 2000). In contrast, for the evaluation of liquids the tongue and palate are in the center of interest, although the presence of the tongue complicates the system as well due to its irregular movements and changing shape (De Wijk et al., 2003a). For the first part of this work the anatomy and physiology of the tongue, i.e. the surface of the tongue being covered with four types of papillae: filiform, fungiform, vallate, and foliate (Paulsen & Thale, 1998), is of high importance. Also the fact that the tongue is innervated by mechanoreceptors, which are also present in the glabrous skin, e.g. the hand, plays a major role. Three of the four mechanoreceptors present in the glabrous skin can be found in the oral mucosa and tongue: Merkel cells, Meissner, and Ruffini corpuscles, whereas Pacinian corpuscles are not found in the oral mucosa (Johansson et al., 1988). Some of the mechanisms can and will be transferred to the in-mouth processes.

The final idea of this work is to understand in-mouth processing during textural perception and to establish a model, which is **able to predict the textural impression of a food, which has only been physico-chemically characterized**. Alternatively, the understanding could lead to a definition of the **physico-chemical product properties to be obtained for a desirable sensory impression** (Figure 1.2). Of course considerations such as experience or variations among individuals cannot be considered in a model in a complete way but the aim should be to achieve a standardization for the aspects, which can be considered as uniform among subjects.

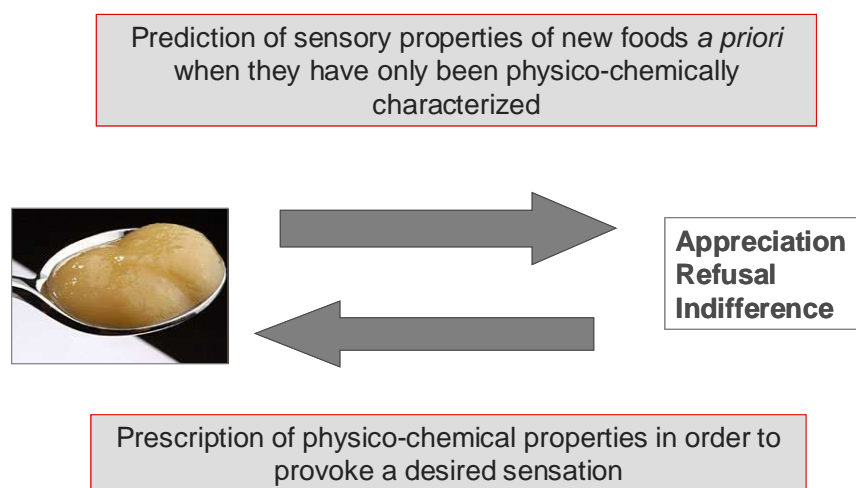


Figure 1.2: Two-fold deliverables of the thesis: 1) knowledge about textural impression without sensory evaluation based on physico-chemical characterization, 2) product design with previously assigned textural attributes.

In order to achieve the above mentioned goal, a very interdisciplinary approach, combining fluid mechanics, dentistry, biology, biomechanics, and neurology is taken. At the same time, and this is the new idea of this work, the mouth itself is considered as an instrument, such as a squeeze-flow rheometer, which needs to be characterized (Chapter 2) and evaluated (Chapter 3 and 4). This is in contrast to traditional approaches, where external machine measurements were compared with the in-mouth impression (e.g. De Wijk et al. (2003b)).

So far studies about the treatment of liquid foods in the oral cavity are rare and

have not fulfilled the aim to understand textural perception. As Guinard & Mazzucchelli (1996) stated explicitly mouth-feel properties of e.g. beverages have received comparatively little attention.

Some of the methods used, but mainly for solid food investigation, are

- Videofluorographic (VFG) (Palmer et al., 1997)
- X-ray/Cinefluorographic (CFG) recordings (Hiimae & Palmer, 1999)
- Sirognatography (attaching a magnet on the incisor tooth and following its movement) (Dove et al., 1994; Hiimae et al., 1996))
- Electromyography (EMG, recording muscle activity) (van der Bilt et al., 2001)
- Mixing of two-color chewing gums (Hayakawa et al., 1998)
- Bite mark analysis of chewed wax-wafers (Prinz & Lucas, 2001)
- Particle size analysis after chewing (Hoebler et al., 2000)
- Implementation of small strain gauges into teeth in order to record the forces exerted during chewing (Bourne et al., 2002)
- Magnetic resonance imaging (MRI) (Lindinger, 2003)

Most of these methods are too invasive: MRI measurements, despite the fact that they do not deliver results in real-time, make it very difficult to place food into the subject's mouth (Wilkinson et al., 2000). Due to the stressful testing conditions it is almost impossible to receive an objective opinion concerning the food's texture from the test subjects. Therefore, a **non-invasive method is needed**, meaning that the measurement is not supposed to take place at the same time as the textural evaluation but rather through the application of models, which have to be established. A two-fold approach is taken in order to fulfill this aim.

### 1.4.1 Geometrical size sensitivity

As a first step in this direction trials are carried out in order to determine the sensitivity to geometric differences in the mouth (Chapter 2). Disks of varying diameter, thickness, and material are introduced into blind-folded subjects' mouths for pair comparisons in order to obtain information about in-mouth size judgement and especially the detection processes. Trials for the determination of spatial resolution on the finger or hand have been carried out already by Schlereth et al. (2001) and Johansson & Vallbo (1979) but similar studies in mouth are rare. The sensitivity between finger (index) and palm is also investigated within the framework of this work in order to possibly use this system alternatively to the tongue-palate system for non food grade materials. Prinz & Lucas (1995) discovered that human beings can detect particles of 15  $\mu\text{m}$  between the teeth but not on the oral mucosa. Therefore, the idea to investigate the sensitivity between tongue and palate is a new approach. The first part of the work dealing with the size sensitivity for geometric objects creates the basis for the further investigations in Chapter 3 and 4. Here the mouth is considered as a squeeze flow rheometer and perception of suspensions ("grittiness") is looked at. The discovered particle size sensitivity and detection processes from Chapter 2 play an important role.

### 1.4.2 Perception of suspensions

For the second step, the investigation of suspensions in the mouth, the manipulation of the fluid in-mouth and the predominant flow behavior are important. Dickie & Kokini (1983) assumed that the prevalent flow type between tongue and palate is shear flow. This agrees with Cook et al. (2003) who claimed that the stimulus associated with the evaluation of fluid foods appeared to be the shear rate developed at a constant shear stress of 10 Pa (therefore a stress-controlled process). The results of Wood (1968), who carried out work in this field earlier, differ from this. He stated that the stimulus for perceived texture of hydrocolloids is a shear stress developed in the mouth at a constant shear rate of 50  $\text{s}^{-1}$  (hence a strain-controlled process). A much wider range of shear rates are operative in the mouth (10 - 1000  $\text{s}^{-1}$ ) dependent on the flow characteristics

of the food. *Low viscosity liquids* (viscosity below 0.1 Pas) are evaluated at a *constant shear stress* of about 10 Pa, while products with *high viscosity* (viscosity above 10 Pas) are evaluated at a *constant shear* rate of  $10 \text{ s}^{-1}$ . Low viscosity samples will spread faster (higher shear rates) and over longer distances. Products with a high viscosity or a yield stress will not spread significantly under gravity in the usual oral evaluation time. So probably for these products there is another evaluation criterion for viscosity. This could be the pressure (normal stress) required to produce significant flow (Cook et al., 2003).

Very important, bulk rheology does not completely characterize in-mouth texture properties. Therefore, tribology, which is the science of adhesion, friction and lubrication (Foegeding et al., 2003) becomes important. Tribology (science and technology of friction, lubrication, and wear) combines rheological and solid mechanical aspects of a dynamic contact problem. It therefore provides a useful approach to determine properties in thin films, that cannot be deduced from bulk properties nor from thin film rheology. In a study by Malone et al. (2003) average fluid film thickness, which occurs during the processing of semi-solid foods, was investigated. It is in the order of 1.5 - 25  $\mu\text{m}$ , a size range, which encompasses most of the dispersed particles found in foods. Twenty-five  $\mu\text{m}$  is also the differentiable thickness difference that is found in the framework of this research project (Chapter 2). van Vliet (2002), who gave a wide overview of the possibilities of stress or strain controlled behavior, stressed the importance of considering additionally uni- and biaxial elongational flow, as experiments with oil samples containing air bubbles showed that only elongational flow caused the bubbles to break up. Its importance for textural impression has also been mentioned by Pollen et al. (2005), who instrumentally studied the extensional viscosity (a material's resistance to elongational flow). Still this elongational flow component in-mouth has not been studied so far. This does not appear to be possible in the near future, either, since the measurement of elongational properties imposes serious difficulties.

There are earlier investigations about different aspects of the tongue-palate system, but not much is known about the flow of fluids between tongue and palate and especially not about the behavior of suspensions. Agrawal et al. (1997) looked at the connection

between the rate of breakdown (particle size reduction over time) between tongue and palate, and the toughness and elastic modulus of the food. Chiba et al. (2003) investigated the pressures between tongue and palate with the help of a transpalatal arch (TPA), which measured the tongue pressure exerted during deglutition. The values measured at various distances between 2 and 6 mm away from the mucosa were between 0.97 and 2.23 N/m<sup>2</sup>. Palatal pressure as well as the elasticity of in-mouth objects are two of the key parameters in this work, which are also relevant for the modeling presented in Chapter 3.

The modeling of physical phenomena in the oral region so far mainly refers to flavor release based on mass transfer as done by Harrison in several studies since 1996 (Harrison & Hills, 1996) or mechanical processing such as the prediction of particle sizes after chewing as done by Agrawal et al. (1997). Nicosia & Robbins (2001) used parallel plates in order to model the process of swallowing and predict ejection of the food bolus from the oral cavity. The tongue was considered as a rigid body due to its composition of muscle tissue and as containing incompressible fluid (Smith & Kier, 1989). This is also the case in the study presented here. Modeling the tongue is very difficult as it is never static. Stone et al. (2001) used continuum mechanics and modelled each tongue slice taken from an MRI as a single 2D object. The modeled tongue was only capable of rotation, translation, and homogeneous strain and shear. 3D models were possible but static. Napadow et al. (1999) used finite element modeling to represent the internal mechanics of the tongue but had problems incorporating the proper anatomy and physiology.

Since there are limitations to all of the models existing at present it was decided to work with the parallel plate model, especially since food particles, such as those present in suspensions, are principally worked by the tongue against the palate (Prinz & Lucas, 2001). The approach in this work is taken on a micro-scale level (Chapter 3), i.e. at the level of the particles and embedding fluid and not for the bulk fluid. Suspensions are looked at with the objective to understand “grittiness” perception. The work done by Malone et al. (2003) on film thickness between tongue and palate was a first approach in this direction.

A mathematical as well as a mechanical model are constructed. For this purpose the tongue and palate are represented by two parallel plates of known diameter. The mechanical approximation of the tongue-palate assembly by a two-plate system is similar to the simplification of Booth et al. (2003). He represented the biting of a cookie simply with a 3-point break rig. Weipert et al. (1993) actually suggested a two-plate model for the representation of tongue and palate.

The plates are at the beginning a known distance apart, then the top plate moves towards the bottom plate at a constant speed like in a squeeze flow rheometer. Between these plates there is a fluid of known viscosity, which is gradually squeezed out in the radial direction.

At the beginning, when the reliability of the instrument is still being tested, the fluid does not contain any particles. The behavior of the fluid between the plates is axisymmetric squeeze flow with constant contact area between sample and plates. Various mathematical models are applied in order to describe the flow, pressure, and velocity field between the plates with and without particles. The resulting pressure profile across the plates in dependence of the plate radius is first described by the pressure form of the Stefan equation (Stefan, 1874).

As a next step the force on a single particle is considered. For this Faxen's first law is used. Then the free space Green function allows determination of the pressure and velocity field due to this point force. The bounded Green function from Blake & Chwang (1974) is considered afterwards since it can take possible boundary conditions such as the presence of the bottom plate into account. Both Green functions give pressures and velocities. The stress tensor can be derived from these quantities. Thus, the disturbances due to the presence of a particle can be determined.

In the experimental part these pressure field fluctuations need to be demonstrated. The experimental set-up consists of two parallel plates and a Tekscan pressure sensor in sheet form, which is attached to the bottom plate. The sensor should show the variations when the fluid containing particles is compressed between the plates. This is the intermediate step before conducting the same experiment in vivo, i.e. let test

subjects evaluate suspensions for grittiness. This verification has not been done within the framework of this thesis and the question remains open for future work. The suspensions have to be designed so that they show stress field disturbances in the mathematical model as well as on the sensor of the mechanical model, and finally in the human mouth.

Modeling particles and their resulting stress fields is a reasonable approach because some of the superficial receptors in the tongue are actually tuned to detect forces even in the low mN range (Trulsson & Essick, 1997). The data from Engelen et al. (2002) suggests that the tongue rather than the palate is probably responsible for the sensory evaluation of this type, but more importantly it confirms the general feasibility of the study.

Recapitulating the basic ideas of this thesis the questions to be answered within the framework of this work are:

1. **How sensitive is the human mouth to geometric size differences when evaluated between tongue and palate?**
2. **What are the detection processes?**
3. **How can these processes be expressed with the help of mathematical models?**
4. **How does a human being perceive grittiness in the oral cavity? Could it be the perception of stress field perturbations?**
5. **What do these perturbations look like?**
6. **How well do the mathematical models agree with experimental data?**

## Chapter 2

# Geometrical resolution limits in the human mouth

In order to understand textural perception it is necessary to know the stereognostic ability for objects in mouth, i.e. the ability to recognize and to distinguish forms and sizes. For the definition of the shear rate (velocity divided by a characteristic length over which the velocity varies) the judgement of object sizes in the mouth is absolutely necessary. This assumes that shearing is distance controlled. Also for the perception of *grittiness* the sensitivity for object sizes has to be understood. Grittiness is a special smaller size case of granularity, which is a textural attribute relating to the perception of the size and shape of particles in a product (Association Francaise de Normalisation, 1995b). The study described in the following is carried out in order to determine this geometric sensitivity and to draw conclusions about the detection process(es). Disks are differentiated concerning their differences in height and diameter. Up to now grittiness has only been investigated as a function of the dispersion medium, particle size, shape, and concentration (Imai et al., 1995; Engelen, 2004). There is little published information available on intraoral size perception as stated by Engelen et al. (2002), who reports size sensitivity trials for spheres of varying size, material, and weight/density. Spheres lead to a small, indeterminate area of contact on the palate because the palate is not compliant in comparison with the tongue, which can sense

the sphere's full size. Therefore, Engelen suggested the use of plastic plates instead of spheres as done in the experiments described further on.

## 2.1 Materials & methods

### 2.1.1 Sensory test procedure

The assessment took place on a one to one basis. All trials were pair comparisons, where one disk at a time was placed on a blind-folded subject's tongue with tweezers. Subjects were instructed to press the tongue with the disk against the palate for evaluation since touch sensation is the most acute in the anterior part of the tongue and hard palate (Ten Cate, 1994).

At the same time they were instructed not to turn or bite the disks, nor to move them excessively, see Figure 2.1. The disks were removed from the mouth with a tissue in order to avoid touching with the hands and the introduction of an extra parameter: as previously mentioned the mechanoreceptors of the tongue and finger are very similar (van Boven & Johnson, 1994) and thus the sensation between tongue and palate is comparable to the one between finger and palm (Jacobs et al., 2002). Samples could have also been evaluated visually, thus the blind-folding. Once the second disk had been evaluated the subjects were asked to name the apparently larger (diameter sensitivity determination), respectively thicker (height sensitivity determination) sample. By asking the question in this way a 2-Alternative Forced Choice test (2-AFC) was carried out, which allows the statistical analysis described in the data processing Section.

### 2.1.2 Subjects

A minimum number of fifteen subjects participated in each trial to assure statistical significance. If material and time permitted up to 25 subjects evaluated samples in duplicate and triplicates. This was only different for the pre-trials (7 subjects), which

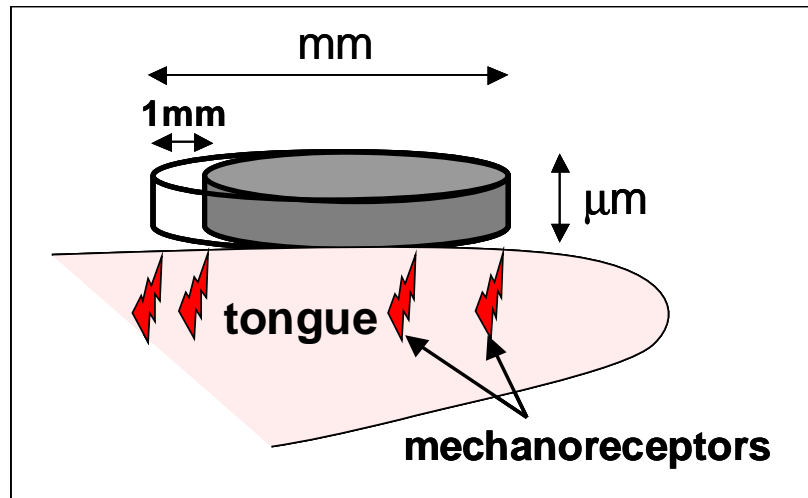


Figure 2.1: Schematic illustration of the trial procedure for disks varying in diameter.

aimed at the determination of the general feasibility of the trials and relied strongly on subjective judgement by test subjects. Subjects were randomly chosen concerning age and gender. The range of age of the subjects varied between 21 and 39 years. The influence of age could be neglected: age dependent changes as for example the muscle weakening in elderly mentioned by Roininen et al. (2004) only occur at age 60+. Informed consent was received from all subjects.

### 2.1.3 Materials (films)

Small disks made from polyethylene terephthalate (PET, Eastman, Young's modulus 1900 MPa) films of three different thicknesses (50, 75, and 250  $\mu\text{m}$ ) were used for series A and B of the preliminary trials (see Section 2.1.4). Disks of 3, 5, 6, and 10 mm diameter were punched out of these films leading to 12 possible disks (see Table 2.1). Multiples of these disks were used in the trials. Series C, evaluating the finger (index)-palm system, used the standard film from the main series explained below. All materials were obtained in form of films and available in the thicknesses described in Table 2.2.

For the main trial series, focusing on the sensitivity for vertical differences (“thick-

Table 2.1: Possible disks resulting from three different thicknesses and four diameters.

diameter	3 mm	5 mm	6 mm	10 mm
thickness				
50 $\mu\text{m}$	x	x	x	x
75 $\mu\text{m}$	x	x	x	x
250 $\mu\text{m}$	x	x	x	x

ness”), three different materials were tested:

1. “standard material”: Fluoroethylene propylene (FEP, DuPont), Young’s modulus 480 MPa, used in series C and series 1-3,
2. “stiff material”: Polyethylene terephthalate (PET, Klöckner Pentaplast), Young’s modulus 2060 MPa, used in series 2 and series 3,
3. “compliant material”: whey protein - glycerol (65 : 35) films (NIZO food research), Young’s modulus approximately 90 MPa, used in series 3 (for details about the production please see below).

The standard films disposed of the following thicknesses: 12.5, 25, 50, 75, 125, 190, and 250  $\mu\text{m}$  (for later trials further disks, 150 and 180  $\mu\text{m}$ , were added, see further on for modification process of the films). Disks of 3 and 5 mm diameter were punched out of these films. For the stiffer and compliant films only two thicknesses (150 and 180  $\mu\text{m}$ ) and one diameter (3 mm) were used (see Table 2.2 for an overview of all materials used).

### 2.1.3.1 Thinning of standard films

The films were placed between the two plates of a heatable load cell. The films were of 10 cm x 10 cm surface. The plates were heated until 270 °C (melting temperature of

Table 2.2: Classification of all disks used in the main study in terms of diameter, thickness and material.

Material	“standard”		“stiff”		“compliant”	
	DuPont		Klöckner		NIZO	
E[MPa]	480		2060		90	
Thickness	diameter [mm]		diameter [mm]		diameter [mm]	
$\mu\text{m}$	3	5	3	5	3	5
12.5	x	x	-	-	-	-
25	x	x	-	-	-	-
50	x	x	-	-	-	-
75	x	x	-	-	-	-
125	x	x	-	-	-	-
150	(x)	-	x	-	x	-
180	(x)	-	x	-	x	-
190	x	x	-	-	-	-
250	x	x	-	-	-	-
350	x	x	-	-	-	-

Teflon) before a load of 100 kN was applied for a duration of 7 min. After the thinning it was possible to punch out disks of 150 and 180  $\mu\text{m}$  from the original 190  $\mu\text{m}$  thick but now thinned films. The punched out disks were measured with a Käfer micrometer (resolution 1  $\mu\text{m}$ , calibration with 100  $\mu\text{m}$  film from Mitutoyo no. 030122) in triplicates in order to determine their thickness with minimum error. The procedure was the same for the creation of the 225 and 250  $\mu\text{m}$  thick films used later on.

### 2.1.3.2 Whey protein-glycerol films (WP/G)

These films were provided by NIZO food research. An 8 % whey protein isolate (WPI, type BIPRO, from Davisco Food International, Le Sueur, USA) was heated at 85 °C

for 80 minutes. The solution was subsequently filtered (sieve) to remove any large flocs. Glycerol (BDH Laboratory) was added to the protein solution to obtain a ratio of WPI: glycerol of 65:35. Films were prepared by casting an aliquot of protein solution into Petri dishes and evaporating the solvent at ambient temperature. The elastic modulus was characterized using a Texture Analyzer TA-XT2 with a 25 kg load cell, following the approach of ASTM-D882-02 (2005) (Standard Test Method for Tensile Properties of Thin Plastic Sheeting). Films were cut to 70 mm x 35 mm. The initial distance between the grips was 60 mm, the speed of separation of the grips was 1.6 mm/sec. The elastic modulus was determined during the first part of the stress strain curve. For each value of the elastic modulus an average of five measurements was taken. Afterwards disks of 3 mm were punched out of these films using of a hand press. The thicknesses of these disks were measured with a Kafer micrometer (see above), three times for each disk, and then the average was taken.

## 2.1.4 Geometrical sensitivity experiments

### 2.1.4.1 Introductory trials for determination of the feasibility

The trials were conducted in six sessions (A, B, C, 1, 2, and 3) and some sub-sessions (a, b, and c). Three trials (A, B, and C) were carried out for general orientation and determination of the feasibility of a larger study. For an overview of all the trials carried out see Table 2.3. Values in rows were compared with each other whereas values in columns were kept constant. For series B this means for example that disks of 50, 75, and 250  $\mu\text{m}$  thickness were compared but they all had the same diameter of 3 mm.

The first two trial series (A and B) focused on:

1. horizontal sensitivity: by the means of different diameters (study A)
2. vertical sensitivity: by the use of different thicknesses (study B)

The third preliminary trial (series C) investigated the statement made by, e.g. Jacobs

et al. (2002) and Sakada (1983), that the tongue-palate system is similar to the finger-palm system. The idea was to verify the suitability of this system in order to be able to also use non food-grade materials since in-mouth contact can be avoided. At the same time the finger-palm system reduces stimuli such as taste and smell.

For all trials only one parameter out of thickness, diameter or Young's modulus, was varied at a time. Table 2.4 shows comparisons of disks of constant thickness and material but varying diameter (study A), Table 2.5 gives pairs of disks with constant diameter and material but varying thickness (study B) in all combinations, which were investigated. Table 2.6 shows all pairs evaluated between finger and palm (preliminary series C) and main study 1.

Table 2.3: Overview and further references for all trial series carried out.

series	subjects	system	diameter	thickness	material/[E]=MPa
<b>preliminary study</b>					
A	7	tongue-palate	3,5,6,10	50 75 250	PET 1900
B	7	tongue-palate	3 5 6 10	50,75,250	PET 1900
C	7	index-palm	5 3	12.5,25,50,75,125,190,250	FEP 480
<b>main study</b>					
1a	15	tongue-palate	5	12.5,25,50,75,125,190,250	FEP 480
1b	15		3		
1c	14		3	50 vs. 75, 225 vs. 250	
2a	13	tongue-palate	3	150 vs. 180	FEP 480
2b	15		3	150 vs. 180	PET 2060
3a	25	tongue-palate	3	150 vs. 180	WP/G 90
3b	10		3	150 vs. 180	PET 2060

Table 2.4: Pairs of disks which were compared in the framework of *diameter* sensitivity detection (series A).

thickness [ $\mu\text{m}$ ]	diameter 1 [mm]	diameter 2 [mm]
250 $\mu\text{m}$	5	6
	6	10
	3	5
75 $\mu\text{m}$	5	6
	6	10
	3	5
50 $\mu\text{m}$	5	6
	6	10
	3	5

Table 2.5: Pairs of disks which were compared in the framework of *thickness* sensitivity detection (series B).

diameter	thickness 1 [ $\mu\text{m}$ ]	thickness 2 [ $\mu\text{m}$ ]
10	50	75
	75	250
6	50	75
	50	250
5	50	75
	75	250
3	50	75
	75	250

Table 2.6: Pairs of disks which were compared in the framework of *finger-palm* trials (series C, but also series 1). The trial was carried out for disks of 5 mm diameter and repeated for 3 mm.

thickness 1 [ $\mu\text{m}$ ]	thickness 2 [ $\mu\text{m}$ ]
12.5	25
25	50
50	75
75	125
125	190
190	250

#### 2.1.4.2 Thickness determination (main study)

The main study consisted of three series of trials (1-3), each focusing on a different material. The stimuli for the series 1 were adjacent pairs of disks of the eight standard films (see Table 2.2 and Table 2.6), all disposing of the same diameter (once 5 mm and once 3 mm). The 5 mm disks were compared first (15 subjects). After a small break the 3 mm pairs were compared (1b). During this session a re-evaluation of the 50/75 and a new pair (225/250) was carried out by 14 randomly chosen subjects (1c).

The second and third series focused on one single pair, i.e. 150 versus 180  $\mu\text{m}$ , but made of different materials. Series 2 evaluated first the standard material (13 randomly chosen subjects) and then the stiff material (15 subjects- varying number of subjects and its influence are explained below).

Series 3 (25 subjects) compared the same pair of disks but made of the compliant material. Ten randomly chosen subjects re-evaluated the stiff pair to confirm the impossibility to detect the difference.

### 2.1.5 Data processing

Data was collected using a sensory difference test called 2-Alternative Forced Choice (2-AFC, Lawless & Heymann (1999)) and analyzed by the means of an adapted and common statistical hypothesis testing approach. As for all statistical tests, a null hypothesis  $H_0$  and an alternative hypothesis  $H_1$  are defined:

- $H_0$ : disk 1 and disc 2 are not different in thickness
- $H_1$ : the two disks are perceived as significantly different in thickness.

Each experiment has a fixed number of trials. When the outcome of each trial is only success or failure, when trials are independent, and when the probability of success is constant throughout the experiment, this can be expressed via a binomial  $b(x, N, P)$ , where:

- $X$  is the random variable representing the number of correct answers
- $x$  is the number of correct answers in the data
- $N$  is the number of trials (panelists multiplied by repetitions)
- $P$  is the probability for success, i.e. 0.5

It is therefore possible to calculate the probability, under  $H_0$ , to have  $X = x$  correct answers in the data:

$$b(x, N, P) = \frac{N!}{(N-x)!x!} P^x (1-P)^{N-x} = p(X = x), \quad (2.1)$$

or to have  $x$  or more correct answers in the data (cumulative binomial distribution):

$$B(x, N, P) = \sum_{y=x}^N \frac{N!}{(N-y)!y!} P^y (1-P)^{N-y} = p(X \geq x) \quad (2.2)$$

This probability is called the p-value. According to common practice this value is set at 5 %. If the p-value is lower than 5 %, then  $H_0$  is rejected and the two disks

can be considered as being significantly different in thickness. The level of 5 % is called the level of significance and represents the risk to reject  $H_0$  when it is effectively true. It has to be kept in mind that if  $p > 0.05$ ,  $H_0$  cannot be rejected, but it does not mean that  $H_1$  is automatically accepted (Henze, 1997). Since the proof for similarity is not straightforward and statistically not possible for a 2-AFC but only for a triangle test, another condition was introduced before the conclusion on similarity could be admitted. If the hypothesis that two disks are similar could not be rejected, i.e.  $p > 0.05$ , and simultaneously the percentage of correct responses was between 30 and 70 %, hence the results must be due to no more than pure chance, the two disks were considered as non-differentiable.

### 2.1.6 Mathematical model

A mathematical model was applied to predict the load  $P$  exerted on the disks when manipulated by the tongue. It was assumed that, when the tongue presses the disk against the palate, the disk is aligned with the palate (see Figure 2.2) due to a distributed load  $P(r)$ . This force intensity is generated through activation of the tongue muscle. The contraction of the muscle allows contact between tongue and disk causing a deflection. The distributed load is a force intensity and has the dimension of a force per surface area. It has a normal and a tangential component. The normal component is responsible for the deflection, since the tangential component disappears due to radial symmetry. Additionally lubricating effects of saliva do not allow any shear component. This normal force intensity is unknown but can be determined through use of linear plate bending theory (Timoshenko & Woinoswky-Krieger, 1959) and the radius of curvature of the palate. For small deflections/deformations (linear theory of plates and shells (Timoshenko & Woinoswky-Krieger, 1959)) the normal component of the force intensity (induced through deflection) can be neglected.

The radius of curvature of the palate  $R_C$  was determined experimentally to be 1 cm. For this an imprint of one subject's palate was taken with the help of alginate impression material (Cavex Holland BV, Cavex Impressional Fast Set). The imprint was then

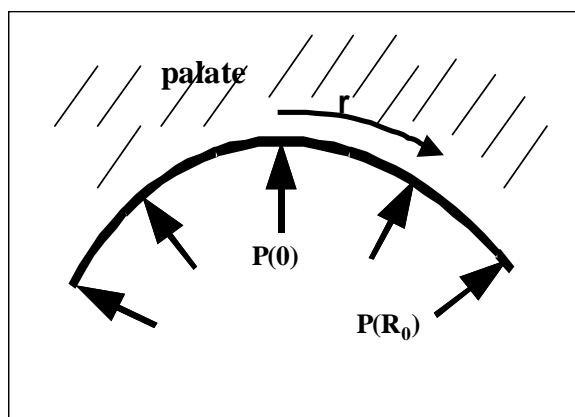


Figure 2.2: Schematic illustration of the distributed load across the bent disk with a preset deformation profile.

cut at its highest point, and the diameter measured with a caliper in longitudinal and cross-sectional direction (Figure 2.3). In order to obtain the radius the retrieved value was divided by two. No great variations could be found between the longitudinal and cross-sectional value, see also Figure 2.3. This is why the impressing of the disk can be imagined as pressing it against the inside of a spherical shell with 1 cm radius. Measuring only one subject is not representative but it was sufficient to retrieve knowledge about the order of magnitude. The actual radius might vary by millimeters but never by an order of magnitude (e.g. 10 cm instead of 1 cm).

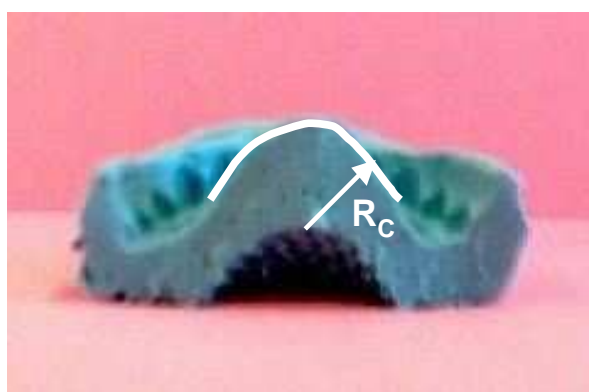


Figure 2.3: Illustration of the cross-sectional measurement of the radius of curvature in one human palate.

In the following the development of the model for treating the bending of the disks

against the human palate is sketched. Consider a lateral cross-section through the palate, which takes form of part of a circle with radius  $R_C$  as demonstrated with the imprints, which has been moved towards the negative y-axis and intersects the y-axis at  $\lambda$  (Figure 2.4).

$$r^2 + (w + (R_C - \lambda))^2 = R_C^2 \quad (2.3)$$

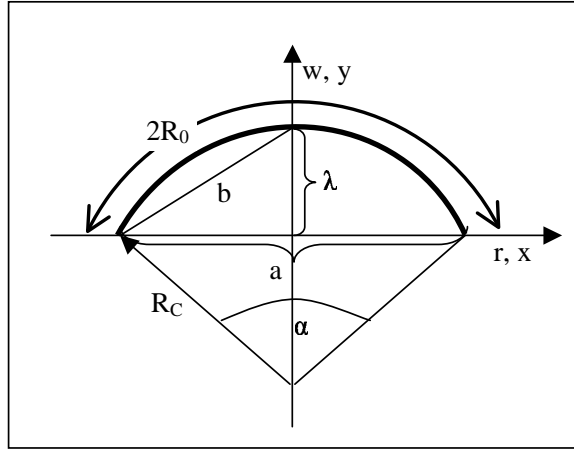


Figure 2.4: Deflection of a disk with Radius  $R_0$  in-mouth to the preset radius of curvature of the palate  $R_C$  leading to the deflection  $\lambda$ .

The part of the circular arc above the x-axis represents the bent disk and has the length  $2R_0$  with  $R_0$  being the radius of the disk. The deflection profile  $w$  was required, which can be obtained by solving the original circular equation for  $w$ .

$$w(r) = \lambda + \sqrt{R_C^2 - r^2} - R_C \quad (2.4)$$

To proceed it is necessary to relate  $\lambda$  to the radius of the disk  $R_0$  and the radius of curvature (of the palate)  $R_C$ . It is evident from Figure 2.4 that

$$\sin \frac{\alpha}{2} = \frac{a}{2R_C} \quad (2.5)$$

and that the segment length is  $2R_0 = R_C \alpha$ , hence  $\alpha = \frac{2R_0}{R_C}$ , therefore

$$\lambda = R_C \left( 1 - \cos \frac{R_0}{R_C} \right). \quad (2.6)$$

Since the dependence of  $\lambda$  on  $R_C$  is now known it is possible to calculate the deflection profile  $w(r)$ . An integral equation, which is derived in Timoshenko's "Theory of

Plates and Shells” (Timoshenko & Woinoswky-Krieger, 1959) and which is explained in the following, is used to determine the resulting load distributions as a function of the radius. The following boundary conditions are assumed:

1. The slope at the center of the disk is zero:  $w'(R_C) = 0$ .
2. The deflection at the edge is zero:  $w(R_0) = 0$ .
3. The bending moment at the edge is zero:  $\frac{1}{R}w'(R_0) + \nu w''(R_0) = 0$ .

The theory deals with symmetrical bending of circular plates and the special case discussed here is bending of thin plates with small deflections. The deflections have to be small (i.e. <10 %) in comparison with the plate’s thickness  $h$ . This condition has been checked, e.g. for a disk of 0.0015 m radius a deflection of 0.0001122 m results, which is equivalent to 8 %. A very satisfactory approximate theory of bending of the plate by lateral loads can be developed by making the following assumptions:

1. there is no deflection in the central fiber of the plate. This plane remains *neutral* during bending.
2. points of the plate lying initially on a normal-to-the-middle plane of the plate remain on the normal-to-the-middle surface of the plate after bending
3. the normal stresses in the direction transverse to the plate can be disregarded

Using these assumptions, all stress components can be expressed through the deflection  $w$  of the plate, which is a function of the two coordinates in the plane of the plate. This function together with the boundary conditions completely defines  $w$ . Thus the solution of this equation gives all necessary information for calculating stresses at any point of the plate.

If the load acting on a circular plate is symmetrically distributed about the axis perpendicular to the plate through its center, the deflection surface to which the middle plane of the plate is bent will also be symmetrical. At all points equally distant from

the center of the plate the deflections will be the same, and it is sufficient to consider deflections in one diametral section through the axis of symmetry. The origin of the coordinate system will be set as 0 at the center of the non-deflected plate,  $r$  denotes the radial distance and  $w$  the deflections of the disk in the downward direction (Figure 2.5, in accordance with Figure 2.4).  $B$  is a point on the axis through the origin, and  $A$  is a point on the disk.  $\varphi$  refers to the small angle between the normal to the deflection surface at  $A$  and the axis of symmetry  $OB$ .

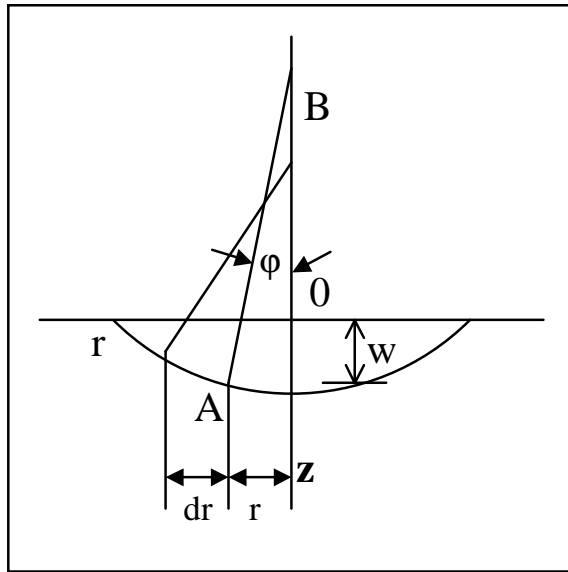


Figure 2.5: Illustration of the deflected disk in a coordinate system, where  $r$  denotes the radial distance,  $w$  the deflection of the disk in the downward direction.

The slope of the deflection at any point is  $\frac{-dw}{dr}$ , and the curvature of the middle surface of the plate in the diametral section  $rz$  for small deflections (linear theory) is

$$\frac{1}{R_n} = \frac{d^2w}{dr^2} = \frac{d\varphi}{dr} \quad (2.7)$$

This is one of the principle curvatures. A second one is through  $AB$  but perpendicular to the  $rz$  plane. From Figure 2.5 it can be obtained that

$$\frac{1}{R_t} = -\frac{1}{r} \frac{dw}{dr} = \frac{\varphi}{r}. \quad (2.8)$$

Using expressions (2.7) and (2.8) for the principle curvatures, and assuming that the bending moments (2.9) and (2.10),

$$M_x = D \left( \frac{1}{r_x} + \nu \frac{1}{r_y} \right) = -D \left( \frac{\partial^2 w}{\partial x^2} + \nu \frac{\partial^2 w}{\partial y^2} \right) \quad (2.9)$$

$$M_y = D \left( \frac{1}{r_y} + \nu \frac{1}{r_x} \right) = -D \left( \frac{\partial^2 w}{\partial y^2} + \nu \frac{\partial^2 w}{\partial x^2} \right), \quad (2.10)$$

which were originally derived for pure bending of a rectangular plate with  $x$  and  $y$  coordinates (Timoshenko & Woinoswky-Krieger, 1959), still hold, the bending moments described in (2.11) and (2.12) can be obtained.  $D$  with  $D = \frac{Eh^3}{12(1-\nu^2)}$  ( $E$  = elastic modulus,  $h$  = disk thickness, and  $\nu$  = Poisson ratio) is the flexural rigidity.

$$M_r = -D \left( \frac{d^2 w}{dr^2} + \frac{\nu}{r} \frac{dw}{dr} \right) = D \left( \frac{d\varphi}{dr} + \frac{\nu}{r} \varphi \right) \quad (2.11)$$

and

$$M_t = -D \left( \frac{1}{r} \frac{dw}{dr} + \nu \frac{d^2 w}{dr^2} \right) = D \left( \frac{\varphi}{r} + \nu \frac{d\varphi}{dr} \right) \quad (2.12)$$

The effect of shearing stresses acting on normal sections of the plate perpendicular to meridians is neglected here. Their effect is slight in the case of plates for which the thickness is small in comparison with the diameter.

The moment  $M_r$  acts along circumferential sections of the plate, such as the section made by the conical surface with the apex at  $B$ , and  $M_t$  acts along the diametral section  $rz$  of the plate. Equations (2.11) and (2.12) only contain  $\varphi$  or  $w$ , which can be determined by considering the equilibrium of an element of the plate which was cut out from the plate by two cylindrical sections  $ab$  and  $cd$  and by two diametral sections  $ad$  and  $bc$  (Figure 2.6).  $Q$  refers to the load applied on the element of the disc. This is the actio. The re-actio is shown by  $M_r$ , respectively  $M_t$ .

The bending moment  $M_r$  acting on the side  $cd$  of the element is

$$M_r r d\theta. \quad (2.13)$$

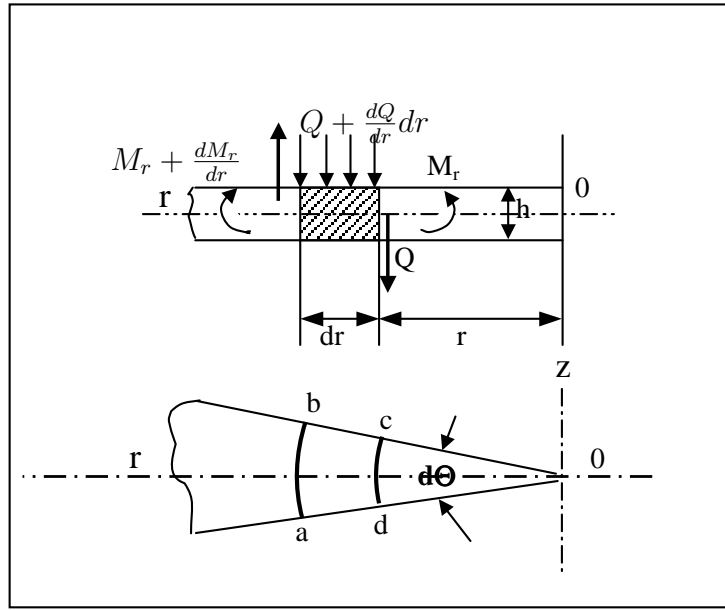


Figure 2.6: Equilibrium on an element of the plate, i.e. internal reaction  $M_r$  to external load  $Q$  on the element

The corresponding bending moment on the side  $ab$  is

$$\left( M_r + \frac{dM_r}{dr} dr \right) (r + dr) d\theta. \quad (2.14)$$

The bending moments on the sides  $ad$  and  $bc$  of the element are each  $M_t dr$ , and they give a resultant bending moment in the plane  $r\theta z$

$$M_t dr d\theta. \quad (2.15)$$

From symmetry it can be concluded that the shearing forces that may act on the element must vanish on diametral section of the plate but that they are usually present on cylindrical sections such as sides  $cd$  and  $ab$  of the element. Denoting by  $Q$  the shearing force per unit length of the cylindrical section of radius  $r$ , the total shearing force acting on the side  $cd$  of the element is  $Q_r d\theta$ , and the corresponding force on this side  $ab$  is

$$\left[ Q + \left( \frac{dQ}{dr} dr \right) \right] (r + dr) d\theta. \quad (2.16)$$

Neglecting the small differences between the shearing forces on the two opposite sides of the element, it can be stated that these forces give a bending moment in the

$rz$  plane equal to:

$$Qrd\theta dr. \quad (2.17)$$

Summing up the moments (2.13), (2.14), (2.15), and (2.17) with proper signs and neglecting the moment due to the external load on the element as a small quantity of higher order, the following equation of equilibrium on the element  $abcd$  can be obtained

$$\left( M_r + \frac{dM_r}{dr} dr \right) (r + dr) d\theta - M_r r d\theta - M_t dr d\theta + Qrd\theta dr = 0, \quad (2.18)$$

for which it can be found, by neglecting high order quantities, that

$$M_r + \frac{dM_r}{dr} r - M_t + Q_r = 0. \quad (2.19)$$

Substituting expressions (2.11) and (2.12) for  $M_r$  and  $M_t$  equation (2.19) becomes

$$\frac{d^2\varphi}{dr^2} + \frac{1}{r} \frac{d\varphi}{dr} - \frac{\varphi}{r^2} = -\frac{Q}{D} \quad (2.20)$$

or, in another form,

$$\frac{d^3w}{dr^3} + \frac{1}{r} \frac{d^2w}{dr^2} - \frac{1}{r^2} \frac{dw}{dr} = \frac{Q}{D}. \quad (2.21)$$

Sometimes it is advantageous to represent the right-hand side of equation (2.21) as a function of the intensity  $P$  of the load distributed over the plate. For this purpose both sides of the equation are multiplied by  $2\pi r$ . Then, observing that

$$Q2\pi r = \int_0^r P(r)2\pi r dr \quad (2.22)$$

we obtain

$$\int_0^r P(r)2\pi r dr = D 2\pi r \left( \frac{d^3w}{dr^3} + \frac{1}{r} \frac{d^2w}{dr^2} - \frac{1}{r^2} \frac{dw}{dr} \right), \quad (2.23)$$

When differentiating this equation with respect to  $r$ , dividing by  $r$ , and substituting for  $w$ , the load across the disk in dependance of the radius  $r$  can finally be obtained.

$$P(r) = \frac{64 D \lambda^2 (R_0^8 + 4R_0^6 \lambda^2 - 2r^4 \lambda^4 + 4r^2 \lambda^6 + \lambda^8)}{(R_0^4 - 4r^2 \lambda^2 + 2R_0^2 \lambda^2 + \lambda^4)^3 \sqrt{-4r^2 + \frac{(R_0^2 + \lambda^2)^2}{\lambda^2}}} + \frac{64 D \lambda^2 (R_0^4 (4r^2 \lambda^2 + 6\lambda^4) + 4 R_0^2 (2r^2 \lambda^4 + \lambda^6))}{(R_0^4 - 4r^2 \lambda^2 + 2R_0^2 \lambda^2 + \lambda^4)^3 \sqrt{-4r^2 + \frac{(R_0^2 + \lambda^2)^2}{\lambda^2}}} \quad (2.24)$$

In order to compare the load profiles for different disks  $\frac{P(0)}{P(R_0)}$  is evaluated and used as a characteristic dimensionless number representing the ratio of the distributed load value in the center to the one at the edge.

## 2.2 Results

In the following the results of the preliminary and main trials are presented. The previously discussed mathematical model was used in order to determine the conditions for confirmatory trials.

### 2.2.1 Preliminary trials

First of all it has to be stated that all subjects were able to sense certain differences and confirmed the feasibility of the study by reasonable judgement. For the horizontal sensitivity trials (series A) the comparison of adjacent pairs showed that subjects could significantly differentiate between 3 and 5 mm, and 6 and 10 mm diameters (see Table 2.7), but most importantly between 5 and 6 mm diameters (17 of 21 subjects, when adding the replies for the same diametric difference, replied correctly,  $p < 0.05$ ), which suggests a sensitivity of at least 1 mm since no smaller disks were tested. For the preliminary vertical sensitivity trials (series B) there were three situations for which differentiation was not possible with 100 % certainty (see Table 2.8). This occurred for the 50 - 75 pair at 3, 5, and 6 mm, where the number of wrong answers increased with reduced diameter (from three wrong answers out of seven for the 6 mm disk to 4 wrong answers out of seven for the 5 mm disk, and then up to five out of seven wrong answer for the 3 mm disk). When regarding these results it has to be kept in mind that the general idea was to receive a subjective opinion from the test subjects about the feasibility of a larger study. The total number of participants was not sufficient for significant statistical analysis.

Table 2.7: Series A: diameter differentiation between tongue and palate (the replies for pairs comparing the same diameters were added leading to a total of 21 replies for the calculation of the p-value).

diameter [mm]		thickness	correct/	sum	p-value
disk 1	disk 2	[ $\mu\text{m}$ ]	total		
		50	7/7		
3	5	75	7/7	21/21	0.000
		250	7/7		
		50	5/7		
5	6	75	6/7	17/21	0.001
		250	6/7		
		50	7/7		
6	10	75	7/7	21/21	0.000
		250	7/7		

Table 2.8: Series B: thickness differentiation between tongue and palate. It can only be summed for the comparison of 75 versus 250  $\mu\text{m}$ .

thickness [mm]		diameter	correct/
disk 1	disk 2	[mm]	total
50	75	10	7/7
50	75	6	4/7
50	75	5	3/7
50	75	3	2/7
75	250	3	28/28

For the finger-palm system (series C) the study was once carried out for disks with 5 mm diameter and repeated for disks of 3 mm diameter with the following thicknesses: 12.5, 25, 50, 75, 125, 190, and 250  $\mu\text{m}$ . For all adjacent pairs of these disks differentiation was possible ( $p < 0.05$ ) except for the comparison of 12.5  $\mu\text{m}$  and 25  $\mu\text{m}$ , which is certainly due to the threshold value of 25  $\mu\text{m}$  explained later on (for an overview of the results see Table 2.9). In comparison with the first series of the main study it becomes clear that the finger-palm system is as sensitive as the tongue palate system. Ten Cate (1994) stated that the fingertips fall between the tongue and hard palate in a ranking according to sensitivity. This lead to the conclusion that if the tongue is included, as it is the case in the tongue-palate system, this is more sensitive than the finger-palm combination. van Boven & Johnson (1994) were even more explicit when stating that the smallest grating groove and bar widths that subjects discriminated with lip and tongue were 30 to 40 % lower than the fingertip. Still, during the later discussion we will see that there are some drawbacks which hinder the precision.

Table 2.9: Results of the *finger-palm* trial (series C) for 15 tested subjects. For  $p < 0.05$  at least 11 correct replies are required.

		thickness		correct replies		possible
		[ $\mu\text{m}$ ]		3 mm	5 mm	
12.5	vs.	25		8	12	yes
25	vs.	50		11	12	yes
50	vs.	75		14	13	yes
75	vs.	125		15	14	yes
125	vs.	190		11	14	yes
190	vs.	250		14	13	yes

For the later discussion it has to be pointed out that there was no gap in the detection process for the finger-palm system. All pairs could be differentiated with a sensitivity of 25  $\mu\text{m}$ .

Table 2.10: Pair comparison of selected standard disks (DuPont FEP, elastic modulus 480 MPa) showing that a distinction between two disks varying by 50  $\mu\text{m}$  and even just 25  $\mu\text{m}$  in thickness is possible for both diameters.

no.	diameter [mm]	thickness [ $\mu\text{m}$ ]	answers (correct/total)	p-value	possible
1	5	75 vs. 125	11/15	0.018	yes
2		50 vs. 75	13/15	0.001	yes
3	3	75 vs. 125	12/15	0.004	yes
4		50 vs. 75	19/29	0.031	yes

## 2.2.2 Sensitivity to thickness differences (main study)

### Series 1

The results from the thickness sensitivity trials for the standard material allowed arrangement of the standard disks into three different intervals as demonstrated in Figure 2.7. This Figure clearly points out regions where differentiation is possible and where no difference can be seen. The lower end of the scale including disks of thicknesses below 25  $\mu\text{m}$  is excluded in the further discussion; these disks seem to be below the threshold, which is further explained in the discussion (see Section 2.3).

The *first interval* comprises disks from 25  $\mu\text{m}$  to approximately 125  $\mu\text{m}$  thickness, and here disks with differences of 25  $\mu\text{m}$  difference in thickness could clearly be distinguished from each other, e.g. 50  $\mu\text{m}$  from 75  $\mu\text{m}$ , see Table 2.10, where four sets of pairs are presented exemplarily.

First pairs of disks with 5 mm diameter were compared (series 4a) leading to 11 correct replies out of 15 in the case of 75 versus 125  $\mu\text{m}$  ( $p = 0.018$ ) and 13 right answers out of 15 for the 50  $\mu\text{m}$  and 75  $\mu\text{m}$  disks ( $p = 0.001$ ). The trial was repeated for disks with 3 mm diameter (no. 3 and 4, series 4b) leading to 12 correct replies out of 15 for 75/125 ( $p = 0.004$ ) and 19 correct replies out of 29 for the smaller difference of 25  $\mu\text{m}$  ( $p = 0.031$ , here the replies from the repetition trial 4c are considered as well).

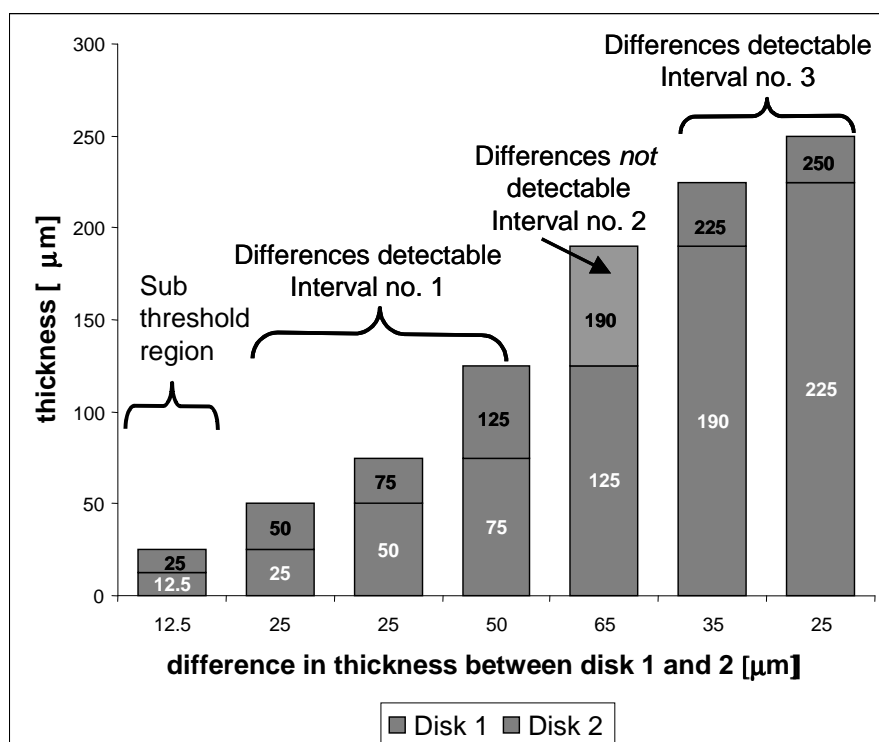


Figure 2.7: Three different intervals for the standard disks (DuPont FEP, 480 MPa) are shown in this graphic. For very thin disks (below 25  $\mu\text{m}$ ) no differentiation is possible.

Diminishment of the diameter from 5 mm to 3 mm made the trial more sensitive based on the following assumption: a certain amount of load is applied to each disk to cause alignment of the disk with the palate's curvature. The required load varies between the center and the edge, see Figure 2.8, where the general, dimensionless form is shown on a small scale. The parabolic profile is very developed. A parabolic profile for the load distribution can be obtained for any of the disk sizes and thicknesses. In Figure 2.9 two disks of the same material and diameter but different thickness (dashed < solid) can be seen. The profiles are similar but the thicker disk requires a higher load for the same deflection. Figure 2.10 shows another important characteristic: small disks have a smaller pressure decrease across the surface and also the difference between the gradients is less for the same pair of disks if the diameter is changed (of course the discs were of the same thickness, here exemplarily  $25 \mu\text{m}$ ).

To support the above mentioned Figures with concrete values, Table 2.11 shows pressure values in Pa for different disk thicknesses and two diameters, i.e. 5 and 10 mm. Smaller disks require higher pressures in the disk middle than larger disks of the same thickness as can be seen in the above mentioned Table. On the contrary smaller disks need lower pressures at the edges than the corresponding larger disks. Still, the differences between the loads at the disk middle for different diameters are less than the differences at the edges (see Table 2.11). This leads to the mentioned difference in the gradients. The influence on the detection process is mentioned in the discussion Section.

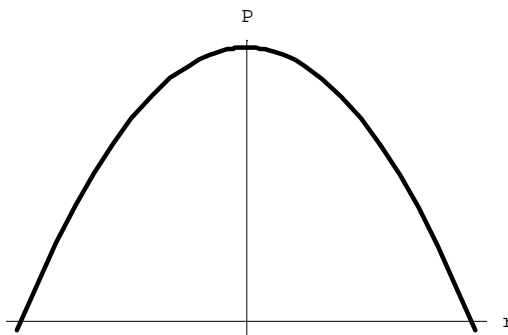


Figure 2.8: Distribution of the load  $P$  in dependence of the radius  $r$ .

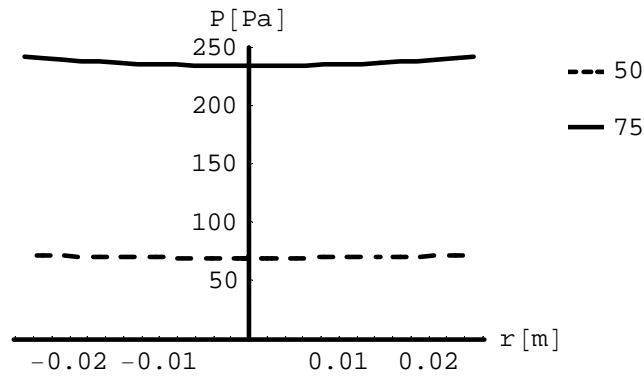


Figure 2.9: Comparison of the load profile for different thicknesses but the same diameter (5 mm) and material (standard).

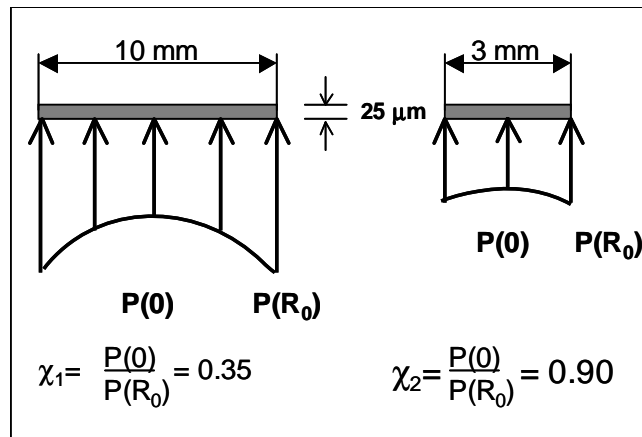


Figure 2.10: Comparison of pressure gradients  $P(0)/P(R_0)$  of disks with different diameters (3 and 10 mm) both of  $25 \mu\text{m}$  thickness.

Coming back to the intervals: the *second interval* comprises the thickness range between  $125 \mu\text{m}$  and  $190 \mu\text{m}$ . Unexpectedly the disks with thicknesses between  $125 \mu\text{m}$  and  $190 \mu\text{m}$  could not be differentiated from each other, despite the thickness difference being much greater than the expected threshold of  $25 \mu\text{m}$ , see Table 2.12 for the results.

Fifteen subjects assessed this pair, giving nine right answers. This leads to a  $p = 0.151$ , which is larger than  $0.05$ , therefore, the second condition had to be looked at: the percentage of correct answers was  $60 \%$ , therefore, the disks could really not be differentiated.

Table 2.11: Theoretically determined pressures in Pa at the disk middle ( $P(0)$ ) and the edge ( $P(R_0)$ ) of two different disks (5 and 10 mm diameter) varying in thickness.

diameter [mm]	P(0) or P( $R_0$ )	thickness [ $\mu\text{m}$ ]						
		12.5	25	50	75	125	190	250
5	P(0)	0.8	6.2	50.1	169.2	783.5	2751.49	6267.0
5	P( $R_0$ )	1.1	8.2	66.0	222.7	1030.8	3620.0	8246.4
10	P(0)	0.7	5.2	42.1	142.0	657.3	2308.3	5258.5
10	P( $R_0$ )	1.8	14.7	117.7	397.3	1839.3	6459.1	14714.1

Table 2.12: Pair comparison of standard disks (DuPont FEP, elastic modulus 480 MPa) showing that a distinction between two disks (5 mm) originating from the second interval and varying by 65  $\mu\text{m}$  in thickness is not possible (no. 1); above and below the second interval this does not pose a problem (no. 2 - 3), even for 3 mm diameters.

no.	thickness [ $\mu\text{m}$ ]	answers (correct/total)	p-value	possible
1	125 vs. 190	9/15 (60 %)	<b>0.151</b>	no
2	50 vs. 75	9/29	0.030	yes
3	225 vs. 250	11/16	0.038	yes

All disks above 200  $\mu\text{m}$  in thickness make up the *third interval*, which resembles the first one concerning the differentiation possibilities, see Table 2.12. Here the comparison of 225  $\mu\text{m}$  versus 250  $\mu\text{m}$  is shown. Eleven correct replies out of 16 lead to  $p = 0.038$ , i.e. differentiation was possible. The pair 50 - 75 is shown once more for clarification to have one pair from each interval opposed.

### Series 2

Series 2 mainly focused on the comparison of 150  $\mu\text{m}$  and 180  $\mu\text{m}$  disks, but of two different materials, i.e. the original (2a) and the less flexible (2b) material. The two standard disks could not be differentiated from each other, since only six correct answers out of 13 could be obtained leading to a correct responsive percentage of only 46 %, see Table 2.13 for the results. The deviation from the standard test subject number of minimum 15 can be explained by a lack of material. In defense of the work it has to be mentioned that even two further positive replies would not change the overall result. For the stiffer disks the same result was received, the two disks of 150  $\mu\text{m}$  and 180  $\mu\text{m}$  could not be differentiated from each other since only 14 out of 25 subjects ( $p = 0.212$ ) replied correctly.

Table 2.13: Pair comparison of 150  $\mu\text{m}$  and 180  $\mu\text{m}$  (3 mm) disks of materials varying in the elastic modulus (480 MPa, 2060 MPa, and 90 MPa). The soft (90 MPa) material leads to significant difference but not the other two.

elastic modulus [MPa]	thickness [ $\mu\text{m}$ ]	answers (correct/total)	p-value	possible
480	150 vs. 180	6/13 (46 %)	<b>0.387</b>	no
2060	150 vs. 180	14/25 (62 %)	<b>0.212</b>	no
90	150 vs. 180	41/64	0.008	yes

### Series 3

The results from the third series are in contrast to the results from the second series investigating the standard and stiff material. The comparison of the same disks made from compliant material resulted in 41 correct replies out of 64 ( $p = 0.008$ ). Therefore, differentiation was possible (see Table 2.13).

## 2.3 Discussion

The spatial resolution capacity for diameter differences is around 1 mm. This finding is consistent with neurological data. Johnson (2001) discovered receptive fields of 2 - 3 mm leading to a discrimination threshold of 0.5 mm. The studies of Conner & Johnson (1992) showed the spatial resolution of the somatosensory system (sensory performance of the surface of the body) to be approximately 0.5 mm. Trials conducted by van Boven & Johnson (1994) proved the tongue spatial resolution capacity to be 0.58 mm. From the results of the thickness sensitivity trials conclusions about the detection process can be made, which are explained in the following. The four pairs illustrated in Table 2.10 could all be differentiated from each other and this lead to the conclusion that a difference in thickness of 25  $\mu\text{m}$  can be detected.

The last two pairs were a repetition of the first two but for a smaller diameter. By diminishment of the diameter from 5 to 3 mm the trial was made more sensitive as explained in Section 2.2.2. Since the ratio  $\frac{P(0)}{P(R_0)}$  (see Table 2.11) becomes larger, i.e. the actual difference between the values becomes smaller, for a 3 mm disk in comparison with a 10 mm disk, judgement is more difficult. With the help of plate theory (Timoshenko & Woinoswky-Krieger, 1959) the resulting pressure profiles and ratios were calculated for each pair. We postulate that this load intensity variation caused by alignment of the disk with the palate is sensed by the tongue. The comparison of relative instead of absolute differences seems to be part of human nature since Chanasattru et al. (2002) also discovered that humans judge differences in consistency relatively rather than absolutely.

Consequently for the comparison of the alternative materials only disks of 3 mm diameter were used in order to make the trial as sensitive as possible. The result shown in Table 2.12 in the first row was in contrast to the 25  $\mu\text{m}$  threshold, though. After it had just been shown that disks differing by just 25  $\mu\text{m}$  could be distinguished from each other, a 125  $\mu\text{m}$  and 190  $\mu\text{m}$  thick disk could not be differentiated, despite a much greater thickness difference. It was suspected that they were too thick and that once a certain thickness is overcome, detection is no longer possible through alignment.

Based on the bending theory this seems reasonable. For example, for a disk of  $250\ \mu\text{m}$  thickness and 10 mm diameter a load intensity of  $\approx 10\ \text{kPa}$  (in the center) is required (see Table 2.11) when calculated according to equation (2.24). Takahashi & Nakazawa (1991b) investigated palatal pressure patterns in the human mouth during gelatine gel consumption and discovered that the pressures between tongue and palate varied between 5 - 30 kPa. These measurements were taken with three transpalatal arches equipped with pressure gauges at different points of the palate. One of them being at the anterior midpoint of the palate, i.e. at the same location where the disks were aligned. Chiba et al. (2003), also using a transpalatal arch, stated values between 9 - 22 kPa. Ono et al. (2004) used a different approach: by implementing seven sensors of 6 mm diameter each into an artificial palate they obtained pressures of 20 - 30 kPa. One of the sensors was at the midpoint of the palate, i.e. at the same position where our assessment took place. This is the point referred to in this work as  $P(0)$ . Thus it is reasonable to compare these values with the theoretical values of the mathematical model. The value of 10 kPa is absolutely within the range of these pressures but it has to be kept in mind, that these values were measured during destructive processes and not during normal evaluation of an object.

The result of the comparison of  $225\ \mu\text{m}$  and  $250\ \mu\text{m}$  is contradictory to the postulation of an upper limit. The disks are even thicker and harder to bend than the preceding pair but differentiation was possible for these two disks. Recapitulating the current findings of the standard trials it can be concluded that for the lower end of the range (reaching up to  $125\ \mu\text{m}$ ) differentiation of  $25\ \mu\text{m}$  was possible as well as it was for the upper end (above  $200\ \mu\text{m}$ ) but the middle range (extending from  $125$  to  $200\ \mu\text{m}$ ) remained impossible. The results mentioned above strongly suggest the existence of a second discrimination processes, schematic illustration of both processes in Figure 2.11.

Thin disks are aligned with the palate through pressure application of the tongue. However, thicker disks cannot be significantly deformed because of their larger structural stiffness. In contrast, these will be impressed into the tongue and therefore generate a deformation, allowing discrimination in this manner. The dynamics of the

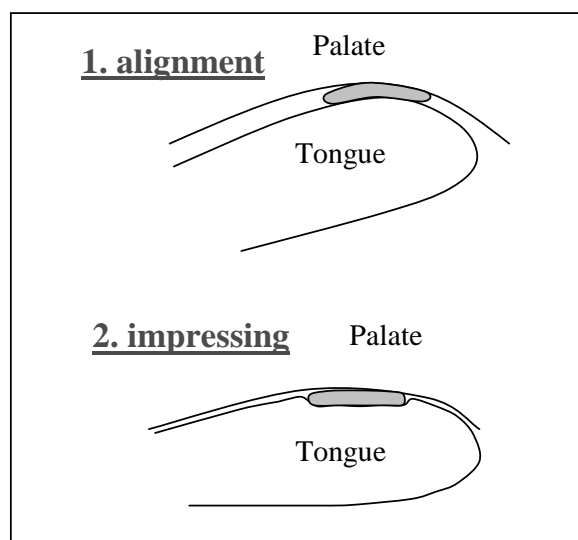


Figure 2.11: Processing of materials between tongue and palate depending on the thickness of the material: 1) For thin or flexible materials, 2) for thick or stiff materials where bending is not possible with the forces present in the mouth.

process can be neglected with respect to the disks. The materials PET, Teflon, and the whey protein-glycerol films, show purely elastic behavior. The dynamics of the process only becomes important for the stimulation of the mechanoreceptors, see below, since some are sensitive to dynamic stimulation and others to static stimulation.

The second interval results from failure of both detection processes. Disks originating from the second interval are too thick to be aligned whereas at the same time they are not thick enough to significantly deform the tongue so that mechanoreceptors sensitive for static stimulation remain unexcited. When the disks are pressed on the tongue they first compress the rather soft papillae before they reach the less compliant tongue body (for an illustration of the papillae on the tongue see Figure 2.12 or Kullaa-Mikkonen & Sorvari (1985)).

The compression of the tongue can be thought of as a strain-hardening material behavior. The measurement system is only sensitive again once the soft papillae are compressed and the rather hard and solid tongue body (Smith & Kier, 1989), which can be considered as incompressible (Napadow et al., 1999), evaluates the load intensity.

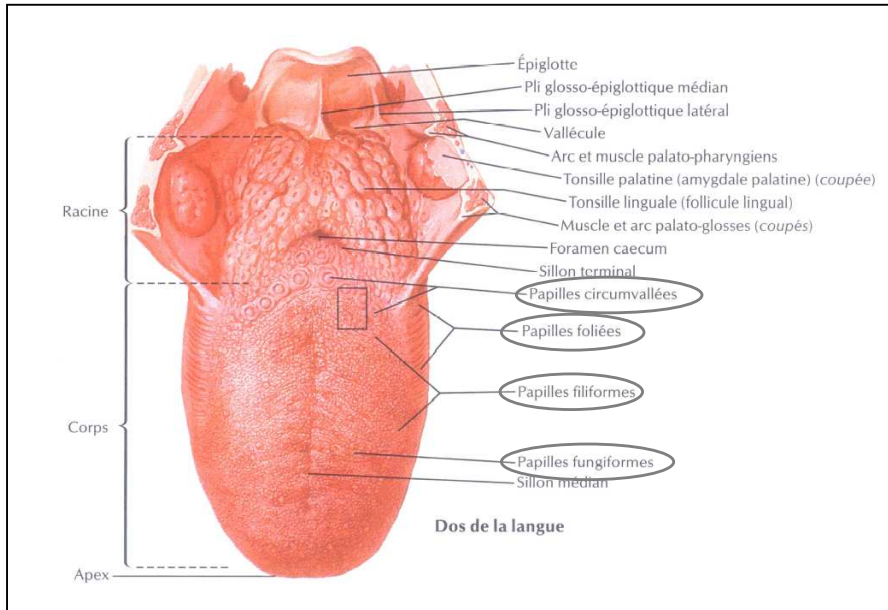


Figure 2.12: Dorsum of the tongue with its four types of papillae (Netter & Kamina, 2004).

Since the papillae have a height from  $20 \mu\text{m}$  up to  $200 \mu\text{m}$  on the tongue (Kobayashi et al., 1994), the anatomical data is consistent with the idea that the tongue can be imagined to behave like a strain-hardening material. Of course it has to be kept in mind that the tongue is an at least two-composite (tongue body and papillae) body, therefore, the term strain-hardening is technically not absolutely correct but illustrates the process.

When looking at the neurology of the tongue the existence of the processes seems logical, too (see Figure 2.13). Three of the four types of mechanoreceptive afferent neuron types present in the glabrous skin are existent in the mouth. These can be classified according to their reaction speed: two slowly adapting nerve endings, which end in Merkel cells (SA 1) and Ruffini corpuscles (SA 2, both located in the medium layer under the surface) and one type of rapidly adapting ones (RA 1), which end in Meissner cells (closest to the surface), or also to the size of their receptive fields (see Table 2.14). Pacinian corpuscles (RA 2) are not found in the oral mucosa (Johansson et al., 1988; Jacobs et al., 2002).

According to Johnson (2001) Merkel cells are sensitive to the detection of local stress-

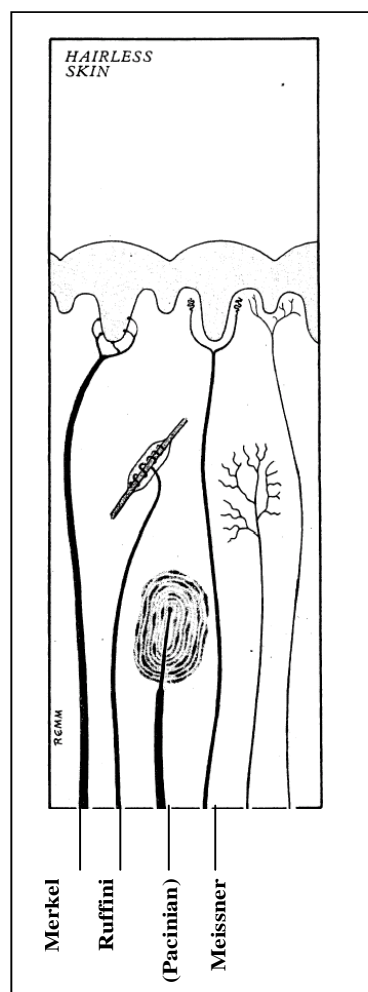


Figure 2.13: Mechanoreceptors in the oral mucosa are identical to mechanoreceptors in the glabrous skin except for the Pacinian corpuscles (Williams et al., 1998).

strain field differences, perception of edges, corner, and curvature, which is consistent with the possibility to detect differences in diameter of round objects. At the same time they manage to detect indentation depths of at least  $1500 \mu\text{m}$  possibly involving them in the thickness determination process of very thick disks or other objects where deformation of the underlying tongue body is relevant. Rapidly adapting nerve endings such as Meissner corpuscles begin to saturate at indentation depths of  $100 \mu\text{m}$  and are insensitive to indentation above  $300 - 400 \mu\text{m}$ . They detect velocities and are sensitive to dynamic deformation. This represents a strong indication for possible involvement of the Meissner corpuscles in the alignment process. Thus the anatomical and neurological

Table 2.14: Classification of the mechanoreceptors due to perception field size and adaptation speed (Pacinian corpuscles are not present in the oral mucosa).

adaptation properties	receptive field	
	small	large
rapid	Meissner cells	<i>Pascinian corpuscles</i>
slow	Merkel cells	Ruffini corpuscles

situation is conform with the concept of an existence of these two processes.

Returning to the intervals previously mentioned, all disks coming from the second interval and differing by 25  $\mu\text{m}$  (and disposing of an elastic modulus of 480 MPa) should fall into a range, where the two processes mentioned fail and no differentiation is possible. Also all disks of harder materials but thinner, as this results in the same structural resistance (geometry and material stiffness) and load intensities, should fall into this range. In order to further confirm the concept of the existence of two different detection mechanisms the following complementary study was undertaken.

The sensory study for the insecure range was reinvented. Disks with 150  $\mu\text{m}$  and 180  $\mu\text{m}$  thickness made from FEP with an elastic modulus of 480 MPa were assessed by a panel of testers. It could be confirmed that disks in this range cannot be distinguished due to the previously mentioned reasoning. These characteristics can be challenged by changing the structural stiffness through choice of stiffer or more compliant materials (see Table 2.13).

A two-fold confirmation of the hypothesis was carried out. On the one hand for a material, here PET, with a much higher elastic modulus (2060 MPa) distinction between the same two disks of 150 and 180  $\mu\text{m}$  should not be possible. Alignment is actually not possible even for much thinner disks, and in addition to that the disks are not thick enough to deform the tongue sufficiently. The required normal stresses for alignment exceed physiological possible values in the human mouth. For a disk (250  $\mu\text{m}$  thickness, 10 mm diameter) a maximum load intensity of 15 kPa (edge) is

required, when calculated from equation 2.24. This is not likely to occur as previously described.

Both, the standard and the stiffer pair, led to the conclusion that the disks could not be distinguished. Thus, these two results support the hypothesis that the disks are too stiff to be aligned with the palate by the tongue and not thick enough to generate a sufficiently large deformation of the tongue body.

This being an indirect verification, direct proof was given by repeating the same pair (150 versus 180  $\mu\text{m}$ ) with a more compliant material. This reduction in structural resistance (through change of the material stiffness) should allow the alignment of the previously not differentiable pair of disks to the palate. Thus, this pair of disks should be differentiable. A disk of known diameter and thickness (thickness at the upper end of the insecure interval) was taken and the force needed to bend a much thinner disk (from the first interval) of the standard material was applied. The elastic modulus was unknown and needed to be determined so that this process was possible. This logically resulted in a much lower modulus than the original (480 MPa) and was calculated as 30 MPa. A material disposing of 90 MPa was the most compliant and still manageable that could be found. Disks were prepared and sensory tests were carried out (see Table 2.13). Differentiation was possible due to the higher compliance of the disks, which permitted alignment. This means that for 30 MPa the trial would also work if the material was available.

Therefore, the experiments with the stiffer disks confirm the hypothesis by showing the impossibility to differentiate these two disks. The more flexible disks also confirm it by showing that differentiation was possible despite the thickness of the disks when the necessary compliance was provided. Of course this does not necessarily imply that detection takes place by these means but until now no other approach has managed to explain the detection processes.

The question remains how the body handles the appearance of this gap between the two detection processes. Investigations of Young's moduli of, e.g. different cheeses, which are considered as crushable between tongue and palate, showed that they have

Young's moduli in the range of several hundred kPa (Goh & Charalambides, 2003). This is low compared to the 90 MPa used for the more flexible film. According to Steffe (1992) other foods' Young's moduli are in this range as well. (Cooked) Carrots for example have a Young's modulus of 20 - 40 MPa, potatoes of 6 - 14 MPa, peach of 2 - 20 MPa, and bananas of 8 - 30 MPa. This shows that during normal textural evaluation of food the insecure range is normally not used when evaluating between tongue and palate. Trials carried out by Takahashi & Nakazawa (1991b) with gelatin gels between tongue and palate showed that samples which cannot be crushed between tongue and palate are moved towards the teeth for biting, therefore, confirming the statement above. The biological pressure limit for this transfer is 20 - 30 kPa according to Takahashi & Nakazawa (1991a).

The range of materials, which are normally introduced into the mouth is limited in comparison to the materials, which come into contact with the finger-palm system. The fact that the insecure range does not exist for the finger-palm system as stated previously agrees with this. Based on the belief that the insecure range results from the presence of papillae it is evident that there is no insecure range for the finger-palm system since this does not dispose of papillae.

# Chapter 3

## Perception of suspensions by the tongue-palate system (fluid mechanical model)

A theoretical and a practical approach are taken in order to investigate textural phenomena such as grittiness. The theoretical approach consists of a mathematical model, which is described in the following. The mechanical model is discussed in Chapter 4.

### 3.1 Introduction to the mathematical model

It seems reasonable to use squeeze flow for the investigation of textural evaluation behavior because three of the basic test procedures human beings use before consuming a foodstuff rely on the principles of compression: evaluation between the fingers, biting with the teeth for solid materials, or squeezing between tongue and palate in the case of crushable, i.e. liquid materials. In addition, food materials are often very viscous or might have yield stresses. Squeeze flow seems to be the most reasonable approach in comparison with traditional rheological measurements (Yates et al., 2001). Although the rheological properties of the sensory system itself, i.e. softness of the

tongue, should be taken into account, a parallel plate model, representing tongue and palate with rigid plates, is used. The reason for this is that the rheological properties of the tissues involved are complex and difficult to characterize mathematically and the interactions between two soft materials presents a contact stress problem between two viscoelastic materials of irregular shape, therefore a simple analytical solution is highly improbable (Campanella & Peleg, 1988). Furthermore, other authors argue (see Chapter 1) that the tongue can be regarded as a static body due to consistence of muscle tissue (Smith & Kier, 1989). The idea to describe fluids in the human mouth with the help of two parallel plates has been used before by, e.g. Weipert et al. (1993). He forced two parallel plates with a fluid between them to move towards each other by application of a normal force to the bottom plate. This results in shear and elongation of the fluid layers. For fluids obeying Ostwald-de Waele's power law, e.g. pseudoplastic substances, shear stresses and velocity fields can be calculated.

The existing models have been applied to pure fluids, but not to particle containing substances such as suspensions. The perception of the latter is in the center of interest of this Chapter. Almost all foods contain particles and the presence of particles in food affects the perception of sensory attributes. While some particles are obviously present such as pits in berries, others are small, or soft and hardly noticeable, such as oil droplets in mayonnaise. Large particles in low concentrations are likely to be perceived as separate entities, e.g. seeds in a watermelon. Conversely, small particles (e.g. 4 - 7  $\mu\text{m}$  (Kilcast & Clegg, 2002; Hough et al., 1988)) of high concentrations are more likely not to be noticed separately, but instead to have an effect on the texture of the product, e.g. graininess (Engelen, 2004) or even creaminess (Kilcast & Clegg, 2002). For the latter case it is possible that the particles and their perturbations in the fluid influence each other, therefore, creating a "bulk" impression of the fluid rather than a heterogeneous perception as is the case for larger particles. The investigation of these perturbations in comparison to unperturbed fluids is the main aim of this Chapter.

The sensitivity of the mouth to particles suspended in liquids relies on its ability to assess shape, size, and surface texture. Information on the significance of the various

oral parts in oral size perception and sensitivity is required to understand their role in the control of bite size, swallowing, and perception of food. The investigation of these limits is discussed in the first part of this work (see Chapter 2).

The shape of the particles also seems to play an important role as demonstrated by Kilcast & Clegg (2002) and Engelen et al. (2005). Although the detectable particle size according to confectionery research is around  $25 \mu\text{m}$ , particles of  $10 \mu\text{m}$  can produce a gritty sensation due to their sharp edges, e.g. alumina particles in tooth pastes. De Wijk & Prinz (2005), who investigated friction in comparison with particle inclusion, also showed that the particle shape has a significant influence; spherical particles show less friction than similarly sized sharp particles. In contrast Kilcast & Clegg (2002) claim that the factor contributing most to grittiness is concentration, followed by type of aqueous phase and then particle size, not mentioning the shape at all. Nevertheless the aspect of shape should be kept in mind when modeling the stress fields around the particles. In the modeling carried out in this work only spherical particles are considered to assure the model works before more complexity is added. Nevertheless, it has to be ensured that the particles are equally buoyant.

An established and repeatedly used model is applied to describe the pressure and velocity field between the plates with and without particles. The modeling starts with an investigation of the unperturbed flow field, represented by the pressure form of the Stefan equation, see Section 3.2.1 or Stefan (1874) for the original work and Engmann et al. (2005) for a more recent description of the theory. This equation takes into account: the velocity of the top plate, the viscosity of the fluid not containing any particles, the plate distance, and the radius of the plates. As a next step the point force of one particle is determined by Faxen's first law (see Section 3.2.2) as derived by Brenner (1964). Faxen's law is valid for an arbitrary flow field, where the particle is convecting with the fluid. Since the particle is small the force is considered as a point force. The theory relies on the fact that close to the particle the fluid is disturbed, but at infinity the disturbance decays. Finally the flow and pressure fields induced by the Faxen point force are investigated with the help of Green functions (see Section 3.2.3 and Blake & Chwang (1974) for the original work). They allow mapping of a known

force, which is the point force, to the associated velocity field. Here two cases are considered: 1) the free space Green function and 2) the bounded Green function. “Free space” refers to the condition that the perturbation of the fluid caused by the point force has to decay at infinity, therefore not assuming any boundaries such as the bottom plate. Up to here this is a linear problem, meaning the solutions can be superposed. Faxen’s law and the Green functions work for any arbitrary flow and velocity field. The specific flow field in this case is the one described by the Stefan equation. The free space Green function cannot satisfy the boundary condition of the plate or another particle by simple superposition. This is why the bounded Green function has to be considered since it can take this condition into account. For both Green functions velocity and pressure fields are determined. The total stress tensor  $\sigma_{ij}$  is the sum of the fluid pressure  $p$  (which can be obtained directly from either Green’s function, this is shown later) multiplied with the Kronecker delta  $\delta_{ij}$  and the viscous stress tensor  $\tau_{ij}$ . The latter can be determined once the velocity is known by taking its derivative and multiplying it by twice the viscosity. Other studies dealing with particle-containing flow fields were conducted by Nirschl (1994), Zima et al. (2005) and Hartmann et al. (2003).

For the practical approach: the bottom plate of the experimental setup is equipped with a sheet pressure sensor as described further on. It can only sense normal stresses. Therefore, when taking the balance for all vertical force components only the  $zz$  component of the total stress tensor remains, since there are no other vertical components. Once these normal stresses are determined they can be added to the ‘background’ pressure field (the normal stress resulting from the presence of fluid, i.e.  $P$  and  $\tau_{ij}^{\text{St}}$ ), not containing any particles, is considered as background pressure) determined with the help of the Stefan equation in order to know the overall pressure profile. This profile is presented on the bottom plate. An experimental verification with a Tekscan pressure sensor, two parallel plates and a strain frame, onto which the plates are mounted, follows (see Chapter 4). For a schematic illustration of the work flow see Figure 3.1.

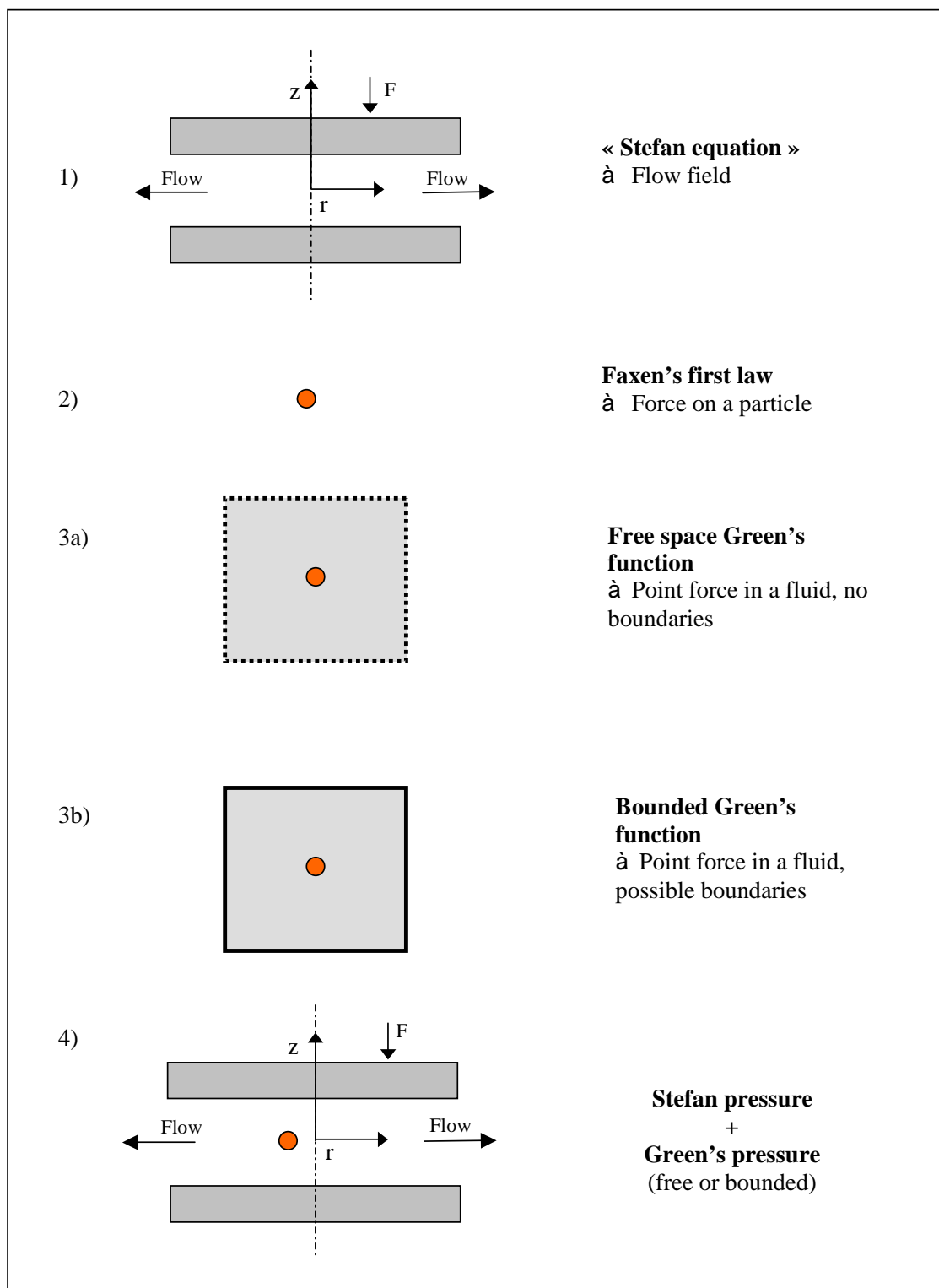


Figure 3.1: Overview of the mathematical approach illustrating the influence of the different equations and their superposition.

### **Novelty and reliability of the approach**

In the current approach, a theoretical description of local hydrodynamics of a particle at low Reynolds numbers based on Green functions is employed. This concept has been formulated by Batchelor (1970), who for example investigated the viscosity of suspensions and the average effective stress (mean field theory) due to the particles. This has been verified extensively, see Pusey (1991), Underwood et al. (1994), or Segre et al. (1995). Blake (1972) used the same models for the investigation of the locomotion of microorganisms in low Reynolds number flow. He also dealt with mean velocity fields due to the organisms but did not develop a singular approach. In a combined theoretical and experimental approach this has more recently been used by Hartmann et al. (2006) to investigate the influence of ciliate organisms on the surrounding flow field. In this case the force the particles exert was theoretically obtained on the basis of micro-Particle Image Velocimetry (PIV) data, which then allowed determination of the force exerted by the micro-organism onto the fluid from the generated flow field. The theoretical forces were obtained through correlation of the experimental data with the established concept from Blake (1972).

In the approach discussed in the following the unperturbed flow field is given a priori and described through the Stefan equation. The force due to a particle is determined with the help of Faxen's law. The values of the forces determined by Hartmann et al. (2006) serve as a reasonable comparison for the force values obtained in our study and the judgement of their reasonability. They are discussed below.

Apart from the technical aspects previously mentioned the most outstanding characteristic of current approach concerning novelty is the use of Faxen's law and Green functions in a context related to oral fluid dynamics. Here, local particle hydrodynamics are used in order to predict pressure perturbations on distant oral surfaces. Both, the Faxen law as well as the Green functions, are well established concepts but are used here for the first time. Hence, all the building blocks of the model have been extensively verified but they have not previously been assembled.

## 3.2 Mathematical methods

Within the work flow illustrated in Figure 3.1 different coordinate systems are used. For clarification these are explained beforehand with the help of Figure 3.2. The cylindrical polar coordinate system in  $rz$ -coordinates placed: at the line of symmetry between the plates is used in the Section describing the Stefan model. There are several  $xyz$ -coordinate systems whose origins are placed on the line of symmetry ( $X_1, Y_1, Z_1$ , this is used for Faxen's law), at the center of the bottom plate ( $X_2, Y_2, Z_2$ , relevant for the bounded Green function), and at the center of a particle ( $X_3, Y_3, Z_3$ , this being of relevance for the free space Green function).

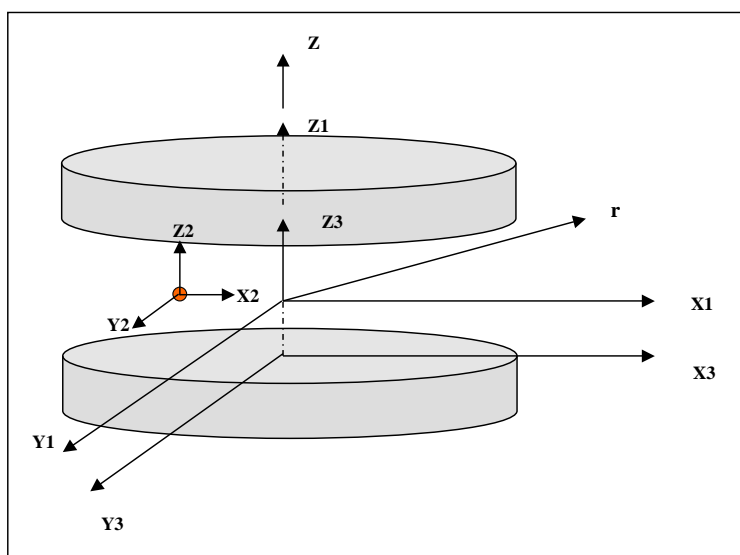


Figure 3.2: Coordinate frames used within the calculations: origin based on the line of symmetry ( $X_1, Y_1, Z_1$  and cylindrical polar  $r, z$ ), origin based at the center of the particle ( $X_2, Y_2, Z_2$ ), and origin at the center of the bottom plate ( $X_3, Y_3, Z_3$ ).

### 3.2.1 Newtonian fluid between parallel moving plates:

#### *Stefan model*

The first step in the model is the description of the unperturbed squeeze flow between parallel plates as described by Stefan (1874). It is assumed that two disks of radius  $R_P$  are brought together, forcing out the incompressible fluid between them. The disk separation is  $2d(t)$  at time  $t$ , and the velocity at which the top plate moves towards the bottom plate is  $\dot{d}$ . The fluid pressure  $P$  at the edges of the disks, where the fluid exists, is assumed to be zero (see Figure 3.3).

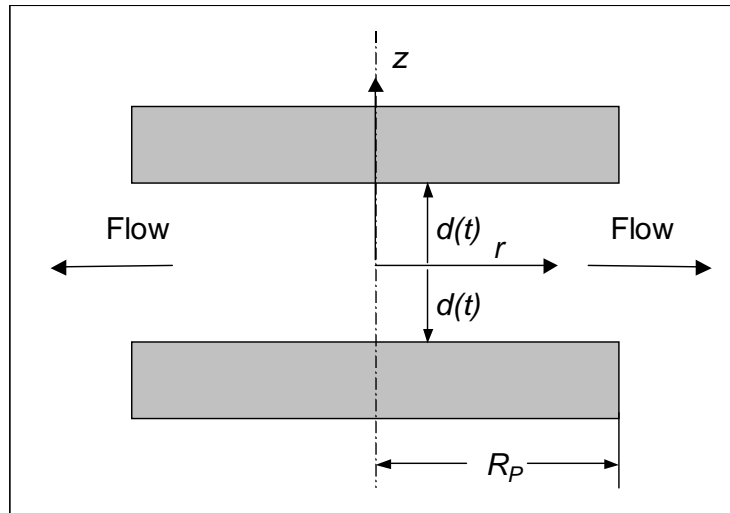


Figure 3.3: Squeeze flow scheme.

Stefan (1874) was one of the first to describe squeeze flow, although his original study dealt with adhesion. The actual Stefan equation deals with the resulting forces during the squeeze flow, whereas here the main focus is on the pressure distribution as a function of the fluid viscosity  $\eta$ , velocity of the upper plate  $\dot{d}$ , radius of the plates  $R_P$ , and the radial distance  $r$  from the center of the plate. The so-called Stefan equation is derived in the following. Starting from the Navier-Stokes equation (Pnueli & Gutfinger, 1992), which is valid for Newtonian fluids under the assumption that they are incompressible and the flow isotherm,

$$\frac{D\mathbf{v}}{Dt} = \frac{\partial\mathbf{v}}{\partial t} + \mathbf{v} \bullet \nabla\mathbf{v} = F_g - \frac{1}{\rho} \nabla P + \nu \nabla^2\mathbf{v}, \quad (3.1)$$

where  $\mathbf{v}$  is the fluid velocity,  $P$  the hydrostatic pressure,  $\nu$  the kinematic viscosity (multiplied with the density  $\rho$  this leads to the dynamic viscosity  $\eta$ ), and  $F_g$  the gravitational force. Bold letters indicate vectors. It is assumed that  $d \ll R_P$  ( $d$  refers to half the gap between the plates). This assumption allows simplification of the Navier-Stokes equation, which is based on similar considerations as those in classical lubrication theory (Pnueli & Gutfinger, 1992). The following three terms can be ignored:

1.  $F_g$  because it is small in comparison with the other forces,
2.  $\mathbf{v} \bullet \nabla \mathbf{v}$  because the Reynolds number  $Re$  is small, i.e. high viscosity and small inertial forces,
3.  $\frac{\partial \mathbf{v}}{\partial t}$  because the changes are taking place slowly, i.e. the acceleration is small.

This leaves

$$-\frac{1}{\rho} \nabla P + \nu \nabla^2 \mathbf{v} = 0 \quad (3.2)$$

and therefore,

$$\nabla P = \eta \nabla^2 \mathbf{v}, \quad (3.3)$$

which is the Stokes equation. This equation needs to be expressed in cylindrical polar coordinates ( $r, z$  with  $\theta$  symmetry) with  $z = 0$  at the line of symmetry between the two plates. With  $P$  being a scalar, Bird et al. (1960) give

$$\frac{\partial P}{\partial r} = \eta \left( \frac{\partial}{\partial r} \left( \frac{1}{r} \frac{\partial}{\partial r} (r v_r) \right) + \frac{1}{r^2} \frac{\partial^2 v_r}{\partial \theta^2} - \frac{2 \partial v_r}{r^2 \partial \theta} + \frac{\partial^2 v_r}{\partial z^2} \right) \quad (3.4)$$

in the  $r$ -direction. For the  $\theta$ -direction the following equation is obtained.

$$\frac{1}{r} \frac{\partial P}{\partial \theta} = \eta \left( \frac{\partial}{\partial r} \left( \frac{1}{r} \frac{\partial}{\partial r} (r v_\theta) \right) + \frac{1}{r^2} \frac{\partial^2 v_\theta}{\partial \theta^2} + \frac{2 \partial v_r}{r^2 \partial \theta} + \frac{\partial^2 v_\theta}{\partial z^2} \right) \quad (3.5)$$

To the system of equations for  $\mathbf{v}$  and  $P$  it belongs

$$\frac{\partial P}{\partial z} = \eta \left( \frac{1}{r} \frac{\partial}{\partial r} \left( r \frac{\partial v_z}{\partial r} \right) + \frac{1}{r^2} \frac{\partial^2 v_z}{\partial \theta^2} + \frac{\partial^2 v_z}{\partial z^2} \right). \quad (3.6)$$

For the axisymmetric squeeze flow considered in this study the circumferential velocity  $v_\theta$  is equal to zero because the plates do not rotate. Therefore all terms containing derivatives in the  $\theta$ -direction vanish.

The three equations above together with the **continuity equation**

$$\nabla \cdot \mathbf{v} = \left( \frac{1}{r} \frac{\partial(r v_r)}{\partial r} + \frac{1}{r} \frac{\partial v_\theta}{\partial \theta} + \frac{\partial v_z}{\partial z} \right) = 0 \quad (3.7)$$

are sufficient to solve the flow problem with the four dependent variables  $v_r, v_\theta, v_z$ , and  $P$  (Pnueli & Gutfinger, 1992).

As a next step a **non-dimensionalization** is carried out, in which the following reduced variables are defined

- $r = r^* R_P$
- $z = z^* d(t)$
- $v_z = \dot{d}(t) v_z^*$
- $v_\theta = v_\theta^* \dot{d}(t)$ .

Dimensionless forms of the variables are marked with an asterisk. The dimensionless forms of  $v_r$  and  $P$  are not shown because they are not immediately apparent but are determined at a later point in the analysis, see below. The continuity equation in its dimensionless form (still containing  $v_r$ ) furnishes the scaling for  $v_r$ .

$$\nabla^* \cdot \mathbf{v}^* = \frac{1}{r^* R_P} \frac{\partial(r^* R_P v_r)}{\partial(r^* R_P)} + \frac{\partial(\dot{d}(t) v_z^*)}{\partial(d(t) z^*)} = 0 \quad (3.8)$$

Simplification leads to

$$\frac{1}{R_P r^*} \frac{\partial(r^* v_r)}{\partial r^*} + \frac{\dot{d}(t)}{d(t)} \frac{\partial v_z^*}{\partial z^*} = 0. \quad (3.9)$$

Multiplication with  $\frac{d(t)}{\dot{d}(t)}$  on both sides gives

$$\frac{d(t)}{\dot{d}(t)} \frac{1}{R_P r^*} \frac{\partial(r^* v_r)}{\partial r^*} + \frac{\partial v_z^*}{\partial z^*} = 0. \quad (3.10)$$

Solving for  $v_r$  leads to the suggested scaling for  $v_r$ .

$$v_r = v_r^* \dot{d}(t) \frac{R_P}{d(t)} \quad (3.11)$$

By substituting  $v_r$  in equation (3.10) the non-dimensional form of the continuity equation can be obtained

$$\frac{d(t)}{\dot{d}(t)} \frac{1}{R_P r^*} \frac{\partial(r^* v_r^* \frac{d(t)}{d} R_P)}{\partial r^*} + \frac{\partial v_z^*}{\partial z^*} = 0, \quad (3.12)$$

which leads to

$$\frac{1}{r^*} \frac{\partial(r^* v_r^*)}{\partial r^*} + \frac{\partial v_z^*}{\partial z^*} = 0 \quad (3.13)$$

after simplification.

The pressure maximum is on the central axis. From equation (3.6) it follows that the pressure change in the  $z$ -direction depends only on  $r$ . At  $r = R_P$  the pressure (total) equals the atmospheric pressure, implying that the dynamic pressure is zero here.

$$\frac{\partial P}{\partial(r^* R_P)} = \eta \left( \frac{\partial}{\partial(r^* R_P)} \left( \frac{1}{r^* R_P} \frac{\partial(r^* R_P R_P \dot{d}(t) v_r^*)}{\partial(r^* R_P) d(t)} \right) \right) + \eta \frac{\partial^2 \left( \frac{R_P \dot{d}(t) r^* v_r^*}{d(t)} \right)}{\partial(d(t) z^*)^2} \quad (3.14)$$

Expanding this expression and dividing it by  $\frac{R_P \dot{d}(t)}{d(t)^3}$  leads to the following equation, which makes it possible to see that  $P$  has to be scaled with  $P = \frac{\eta R_P^2 \dot{d}(t)}{d(t)^3}$  to become dimensionless.

$$\frac{\partial P d(t)^3}{\eta R_P^2 \partial r^* \dot{d}(t)} = \frac{d(t)^2}{R_P^2} \frac{\partial}{\partial r^*} \left( \frac{1}{r^*} \frac{\partial(v_r^* r^{*2})}{\partial r^*} \right) + \frac{\partial^2(v_r^* r^*)}{\partial z^{*2}} \quad (3.15)$$

Substitution of  $P$  in equation (3.15) yields equation (3.16), which is the pressure in the  $r$ -direction in dimensionless form.

$$\frac{\partial P^*}{\partial r^*} = \left( \frac{d(t)}{R_P} \right)^2 \frac{\partial}{\partial r^*} \left( \frac{1}{r^*} \frac{\partial(v_r^* r^{*2})}{\partial r^*} \right) + \frac{\partial^2(v_r^* r^*)}{\partial z^{*2}} \quad (3.16)$$

In the next step a **perturbation analysis** is carried out. This means that every term in the equation is scaled with respect to a small dimensionless parameter, which in this case is  $\frac{d(t)}{R_P} = \varepsilon$ . In dimensionless form this leads to

$$\frac{\partial P^*}{\partial r^*} = \varepsilon^2 \frac{\partial}{\partial r^*} \left( \frac{1}{r^*} \frac{\partial(v_r^* r^{*2})}{\partial r^*} \right) + \frac{\partial^2(v_r^* r^*)}{\partial z^{*2}} \quad (3.17)$$

for equation 3.16.

This leaves the left hand side to be order 1, whereas the two terms on the right hand side are order  $\varepsilon^2$  and 1. Applying the same procedure to equation (3.6), i.e. expansion, non-dimensionalization and scaling with the small parameter  $\varepsilon$ , results in the following equation

$$\frac{R_P^2}{d^2(t)} \frac{\partial P^*}{\partial z^*} = \frac{d^2(t)}{R_P^2} \frac{\partial r^*(\partial v_z^*)}{r^* \partial r^*} + \frac{\partial^2 v_z^*}{\partial z^{*2}}. \quad (3.18)$$

Multiplication with  $\frac{d^2(t)}{R_P^2}$ , i.e.  $\varepsilon^2$ , brings forth

$$\frac{\partial P^*}{\partial z^*} = \varepsilon^4 \frac{\partial r^*(\partial v_z^*)}{r^* \partial r^*} + \varepsilon^2 \frac{\partial^2 v_z^*}{\partial z^{*2}}. \quad (3.19)$$

Omitting terms of the order  $\varepsilon^2$  and higher from equation (3.19) leads to  $\frac{\partial P^*}{\partial z^*} = 0$  and the conclusion that the pressure is only a function of  $r$ . This leaves only equation (3.16), i.e. the scaled equation in the  $r$ -direction,

$$\frac{\partial P^*}{\partial r^*} = \frac{\partial^2 (v_r^* r^*)}{\partial z^{*2}} = r^* \frac{\partial v_r^*}{\partial z^{*2}}. \quad (3.20)$$

In the following steps the above equation is integrated with respect to  $z$  in order to obtain  $v_r^*$ . The left hand side is only dependent on  $r$ , whereas the right hand side is dependent on  $z$ . Hence, both sides have to be constant and the left hand side of the equation is therefore set equal to  $k$ . Integration of the previous integration leads to

$$k z^* + C = \frac{\partial (v_r^* r^*)}{\partial z^*}, \quad (3.21)$$

followed by

$$\frac{k}{2} z^{*2} + C z^* + B = v_r^* r^*, \quad (3.22)$$

when integrated again. The following boundary conditions are now applied

$$v_r^* = 0 \text{ at } z = 1, \quad (3.23)$$

i.e. the velocity at the plate is zero (see Figure 3.3), and

$$\frac{\partial (v_r^*)}{\partial v_z^*} = 0, \text{ for } z = 0, \quad (3.24)$$

i.e. the maximum velocity is at the center.

This leads to  $C = 0$  and  $B = -\frac{1}{2}k$ . When substituting  $k$  by  $\partial P^*/\partial r^*$ , this gives the radial velocity profile. It is the equation later referred to as Stefan velocity but in its dimensionless form.

$$v_r^* = \frac{1}{2r^*} \frac{\partial P^*}{\partial r^*} (z^{*2} - 1) \quad (3.25)$$

As a last step the **overall mass balance**, i.e. the ingoing flow (left hand side) has to be equal to the outgoing flow (right hand side), is taken, first in dimensional units, afterwards in dimensionless form.

$$\dot{d}(t) \pi r^2 = \int_{-d(t)}^{d(t)} 2v_r \pi r dz \quad (3.26)$$

When replacing  $v_r$  by  $R_p r^* \frac{\dot{d}(t)}{d(t)} v_r^*$ ,  $z$  by  $d(t) z^*$ , and  $r$  by  $R_p r^*$  it becomes evident that

$$\dot{d}(t) \pi r^2 = \int_{-1}^1 2\pi r^* R_p R_p r^* \frac{\dot{d}(t)}{d(t)} v_r^* d(t) dz^*. \quad (3.27)$$

After cancellation of reappearing terms and substitution of the right hand side of equation (3.25) for  $v_r^*$  this gives

$$r^* = \frac{\partial P^*}{\partial r^*} \int_{-1}^1 (z^* - 1) dz^* = \frac{\partial P^*}{\partial r^*} \left[ \frac{z^{*3}}{3} - 1 \right]_{-1}^1, \quad (3.28)$$

resulting in

$$\frac{dP^*}{dr^*} = \frac{3}{2} r^*. \quad (3.29)$$

Integration of this equation from 0 to  $r^*$  with respect to  $r^*$  and solving for  $P^*$  leads to

$$P^* = \frac{3}{2} \frac{1}{2} r^{*2} + C. \quad (3.30)$$

Re-substitution of the dimensions gives the final equation, referred to in the following as the **Stefan pressure** equation.

$$P(r) = \frac{3\eta \dot{d}(t)}{4d^3(t)} (r^2 - R_P^2) \quad (3.31)$$

This equation is in needed in its dimensional form because once the presence of a particle is discussed, a new length scale enters the system. In this case it is not evident, which length scale (particle or fluid) needs to taken. The exact non-dimensional form can be found in Burbidge & Servais (2004). The non-dimensionalization discussed previously is necessary in order to carry out the perturbation analysis and determine the terms with least significance.

It can be seen that the resulting pressure profile should show a parabolic form with respect to the radius, which is also demonstrated in the experimental part of this Chapter. Redimensionalizing equation (3.25) gives

$$v_r = \frac{1}{2\eta} \frac{\partial P}{\partial r} (z^2 - d(t)^2). \quad (3.32)$$

Differentiation of equation (3.31) with respect to  $r$  and substitution of  $\partial P/\partial r$  with the obtained result in equation (3.32) gives the **Stefan velocity** in the  $r$ -direction.

$$v_r = \frac{3r \dot{d}(t)(z^2 - d(t)^2)}{4d^3(t)} \quad (3.33)$$

The velocity in the  $z$ -direction can be obtained when substituting  $v_r$  into equation (3.7), which is the continuity equation, and then integrating and solving for  $v_z$ . Solving the obtained equation for  $\partial v_z/\partial z$  gives the the  $z$ -component of the velocity gradient.

$$\frac{\partial v_z}{\partial z} = -\frac{3 \dot{d}(t)(z^2 - d(t)^2)}{2d(t)^3} \quad (3.34)$$

Multiplication of this gradient by  $2\eta$  results in the viscous stress tensor  $\tau_{ij}$  according to the constitutive equation for incompressible Newtonian fluids  $\tau_{ij} = \frac{1}{2} \eta (v_{i,j} + v_{j,i})$  (Pnueli & Gutfinger, 1992).

$$\tau_{zz}^{\text{ST}} = 2\eta \frac{\partial v_z}{\partial z} = -3\eta \frac{\dot{d}(t)(z^2 - d(t)^2)}{d(t)^3} \quad (3.35)$$

This normal stress  $\tau_{zz}^{\text{ST}}$  (in the  $zz$ -direction) is needed additionally to the Stefan pressure when the pressures and normal stresses of the fluid and the particle are superposed. Since the stress is only measured at the plate,  $z = \pm d$ , the stress component vanishes and is therefore not further considered in the following calculations.

### 3.2.2 Point force: Faxen's first law

The objective of this Section is to calculate the force on a small, solid (rigid) sphere with radius  $a$  in an arbitrary velocity field. Furthermore the sphere (particle) has to be nonpolar and biochemically inert.

The Faxen law is valid for non-uniform flows. Faxen's first law (Deen, 1998) provides an expression for the force on a particle in an unbounded flow field in terms of the unperturbed velocity far from the particle (sphere), i.e.  $\mathbf{v}_\infty$ , and the force given by Stokes' law, i.e.  $F_{\text{Stokes}} = 6\eta\pi a v_p$  ( $v_p$  = particle velocity). The notation  $|_0$  refers to the origin of the coordinate system, i.e. the center of the particle (Figure 3.2). The complete Faxen equation is the following

$$\mathbf{F}_{\text{Faxen}} = 6\pi\eta a (\mathbf{v}_\infty|_0 - \mathbf{v}_p) + \eta\pi a^3 (\nabla^2 \mathbf{v}_\infty)|_0. \quad (3.36)$$

This equation relies on the fact that the particle can freely rotate and that pure shear forces have no effect on particle displacement, in contrast squeeze flow does have an effect because it generates a pressure gradient. Because the flow discussed is low Re flow, the Stokes equation  $\nabla P = \eta\nabla^2 \mathbf{v}$  can be used to replace the Laplacian  $\nabla^2 \mathbf{v}_\infty$  by the pressure gradient  $\nabla P$ . This pressure gradient can for example be the one from the squeeze flow described above. The particle must in turn induce a disturbance velocity in the fluid due to the apparent relative velocity. Choosing to represent this particle effect on the fluid as a point force, Faxen's law allows the calculation of the magnitude of this point force. The density of the particle is identical to the density of

the fluid (equally buoyant), therefore, the particle convects at the speed of the fluid, which causes the first term on the right hand side of equation (3.36) to become zero, and leads to the following equation

$$\mathbf{F}_{\text{Faxen}} \simeq \eta \pi a^3 (\nabla^2 \mathbf{v}_\infty) |_0. \quad (3.37)$$

The velocity  $\mathbf{v}_\infty$  of the fluid at infinity equals the velocity  $v_r$  determined in the unperturbed flow field (i.e. Stefan velocity), and taking into account that  $\eta \nabla^2 \mathbf{v} = \nabla P$  for the above mentioned reasons, where  $P$  refers to the Stefan pressure (see Section 3.2.1), the following equation can be obtained, which is from now on referred to as the **Faxen force** equation

$$F_{\text{Faxen}} = \frac{3 a^3 \pi^2 r \eta \dot{d}(t)}{2 d(t)^3}. \quad (3.38)$$

This is the force experienced by a particle in the Stefan flow between the parallel plates when it is assumed to convect with the fluid. Only the pressure gradient matters, since the shear part vanishes because of the convection of the particle with the fluid. The force on the particle thus only depends on  $r$  and the instantaneous position and velocity of the plates. The force can be considered as a point force. The influence of this point force on the flow and pressure field is discussed in the following. Since the force is a vector in the  $r$ -direction it can easily be transformed into Cartesian coordinates and simplified when aligning  $r$  and  $x$ . This is more convenient when carrying out the subsequent vector analysis. Hence

$$F_x = \frac{3 a^3 \pi^2 x \eta \dot{d}(t)}{2 d(t)^3}, \quad (3.39)$$

where  $F_x$  is the force in Cartesian coordinates may these be plate or particle based as discussed further on since it is independent of  $z$ .

### Comparison of the obtained forces with data from the literature

The forces obtained through Faxen's law are used in the Green functions as point forces in order to obtain the pressure field variations. Hence, it is reasonable to compare these forces with values found by other authors before substituting them.

The forces, which are hydrodynamically induced, are the following

- $F_{\text{Stokes}} = 6 \pi \eta a v_{rel}$  Stokes' force
- $F_{\text{centrifugal}} = m \frac{v_{rel}^2}{a}$  centrifugal force
- $F_g = m g = \frac{4}{3} \rho_p \pi a^3 g$  gravitational force
- $F_{\text{buoyancy}} = m g = \frac{4}{3} \rho_{fl} \pi a^3 g$  buoyancy
- $F_{\text{Saffman}} = 6.46 a^2 \sqrt{\frac{\rho_{fl} \eta}{\dot{\gamma}}} \dot{\gamma} v_{rel}$  Saffman's force (lift from rotation)
- $F_{\text{Rubinow-Keller}} = \pi a^2 \rho_p v_{rel}^2$  Rubinow-Keller force (lift),

where  $\dot{\gamma} = \frac{v_{rel}}{a}$  is the shear rate. For the characteristic length the particle radius  $a$  is considered, and  $v_{rel}$  refers to the relative velocity between the particle and the fluid. For the centrifugal force the radius of curvature of the path line is assumed to be  $a$ . The indices  $fl$  and  $p$  refer to fluid and particle,  $m$  is the particle mass.

The above mentioned forces are calculated for the particle but not for the surrounding fluid. In all cases the fluid velocity is considered for  $v_{rel}$  leading to upper bound forces. For the centrifugal force this means, e.g. it is the absolute force on the particle, but it does not cause the particle to leave the path line. For the case that the fluid is considered forces such as Rubinow-Keller or Stokes would turn to zero due to the assumption of equal buoyancy, i.e. no density or velocity differences. On the contrary the Faxen force remains in both cases.

As previously discussed only the second part of Faxen's law remains. The first part, which is actually Stokes' law, is evaluated in the Stokes' force calculation. All forces mentioned above were determined for particles in fluids by Hartmann et al. (2006), who also investigated the relation of each force to the Stokes force, in order to determine the predominant forces. The parameters of both trials can be found in Table 3.1. Use of these parameters in the above mentioned force equations resulted in the forces and force ratios in Table 3.2.

Table 3.1: Parameters for force comparisons of current values with values from Hartmann et al. (2006) (the values in parentheses were not given by Hartmann et al. (2006), the plate distance and radius were set according to the current data, i.e. 2a and  $R_P$ ; the plate velocity was determined with help of equation (3.33).

<b>Value</b>	<b>Hartmann et al. (2006)</b>	<b>Current work</b>
fluid density $\rho_{fl}$ [kg/m <sup>3</sup> ]	998 (water)	938 (silicon oil)
fluid viscosity $\eta$ [Pas]	$10^{-3}$	30
particle density $\rho_p$ [kg/m <sup>3</sup> ]	1030 (yeast)	938 (equally buoyant material)
fluid velocity $v$ [m/s]	$2.5 \cdot 10^{-5}$	$3.75 \cdot 10^{-5}$ (from Stefan's equation)
particle mass $m$ [kg]	$4 \cdot 10^{-14}$	$4 \cdot 10^{-9}$
particle radius $a$ [m]	$3.5 \cdot 10^{-6}$	$10^{-4}$
plate distance $d$ [m]	( $7 \cdot 10^{-6}$ )	$2 \cdot 10^{-4}$
plate velocity $pv$ [m/s]	( $6.7 \cdot 10^{-5}$ )	$10^{-4}$

Table 3.2: Force values and ratios obtained in the current work in comparison with values from (Hartmann et al., 2006). In all cases the fluid velocity was taken for  $v_{rel}$  and equally buoyant particles were assumed, i.e.  $\rho_p = \rho_{fl}$ . All other values were as listed in Table 3.1. The influence of the supporting fluid was not considered, hence, leading to upper limit forces.

Force or Force relation	Hartmann et al. (2006)	Current work
Stokes	$1.7 \cdot 10^{-12}$ N	$2.1 \cdot 10^{-06}$ N
Faxen <sup>1</sup>	$8.6 \cdot 10^{-13}$ N	$1.8 \cdot 10^{-06}$ N
Faxen <sup>2</sup>	$4.2 \cdot 10^{-11}$ N	$8.7 \cdot 10^{-05}$ N
Buoyancy	$1.8 \cdot 10^{-12}$ N	$4.0 \cdot 10^{-08}$ N
Gravitational	$1.8 \cdot 10^{-12}$ N	$4.0 \cdot 10^{-08}$ N
Centrifugal	$1.2 \cdot 10^{-17}$ N	$2.6 \cdot 10^{-14}$ N
Saffman	$1.3 \cdot 10^{-19}$ N	$4.9 \cdot 10^{-16}$ N
Rubinow-Keller	$8.7 \cdot 10^{-18}$ N	$2.1 \cdot 10^{-14}$ N
Faxen <sup>1</sup> /Stokes	$5.2 \cdot 10^{-01}$	$8.3 \cdot 10^{-01}$
Faxen <sup>2</sup> /Stokes	$2.6 \cdot 10^{+01}$	$4.1 \cdot 10^{+01}$
Buoyancy/Stokes	$1.1 \cdot 10^{00}$	$1.9 \cdot 10^{-02}$
Gravitation/Stokes	$1.1 \cdot 10^{00}$	$1.9 \cdot 10^{-02}$
Centrifugal/Stokes	$7.0 \cdot 10^{-06}$	$1.3 \cdot 10^{-08}$
Saffman/Stokes	$8.1 \cdot 10^{-08}$	$2.3 \cdot 10^{-10}$
Rubinow-Keller/Stokes	$5.3 \cdot 10^{-06}$	$1.0 \cdot 10^{-08}$

<sup>1</sup> close to (less than  $10a$  away from) the center of the plate

<sup>2</sup> close to (less than  $10a$  away from) the edge of the plate

In Table 3.2 it can be seen that the predominant forces in the experimental flow carried out are the Stokes and Faxen force. All other forces are at least two orders of magnitude smaller, hence they are negligible for further estimations. Faxen and Stokes forces are roughly in the same order of magnitude. This allows use of the Faxen force as a point force in further estimations.

### 3.2.3 Point force (particle) in a fluid: *Green functions*

In this Section the stress distributions in a fluid due to a particle are determined. Once these are known they are added to the unperturbed flow field, determined previously (see Section 3.2.1) so that the pressure profile on the bottom plate is known. With the help of the Green functions the two components of the total stress tensor  $\sigma_{ij}$

$$\sigma_{ij} = -\delta_{ij}p + \tau_{ij} \quad (3.40)$$

can be determined. From now on the notation with indices is used to make use of the Einstein convention (Morrison, 2001). The hydrostatic pressure contributes directly to the total stress tensor, whereas the velocity field contributes through the deviatoric part of the stress tensor, i.e. through  $\tau_{ij}$ , based on the constitutive equation for incompressible Newtonian fluids (see above).

Once the total stress is determined, i.e. the particle has been considered, the Stefan pressure has to be added to the result of equation (3.40). This gives the complete stress exerted on the bottom plate by the fluid and the particle it contains (for the total stress see Section 3.2.5), when considered in the  $zz$ -direction. The influence of the particle should be seen as a disturbance in the Stefan pressure field.

A point force, e.g.  $F_{\text{Faxen}}$ , in a fluid induces a velocity disturbance. The function describing this is/are the Green function(s) and its/their solution(s) is/are called “Stokeslets” (Blake & Chwang, 1974). Blake & Chwang (1974) provide results for the pressure and velocity field, which are discussed in the following. Two situations have to be considered

1. the **free space Green** function assuming a disturbance, which decays at infinity
2. the **bounded Green function** taking into consideration possible boundary conditions such as the bottom plate.

Both equations define pressure and velocity fields due to a point force  $F$ , here  $F_{\text{Faxen}}$ . The free space Green function is discussed first before the bounded Green function is taken into consideration.

### 3.2.3.1 Free space Green function

The free space Green function assumes a point force in a fluid causing a disturbance, which decays at infinity. No boundary conditions are taken into consideration and the Cartesian coordinate system is based at the center of the particle (see Figure 3.4). The singularity solution for this point force can be extracted from the classical solution of Stokes (1851) for flow past a sphere (i.e. the velocity and pressure fields)

$$p(r) = \frac{1}{4\pi r^3} r_i \bullet F_i, \quad (3.41)$$

where  $r_i$  is the position vector to the sample point  $SP$  with origin at the particle center,  $r$  is the magnitude of  $r_i$ ,  $x_i$  is the vector from the plate based coordinate system to the sample point  $SP$ , and  $F_i$  is the force vector acting at the virtual particle center. This force is implied by the disturbance velocity field  $v_i(r)$ , which results from the presence of the particle

$$v_i(r) = \frac{1}{8\pi\nu} \overbrace{\left[ \frac{\delta_{ij}}{r} + \frac{r_i r_j}{r^3} \right]}^{\text{Oseen tensor}} F_j, \quad (3.42)$$

where  $\delta_{ij}$  is the unit tensor. Figure 3.4 illustrates the relations between  $x_p$ ,  $x$ ,  $r$ , the particle, and the plate based coordinate system.

The complimentary tensor for the scalar product with the force vector is called Oseen tensor (Oseen, 1974). The variable  $F_j$  refers to the point force  $F_{\text{Faxen}}$  determined within Section 3.2.2, respectively  $F_x$  for plate based coordinates.

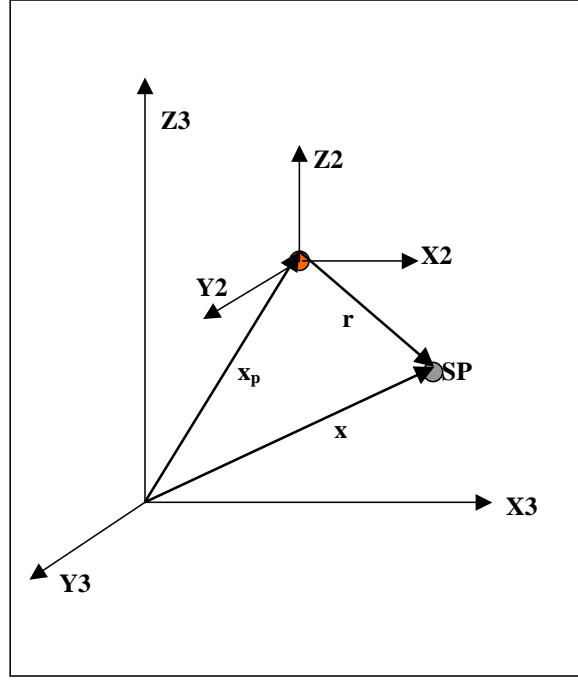


Figure 3.4: Vectorial relations for the free space Green function.

In order to determine the deviatoric part of the stress tensor the gradient of the velocity (equation (3.42)) has to be taken. For this equation (3.42) needs to be differentiated with respect to coordinate direction  $q$  ( $q \in i, j, k$ ) and then expanded with  $F_j$  according to the Einstein convention.

$$\begin{aligned}
 v_{i,q} &= \frac{1}{8\pi\eta} \left( \frac{F_j \delta_{ij}}{r} + \frac{F_j r_i r_j}{r^3} \right)_{,q} & (3.43) \\
 &= \frac{F_j}{8\pi\eta} \left( -\frac{\delta_{ij} r_q}{r^3} + \frac{\delta_{iq} r_j}{r^3} + \frac{r_i \delta_{jq}}{r^3} - \frac{3r_i r_j r_q}{r^5} \right) \\
 &= \frac{1}{8\pi\eta} \left( -\frac{F_i r_q \delta_{iq} (r_1 F_1 + r_2 F_2 + r_3 F_3)}{r^3} - \frac{3r_i r_q (r_1 F_1 + r_2 F_2 + r_3 F_3)}{r^5} + \frac{r_i F_q}{r^3} \right)
 \end{aligned}$$

Due to the position of the pressure sensor, i.e. fixed to the bottom plate, only normal stresses on the plate can be measured, hence, of the deviatoric stress only the  $\tau_{zz}$ , i.e. only the  $\tau_{33}$ -component, is of importance. Also, as determined before, the force is only relevant in the  $r$  (respectively  $x$ ) direction of the coordinate system and is 0 elsewhere. Hence, cancelling all terms containing  $F_2$  and  $F_3$ , and noting that

$F = F_{\text{Faxen}} = F_x = F_1$  and  $i = q = 3$  leads to

$$v_{zz} = v_{33} = \frac{1}{8\pi\eta} \left[ \frac{r_1 F_1}{r^3} + \frac{3r_3^2 r_1 F_1}{r^5} \right] \quad (3.44)$$

for the velocity gradient in the free space flow field in the  $zz$ -direction. Multiplication with  $2\eta$  gives the deviatoric stress  $\tau_{33}$ .

$$\tau_{zz} = \tau_{33} = \frac{1}{4\pi} \left[ \frac{r_1 F_1}{r^3} + \frac{3r_3^2 r_1 F_1}{r^5} \right] \quad (3.45)$$

Here  $r$  is given in particle based coordinates. It can be transformed into the plate based (Cartesian) coordinate system according to  $\underline{r} = \underline{x} - \underline{x}_p$ , i.e.  $r = (x - x_p, y - y_p, z - z_p)$  leading to

$$\tau_{zz} = \frac{1}{4\pi} \left[ \frac{F_1 (x - x_p)}{((x - x_p)^2 + (y - y_p)^2 + (z - z_p)^2)^{\frac{3}{2}}} + \frac{3F_1 (x - x_p)(z - z_p)^2}{((x - x_p)^2 + (y - y_p)^2 + (z - z_p)^2)^{\frac{5}{2}}} \right]. \quad (3.46)$$

When using component notation for the equation for the pressure  $p$  (see equation (3.41)) and applying the same rules as mentioned above for the force, this results in

$$p = \frac{F_1(x - x_p)}{4\pi((x - x_p)^2 + (y - y_p)^2 + (z - z_p)^2)^{\frac{3}{2}}} \quad (3.47)$$

for the free space pressure field.

### 3.2.3.2 Bounded Green function

In this Section a point force in the presence of a stationary plane boundary, as discussed by Blake (1972), is of interest. The bounded problem is discussed in analogy to the free space discussion in the previous Section. The bounded Green function assumes an imaginary particle  $R$  in order to take care of the boundary which is in the midplane between the two particles. The sample point  $SP$  lies on or above (see Figure 3.5) this boundary.

The exact solution for a force singularity in the presence of a stationary plane

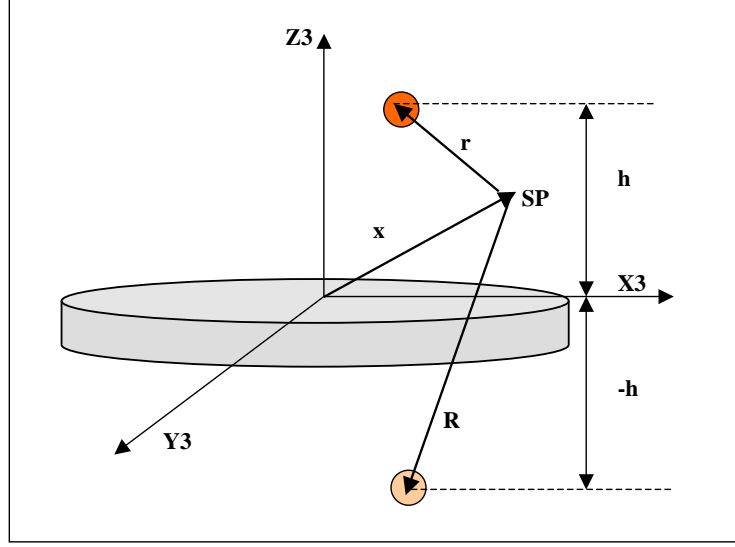


Figure 3.5: Illustration of the vector  $x$  leading to the sample point,  $r$  leading to the real, and  $R$  to the imaginary particle.

boundary is as follows for the pressure

$$p = \frac{R_j}{4\pi} \left[ \frac{r_j}{r^3} - \frac{R_j}{R^3} - 2h (\delta_{j\alpha} \delta_{\alpha k} - \delta_{j3} \delta_{3k}) \frac{\partial}{\partial R_k} \left( \frac{R_3}{R^3} \right) \right] \quad (3.48)$$

and for the velocity

$$v_i = \frac{F_j}{8\pi\eta} \left( \overbrace{\left( \frac{\delta_{ij}}{r} + \frac{r_i r_j}{r^3} \right)}^{\text{real particle}} - \overbrace{\left( \frac{\delta_{ij}}{R} + \frac{R_i R_j}{R^3} \right)}^{\text{image particle}} \right) \quad (3.49)$$

$$+ \frac{2hF_j}{8\pi\eta} (\delta_{j\alpha} \delta_{\alpha k} - \delta_{j3} \delta_{3k}) \overbrace{\frac{\partial}{\partial R_k} \left\{ \frac{h R_i}{R^3} - \left( \frac{\delta_{ij}}{R} + \frac{R_i R_3}{R^3} \right) \right\}}^A,$$

where  $r_i$  refers to the particle position,  $R_i$  to the position of an image particle,  $\alpha = 1, 2$ ; the tensor  $(\delta_{j\alpha} \delta_{\alpha k} - \delta_{j3} \delta_{3k})$  is non zero only when  $j = k$ ; its value is +1 for  $j = 1$  or  $2$ , and 0 for  $i, j = 3$ .  $h$  refers to the distance of the real particle from the plate in the  $z$ -direction, this is  $-h$  for the image particle.

As a first step the term  $A$  of equation (3.49) needs to be differentiated with respect to  $R_k$  before the whole equation is differentiated with respect to  $q$

$$\frac{\partial}{\partial R_k} \left( \frac{h R_i}{R^3} - \left( \frac{\delta_{ij}}{R} + \frac{R_i R_3}{R^3} \right) \right) = \quad (3.50)$$

$$\frac{hR_{i,k}}{R^3} - \frac{3hR_iR_{\alpha,k}R_\alpha}{R^5} - \frac{\delta_{ij}R_\alpha R_{\alpha,k}}{R^3} + \frac{R_{i,k}R_3 + R_iR_{3,k}}{R^3} - \frac{3R_iR_3R_{\alpha,k}R_\alpha}{R^5}.$$

Now it is possible to take the differential of  $v_i$  with respect to  $q$ . The differential of the real particle part is equal to the velocity derivative of the free space Green function but with  $R$  instead of  $r$  for the imaginary particle

$$\begin{aligned} v_{i,q} = & \frac{1}{8\pi\eta} \left[ -\frac{F_i r_q}{r^3} + \frac{\delta_{iq} r_1 F_1 + r_2 F_2 + r_3 F_3}{r^3} - \frac{3r_i r_q r_1 F_1 r_2 F_2 + r_3 F_3}{r^5} + \frac{r_i F_q}{r^3} \right] \\ & - \frac{1}{8\pi\eta} \left[ -\frac{F_i R_q}{R^3} + \frac{\delta_{iq} R_1 F_1 + R_2 F_2 + R_3 F_3}{R^3} - \frac{3R_i R_q R_1 F_1 R_2 F_2 + R_3 F_3}{R^5} + \frac{R_i F_q}{R^3} \right] \\ & + \frac{6h^2}{8\pi\eta} \left[ -\frac{R_q F_i}{R^5} + \frac{R_q F_3 \delta_{i3}}{R^5} + \frac{R_3 F_3}{R^5} - \frac{R_i F_q}{R^5} + \frac{R_i \delta_{3q} F_3}{R^5} \right] \\ & + \frac{6h}{8\pi\eta} \left[ -\frac{5R_i R_q R_1 F_1 + R_2 F_2 + R_3 F_3}{R^7} - \frac{h\delta_{iq} R_1 F_1 + R_2 F_2 + R_3 F_3}{R^5} \right] \\ & + \frac{2h}{8\pi\eta} \left[ \frac{15hR_i R_q R_3 F_3}{R^7} + \frac{\delta_{i3} F_q}{R^3} - \frac{\delta_{q3} \delta_{i3} F_3}{R^3} + \frac{F_i \delta_{3q}}{R^3} - \frac{F_3 \delta_{i3} \delta_{3q}}{R^3} + \frac{F_3 \delta_{iq}}{R^3} - \frac{F_3 \delta_{33} \delta_{iq}}{R^5} \right] \\ & + \frac{6h}{8\pi\eta} \left[ -\frac{3\delta_{i3} R_q R_1 F_1 + R_2 F_2 + R_3 F_3}{R^5} + \frac{R_3 R_q \delta_{i3} F_3}{R^5} - \frac{R_i R_3 R_q}{R^5} - \frac{r_i R_3 F_q}{R^5} \right] \\ & + \frac{6h}{8\pi\eta} \left[ \frac{\delta_{i3} R_3 R_q F_3}{R^5} - \frac{F_3 R_q R_i}{R^5} - \frac{\delta_{iq} R_3 R_1 F_1 + R_2 F_2 + R_3 F_3}{R^5} + \frac{\delta_{iq} R_3^2 F_3}{R^5} \right] \\ & + \frac{6h}{8\pi\eta} \left[ \frac{F_3 \delta_{33} R_q R_i}{R^5} - \frac{R_i \delta_{3q} R_1 F_1 + R_2 F_2 + R_3 F_3}{R^5} + \frac{R_i \delta_{3q} R_3 F_3}{R^5} + \frac{R_i R_3 \delta_{q3} F_3}{R^5} \right]. \end{aligned} \quad (3.51)$$

The reasoning mentioned in the previous Section for only taking  $v_{zz} = v_{33}$  for  $i = q = 3$  is also valid here and leads to

$$\begin{aligned} v_{33} = & \frac{1}{8\pi\eta} \left[ \frac{r_1 F_1}{r^3} - \frac{R_1 F_1}{R_3} - \frac{3r_3^2 r_1 F_1}{r^5} + \frac{3R_3^2 R_1 F_1}{R^5} \right] \\ & - \frac{6h}{8\pi\eta} \left[ \frac{hR_1 F_1}{R^5} + \frac{5R_3^2 R_1 F_1}{R^7} + \frac{R_3 F_1 R_1}{R^5} + \frac{3R_3 F_1 R_1}{R^5} \right]. \end{aligned} \quad (3.52)$$

Multiplying this equation with  $2\eta$  and replacing  $h$  by  $r_3$  results in  $\tau_{33} = \tau_{zz}$

$$\begin{aligned} \tau_{zz} = & \frac{1}{4\pi} \left[ \frac{r_1 F_1}{r^3} - \frac{R_1 F_1}{R^3} - \frac{3r_3^2 r_1 F_1}{r^5} + \frac{3R_3^2 R_1 F_1}{R^5} \right] \\ & - \frac{6r_3}{8\pi\eta} \left[ \frac{r_3 R_1 F_1}{R^5} + \frac{5R_3^2 R_1 F_1}{R^7} + \frac{R_3 F_1 R_1}{R^5} + \frac{3R_3 F_1 R_1}{R^5} \right]. \end{aligned} \quad (3.53)$$

Before being able to add the above determined stress to the pressure from the bounded Green function given in equation (3.48), the differential term of the pressure equation has to be considered. This leads to

$$p = \frac{F_j}{4\pi} \left[ \frac{r_j}{r^3} - \frac{R_j}{R^3} - 2h (\delta_{j\alpha} \delta_{\alpha k} - \delta_{j3} \delta_{3k}) \left( \frac{\delta_{3k}}{R^3} - \frac{3R_k R_3}{R^5} \right) \right]. \quad (3.54)$$

When expanding this equation for the pressure with  $F_j$ , then summing over the indices, and considering that  $F$  only acts in the  $x$ -direction, i.e.  $F_1$ , the following equation can be obtained for  $p$

$$p = \frac{F_1 r_1}{4\pi(r_1^2 + r_2^2 + r_3^2)^{\frac{3}{2}}} - \frac{6 F_1 r_3 r_1 R_3}{4\pi(R_1^2 + R_2^2 + R_3^2)^{\frac{5}{2}}} - \frac{F_1 R_1}{4\pi(R_1^2 + R_2^2 + R_3^2)^{\frac{3}{2}}}. \quad (3.55)$$

### 3.2.4 Particular consideration of the two Green functions for a particle above the origin

The objective of this Section is to investigate the changes in the stress distribution due to the presence of a particle in a fluid. The special case discussed here is a particle above the origin. As before the free space situation is discussed first.

#### 3.2.4.1 Free space Green function

“Above the origin” is with reference to the coordinate system based at the bottom plate. The coordinates of the free space Green function are based in the particle center (see Figure 3.2). Hence, a particle, which is above the origin, is at  $(x, y, z)$  in particle based coordinates but at  $(0, 0, b)$  in plate based coordinates such that  $Z_3 = Z_2 + b$  when  $Z_2$  refers to the particle coordinate system and  $Z_3$  to the plate based system. This leads to the following pressure distribution

$$p = \frac{F_x x}{4\pi (x^2 + y^2 + (z + b)^2)^{\frac{3}{2}}}. \quad (3.56)$$

Hence, there is a pressure disturbance around the particle, which is positive upstream and negative downstream with respect to the particle moving direction. Since the plate is at  $z = 0$ , the function describing the pressure field on the plate is

$$p = \frac{F_x x}{4\pi (x^2 + y^2 + b^2)^{\frac{3}{2}}}, \quad (3.57)$$

where  $F_x$ , which is  $F_{\text{Faxen}}$ , only acts in the  $x$ -direction as before. Assuming a force  $F_x$  of  $1.8 \cdot 10^{-6}$  N, which is calculated as described in Section 3.2.2 for a particle less than  $10a$  away from the origin (i.e. a particle “close to the origin of the plate”, analogue for the distance from the edge) the pressure field disturbance shown in Figure 3.6 and Figure 3.7 can be obtained. The force used is for a particle of  $100 \mu\text{m}$  radius at  $z = 2 \cdot 10^{-4}$  m (in plate based coordinates) in a gap of  $400 \mu\text{m}$  height (i.e.  $h = 2a$ ). The two graphs show the hydrostatic pressure influence.

The viscous influence for the same parameters can be seen in Figures 3.8 and 3.9. It was determined from equation (3.46) when the same coordinate system transformations (see above) as for the hydrostatic pressure were applied

$$\tau_{zz} = \frac{1}{4\pi} \left[ \frac{F_x x}{(x^2 + y^2 + b^2)^{\frac{3}{2}}} + \frac{3 F_x x b^2}{(x^2 + y^2 + b^2)^{\frac{5}{2}}} \right]. \quad (3.58)$$

The comparison of the graphs shows that the viscous stress leads to a sharper and larger peak (approximately 2 Pa) than the hydrostatic pressure. Still, neither of the stresses is larger than the 10 kPa threshold for in-mouth sensation (or the instrumental threshold, according to Tekscan 0.5 kPa). Therefore, the bounded Green function needed to be investigated.

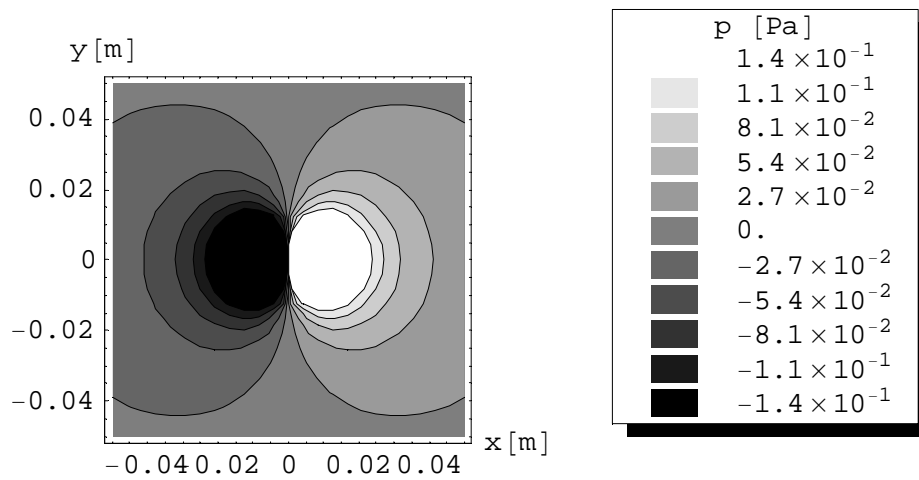


Figure 3.6: Pressure disturbance (hydrostatic pressure  $p$ ) in a fluid due to a single particle under free space conditions, the disturbance is projected onto the bottom plate ( $R_P = 5$  cm).

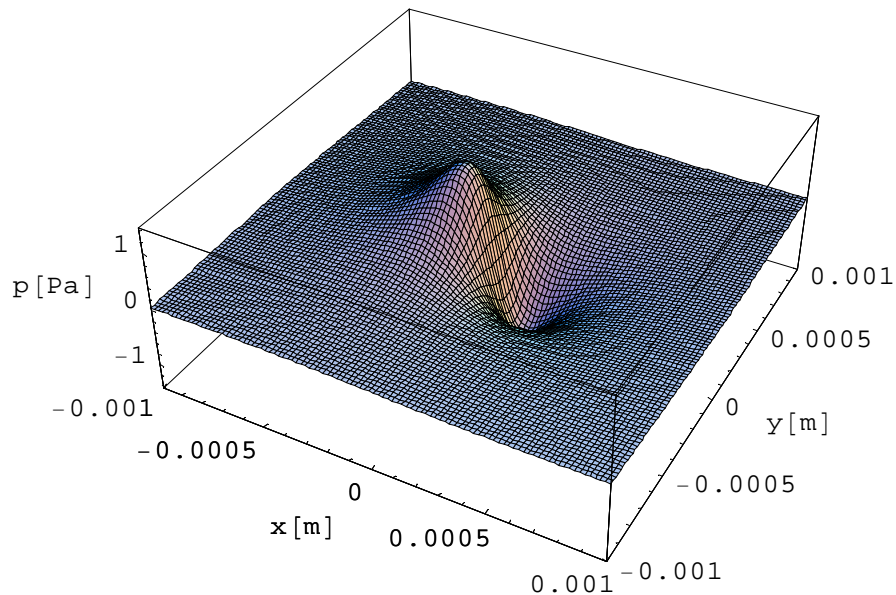


Figure 3.7: Pressure disturbance (hydrostatic pressure  $p$ ) in the fluid due to a point force in free space conditions (regarded in the neighborhood of the particle).

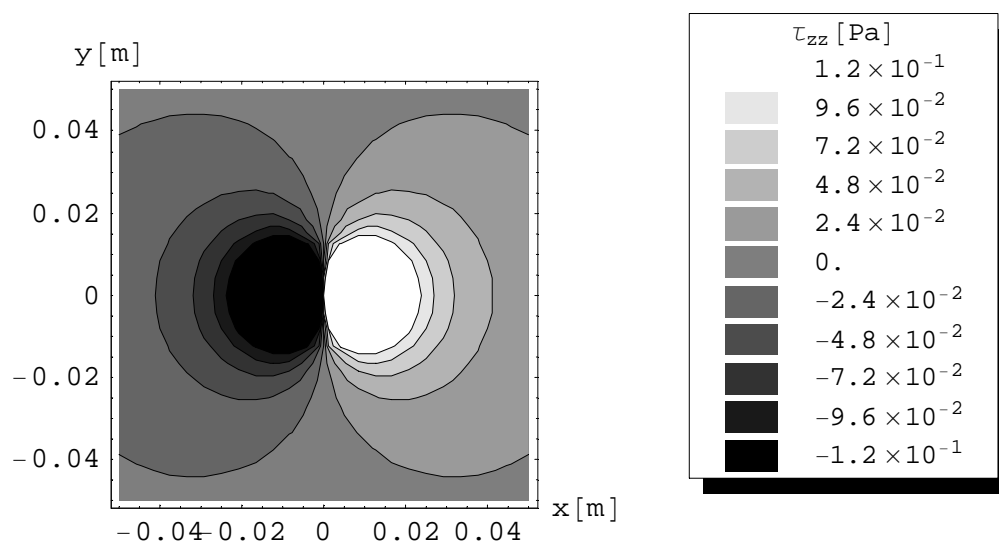


Figure 3.8: Normal stress disturbance (viscous contribution  $\tau_{zz}$ ) under free space conditions, the disturbance is projected onto the bottom plate ( $R_P = 5$  cm).

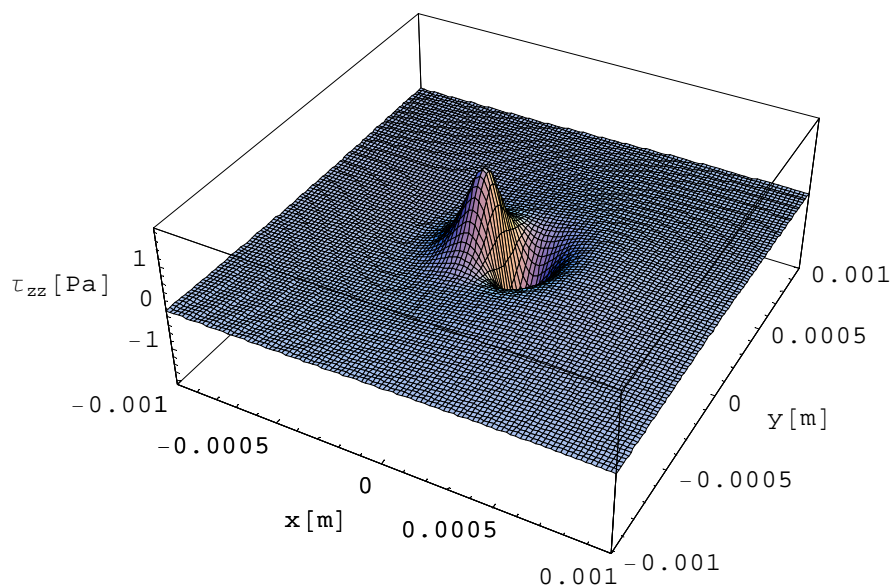


Figure 3.9: Normal stress disturbance (viscous contribution  $\tau_{zz}$ ) in the fluid due to a point force in free space conditions (regarded in the neighborhood of the particle).

### 3.2.4.2 Bounded Green function

As a first step the  $r$ -axis is aligned with the  $x$ -axis so that the force is only in the  $x$ -direction. If the particle is above the origin  $r = (r_1, r_2, r_3) = (-x, -y, b - z)$  and  $R = (R_1, R_2, R_3) = (-x, -y, -b - z)$  in plate based coordinates, where  $b$  refers to the intersection with the  $z$ -axis. Substitution of these relations into equation (3.55) leads to

$$p = \frac{1}{4\pi} \frac{6 F_x (-b - z)(b - z)}{((-x)^2 + (-y)^2 + (-b - z)^2)^5} + \frac{F_x x}{((-x)^2 + (-y)^2 + (-b - z)^2)^3} \quad (3.59)$$

$$- \frac{F_x x}{((-x)^2 + (-y)^2 + (b - z)^2)^3}.$$

This equation gives the pressure anywhere in  $xyz$ -coordinates, which are fixed to the center of the bottom plate. Choosing all parameters to be the same as in the previous Section permits calculation of the pressure on the boundary plane. Figure 3.10 shows the deviatoric part of the particle stress. It was obtained from equation 3.60, when  $r$  and  $R$  were substituted as described above.

$$\tau_{zz} = \frac{1}{4\pi} \left[ \frac{-x F_x}{(((-x)^2 + (-y)^2 + (b - z)^2)^{\frac{3}{2}})} - \frac{-x F_x}{(((-x)^2 + (-y)^2 + (-b - z)^2)^{\frac{3}{2}}} \right] \quad (3.60)$$

$$- \frac{1}{4\pi} \left[ \frac{3(b - z)^2 (-x) F_x}{(((-x)^2 + (-y)^2 + (b - z)^2)^{\frac{5}{2}}} + \frac{3(-b - z)^2 (-x) F_x}{(((-x)^2 + (-y)^2 + (-b - z)^2)^{\frac{5}{2}}} \right] \quad (3.61)$$

$$- \frac{6(b - z)}{4\pi} \left[ \frac{(b - z) (-x) F_x}{(((-x)^2 + (-y)^2 + (-b - z)^2)^{\frac{5}{2}}} + \frac{5(-b - z)^2 (-x) F_x}{(((-x)^2 + (-y)^2 + (-b - z)^2)^{\frac{7}{2}}} \right]$$

$$+ \frac{6(b - z)}{4\pi} \left[ \frac{4(-b - z) F_x (-x)}{(((-x)^2 + (-y)^2 + (-b - z)^2)^{\frac{5}{2}}} \right].$$

The disturbance is in the range of 100 kPa and therefore, overcomes the in-mouth threshold as well as the threshold of the Tekscan sensor. The hydrostatic pressure is not shown since the influence is much less as can be seen in Figure 3.11. The viscous stress is several orders of magnitude larger than the hydrostatic component.

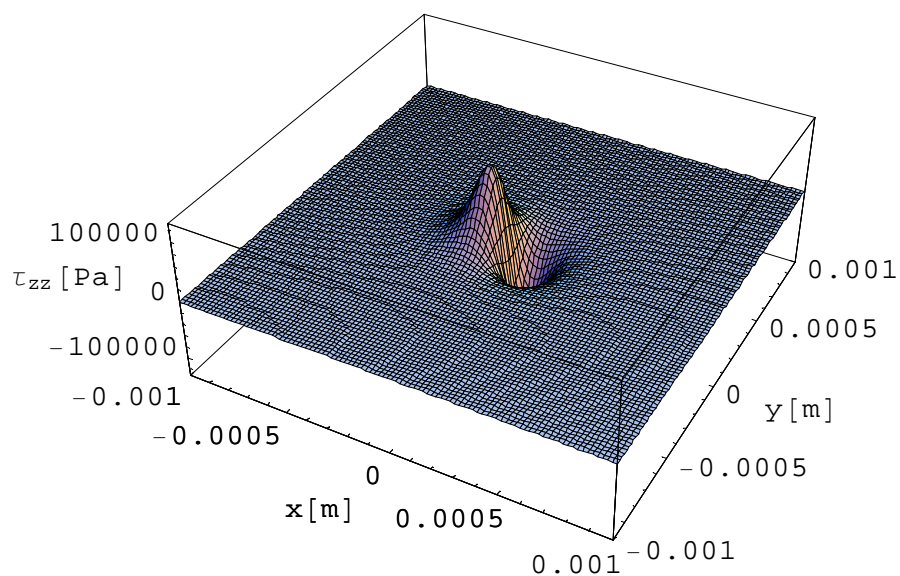


Figure 3.10: Normal stress disturbance (viscous contribution  $\tau_{zz}$ ) in the fluid due to a point force under bounded conditions (regarded in the neighborhood of the particle).

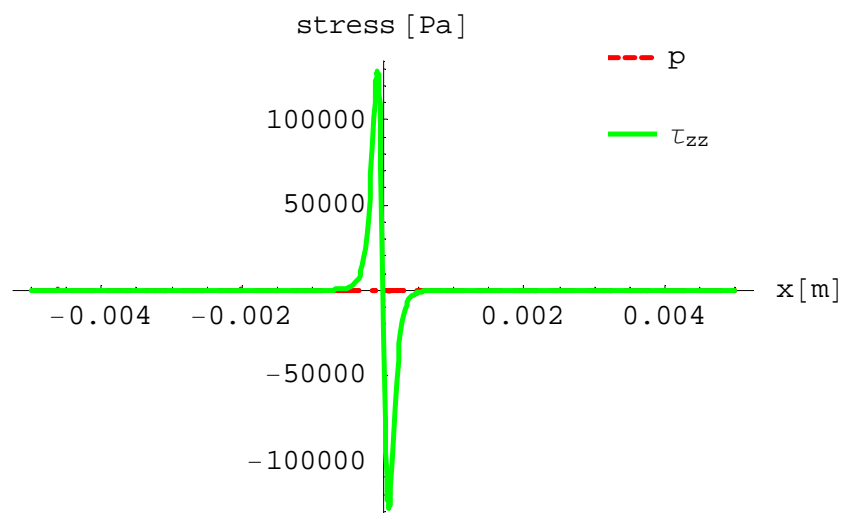


Figure 3.11: Deviatoric (red/dashed) versus hydrostatic pressure for a particle above the origin under bounded conditions (regarded in the neighborhood of the particle).

### 3.2.5 Superposition of the estimated stresses

In order to know the true stress on the bottom plate and therefore the pressure sensor used in Chapter 4, the pure fluid pressure  $P(r)$  obtained from Stefan's equation (see Section 3.2.1) needs to be added to the total stress tensor  $\sigma_{zz}$  obtained from the point-force disturbance. The viscous stress  $\tau_{zz}^{\text{St}}$  from Stefan's equation can be neglected as previously explained. The total stress tensor comes from the particle and consists of the pressure part  $p$  and the deviatoric stress tensor in the  $zz$ -direction, which is equal to the velocity gradient multiplied with twice the viscosity. Again these stresses are first summed for the free space condition before the bounded situation is considered.

#### 3.2.5.1 Stress superposition for the free space situation

As demonstrated in the previous Sections, equation (3.47) gives the pressure distribution for the free space Green's function. Due to the sign convention this equation receives a minus sign when added to the other stress terms. The deviatoric stress, equation (3.46), is added to this.

Finally the pressure distribution of the undisturbed flow field from the Stefan equation (Section 3.2.1), where  $r$  has been replaced by  $x$ , needs to be added. Since there is no dependency in the  $z$  direction this transformation can be formulated as

$$P(x) = \frac{3\eta\dot{d}(t)}{4d^3(t)} (x^2 - R_P^2). \quad (3.62)$$

Figure 3.12 illustrates the influence of the two terms of the total stress tensor by plotting the stress variations versus the radius of the disc. The upper part of the Figure shows the disturbance for a particle above the origin (i.e.  $x = 0$ ) whereas the bottom Figure represents a particle close to the edge, i.e.  $x = 0.049$  m (the values used for  $a$ ,  $F_x$ , and  $d$  are identical with the values used in Section 3.2.4.1). It can be seen that the particle disturbs the fluid more (stress is two orders of magnitude higher) when it is closer to the edge. Furthermore, the fact that the fluid pressure decreases versus the edge (parabolic profile) supports this effect. The positive pressure change in front of

the particle and the negative change behind the particle discussed before can clearly be seen. Still, the resulting stress (150 Pa) is not sufficient to overcome the in-mouth threshold. This is more clearly shown in Figure 3.13. Here the absolute disturbances is shown by plotting the pressure resulting from the sum of the three terms (red/dashed) versus the pure fluid pressure (blue/solid). The curves do not significantly deviate. Hence, in the following the bounded Green function has to be looked at, especially since the situation dealt with here (parallel plate squeeze flow) is certainly a bounded problem.

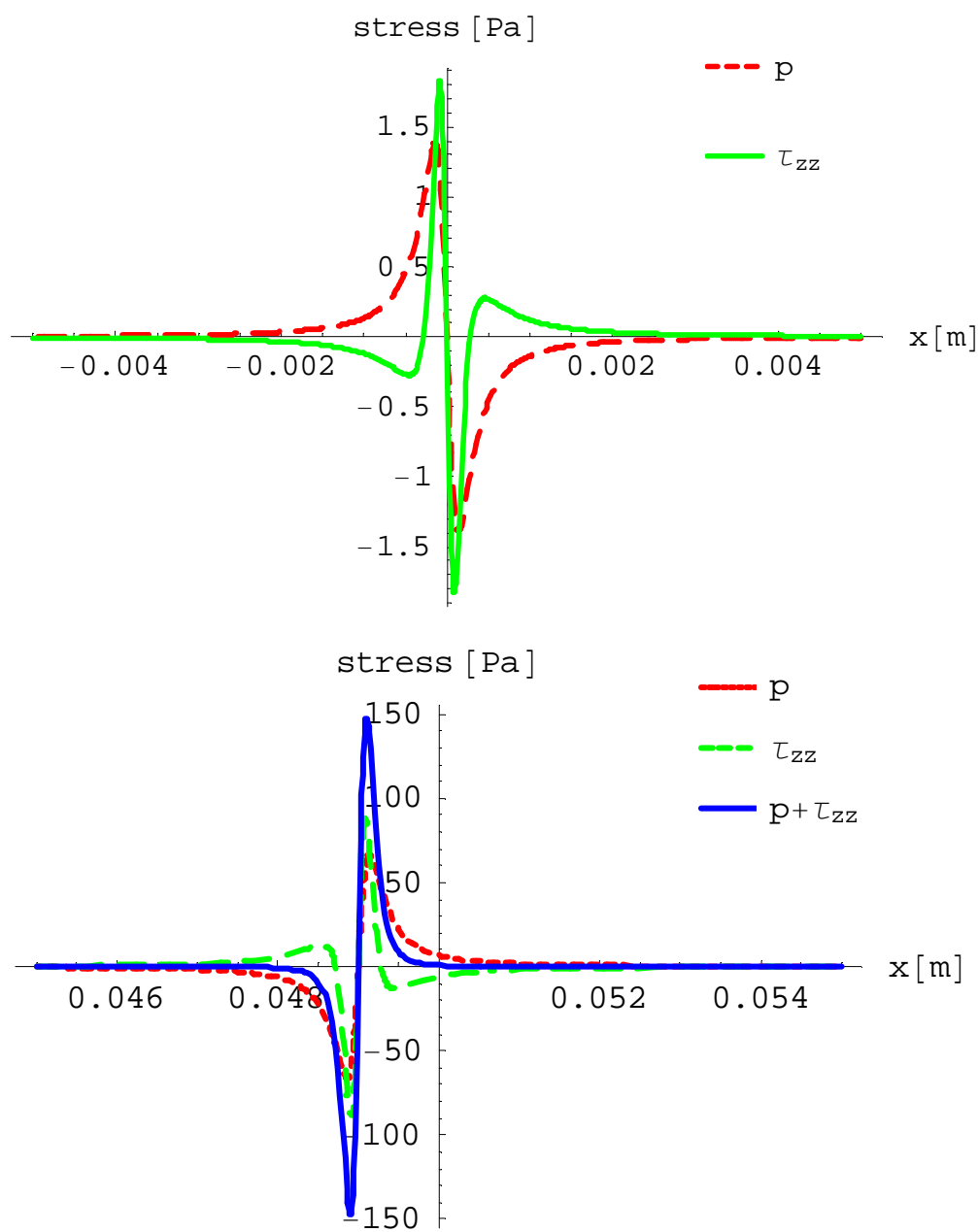


Figure 3.12: Top: Comparison of hydrostatic and deviatoric stress for a particle above the origin. Bottom: Superposition (blue/solid) of hydrostatic pressure  $p$  (red/dashed fine) and deviatoric stress  $\tau_{zz}$  (green/dashed) curves for a particle close to the edge of the plate under free space conditions.

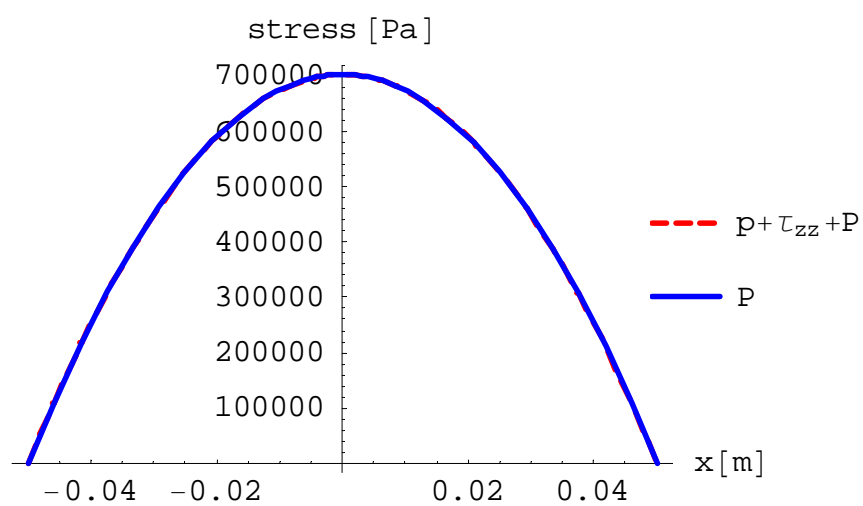


Figure 3.13: Comparison of normal stress resulting from summing over all three terms (red/dashed) in the free space situation versus the pure fluid pressure distribution (blue/solid) taken from the Stefan calculation.

### 3.2.5.2 Stress superposition for the bounded situation

As can be seen in Figure 3.13, the variations between the curves for the fluid with and without particle (for the free space situation) are hardly visible. Still, the Tekscan pressure sensor has to resolve the difference between the curves as a pressure field disturbance and not as noise (analogue for the mechanoreceptors in the mouth). Therefore, in the following the pressure  $p$  taken from equation (3.55), the deviatoric stress  $\tau_{zz}$ , see equation (3.60), and Stefan's pressure, see equation (3.31) need to be superposed for the bounded situation. The normal stress  $\tau_{zz}^{ST}$ , see equation (3.35), is neglected for previously mentioned reasons.

The disturbances of the fluid pressure field due to the particle in the bounded situation are generally larger. This can be seen when comparing the sum of the pressure  $p$  and the deviatoric stress  $\tau_{zz}$  for both conditions as shown in Figure 3.14.

Plotting the same graphs for the bounded situation as before for the free space condition (using the previous parameters) shows that the disturbances resulting in the bounded situation are larger than for the free space situation, see Figures 3.15 and 3.16 respectively 3.17. The differences between the curves are clearly visible ( $6 \cdot 10^6$  Pa) and should be detectable with the Tekscan sensor and with the mechanoreceptors. Investigating a particle close to the edge in a very small gap leads to larger fluctuations (range of 1000s kPa) than the same situation for a particle close to the midpoint (100s kPa, see Figure 3.18). Still, the fluctuations are above the necessary threshold in both cases. Figure 3.15 once again shows the almost negligible influence of  $p$  in comparison with  $\tau_{zz}$ .

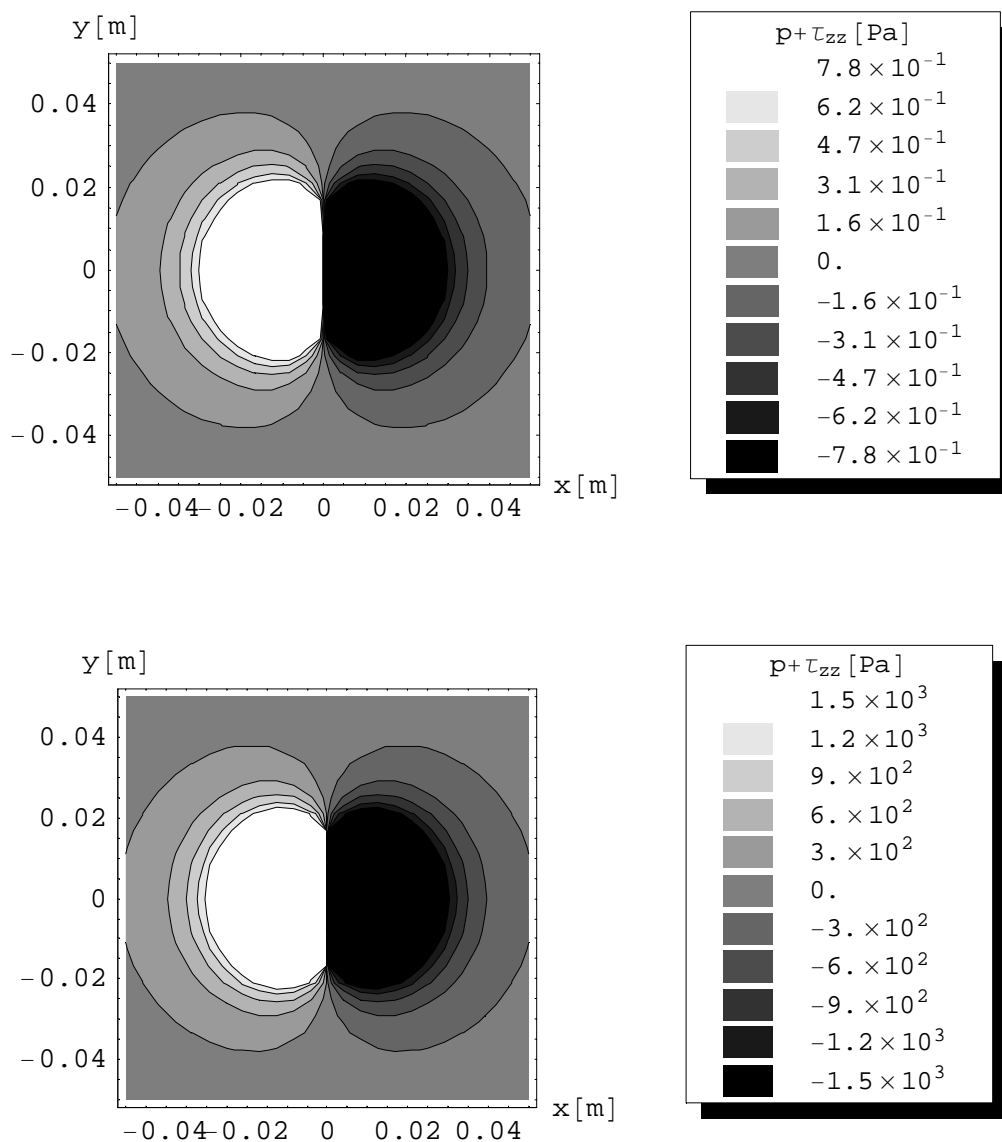


Figure 3.14: Comparison of the normal stress (sum of  $p$  and  $\tau_{zz}$ ) in the  $xy$ -plane for the free space (top) and bounded (bottom) Green's function showing that the stress is larger for the bounded Green's function (investigation for a particle less than 10 radii away from the edge).

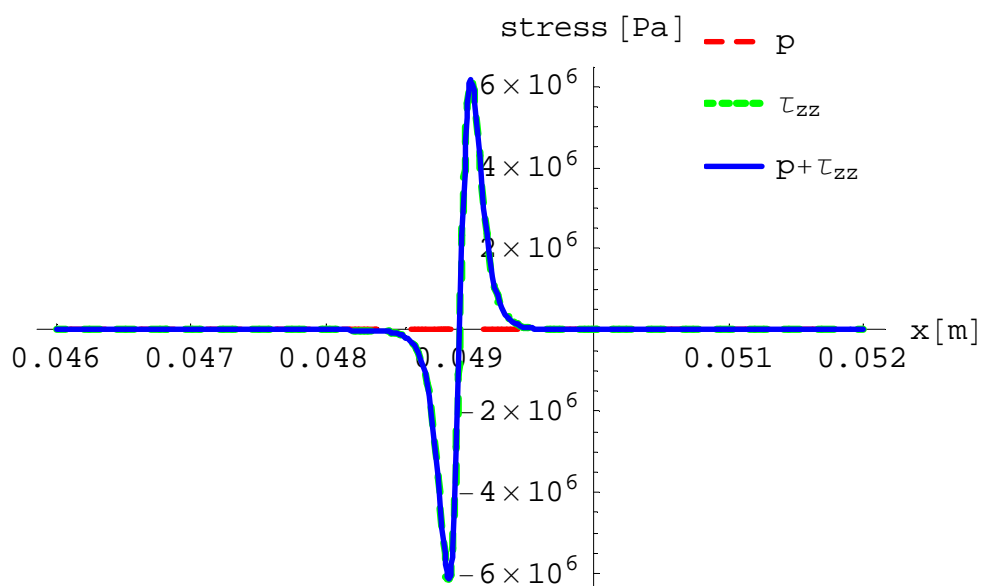


Figure 3.15: Superposition (blue/solid) of pressure  $p$  (red/dashed) and deviatoric stress  $\tau_{zz}$  (green/largely dashed) curves for a particle close to the edge under bounded conditions.

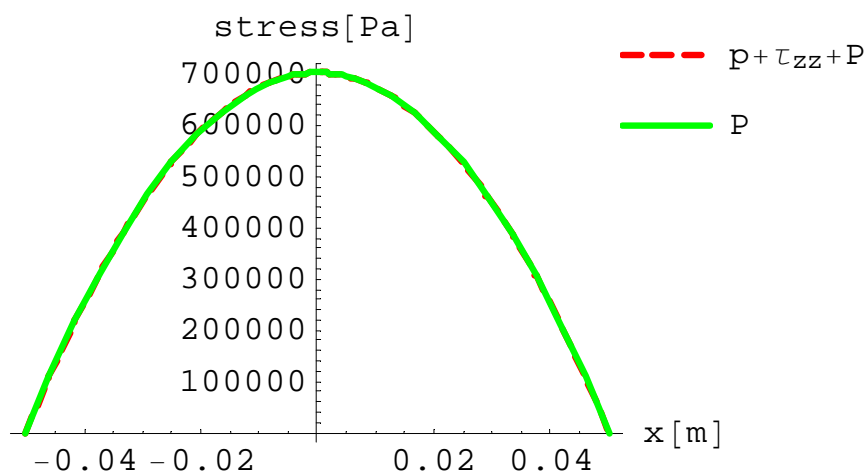


Figure 3.16: Comparison of the stress resulting for the bounded situation from summing over all three terms (red/dashed) versus the pure fluid pressure distribution (green/solid); no disturbance visible (far field perspective).

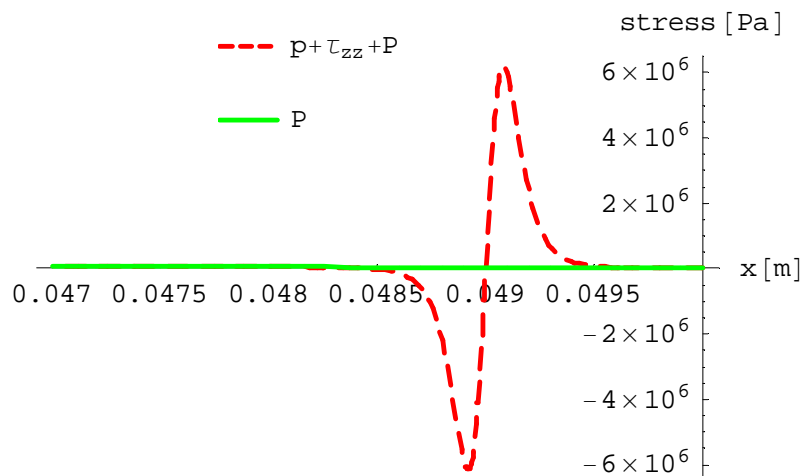


Figure 3.17: Comparison of stress resulting for the bounded situation from summing over all three terms (red/dashed) versus the pure fluid pressure distribution (green/solid) taken from the Stefan calculation. Close up, disturbance visible. Particle close to the edge.

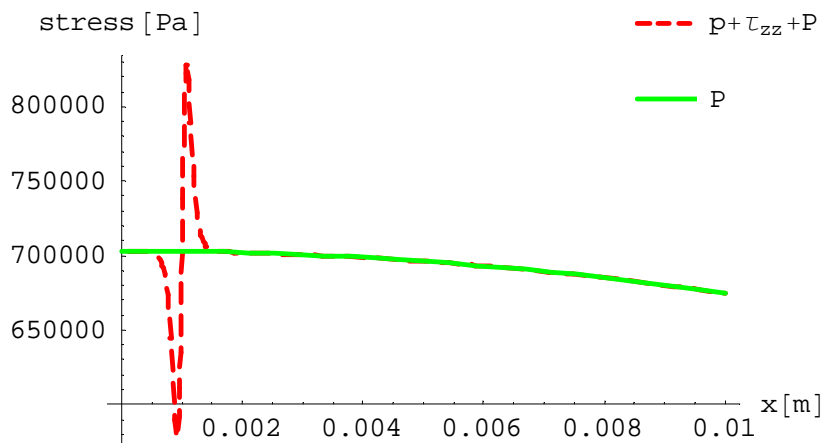


Figure 3.18: Comparison of total pressure resulting for the bounded situation from summing over all three terms (red/dashed) versus the pure fluid pressure distribution (green/solid) taken from the Stefan calculation. Close up, disturbance visible. Particle close to the center.

Three aspects are investigated further: 1. Considering that the particle radius enters Faxen's law with the third power its influence has to be determined. Plotting the resulting pressure fluctuation versus the radius of the particle shows the dependance. For this, additionally to the previous parameters (particle size, plate velocity, viscosity, half plate distance), the sample point is set at (0.03 m, 0.00 m, 0.00 m) and the particle at (0.029 m, 0.00 m, a 1.1). The plates have a radius of 0.05 m as previously. The resulting stress fluctuations are shown in Figure 3.19. This clearly demonstrates that a small particle leads to a higher disturbance due to the smaller gap between the plates.

2. Figure 3.20 shows that the resulting stress is also highly dependent on the particle's position. The parameters are identical to the previous investigation, except for particle position, which is now at  $(x - 0.0015, 0, a 1.1)$ , i.e. 1.5 mm away from the sample point, whereas  $x$  is varied in this part. From the graph it can be seen that the particles should preferably not be placed close to the center but rather in the outer regions of the sensor since their influence increases.

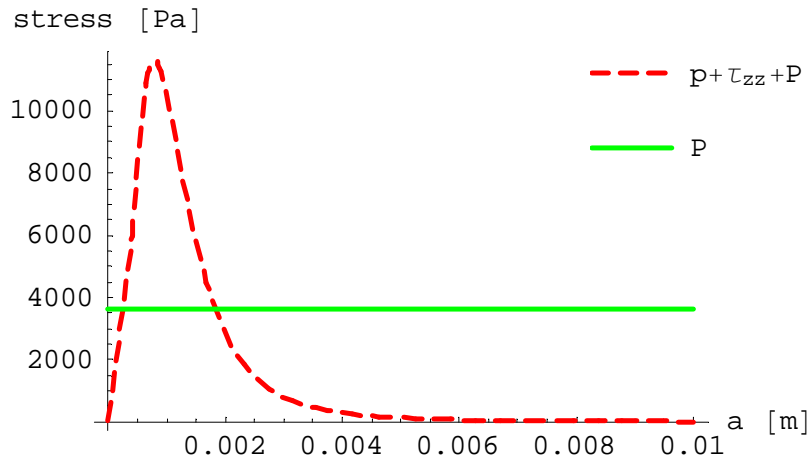


Figure 3.19: Resulting pressures in Pa in dependence of the particle radius  $a$ . This shows that a particle with radius 0.001 m should give a visible disturbance of 10 kPa if the sensor is not too noisy itself (red=particle pressure, green=fluid pressure).

3. The resulting pressure (force) is also dependent on the particle position  $z$  in the gap (how close the particle is to the plate) and the absolute gap around the particle ( $h$ ). Figure 3.21 illustrates the influence of the percentage of the gap the particle occupies

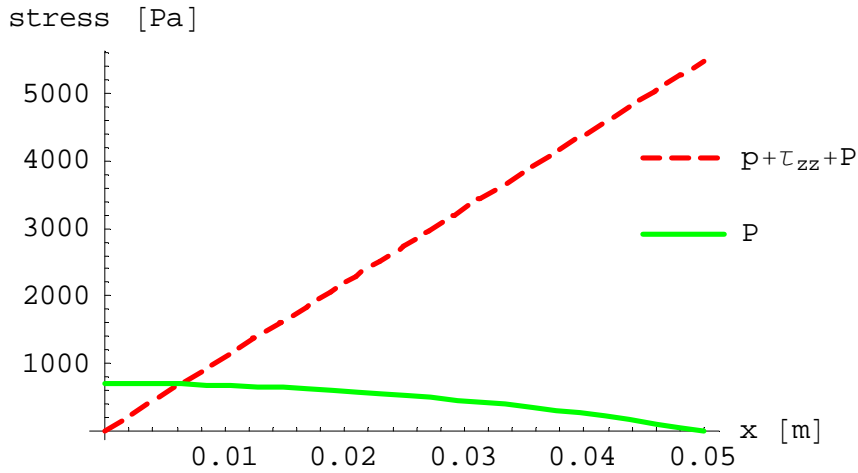


Figure 3.20: Dependence of the disturbance caused by the particle on the particle position. This clearly shows that particles closer to the edge cause more disturbance, especially since the pure fluid pressure (Stefan) is decaying towards the edge (red=particle, green=fluid pressure).

for three different situations (10 %, 50 %, and 99 %). The resulting force relations of Faxen and Stokes (multiplied with the dimensionless radius  $r^*$ ) are plotted against the relative particle position  $\frac{z}{h}$ . This relation is obtained in the following way: in order to have an indication of the velocity in front of the particle and behind the particle, the gradient of the Stefan velocity (equation 3.33) is taken and multiplied with the scale of the rigid body, i.e. the particle radius  $a$ . When Faxen's force is divided by Stokes' force including this term for the velocity, this leads to

$$\frac{F_{\text{Faxen}}}{F_{\text{Stokes}}} = \frac{r a}{3(-h^2 + z^2)}. \quad (3.63)$$

When scaling  $h$  and  $a$  with  $h$ , and  $r$  with  $a$ , leading to the dimensionless  $r^*$ , all variables are dimensionless. Their relations can be investigated. Each obtained value for the relation of the Faxen and Stokes force needs to be multiplied with the dimensionless radius. It can be seen that in the case of increasing  $\frac{z}{h}$  (when regarding the lower plate this means the more the particle approaches the plate) the relation Faxen/Stokes increases, giving more importance to the Faxen force. Figure 3.21 also illustrates very well that the more space the particle takes up of the gap, the larger the force is, i.e.

the curve for 99 % (blue/solid) is much larger than the corresponding curve for 10 % (red/largely dashed). Analogue the smaller the gap around the particle is, the larger the influence of the Faxen force is. These aspects have to be kept in mind for the further discussion. Furthermore, the larger  $r^*$  (which is the radial distance in particle radii) becomes, the more influence the Faxen force has. For very small  $r^*$  the Stokes force is larger than the Faxen force but close to the midpoint, e.g. at distance  $a$ , the theory is not valid because the condition  $\frac{h}{r} \ll 1$  is not fulfilled.

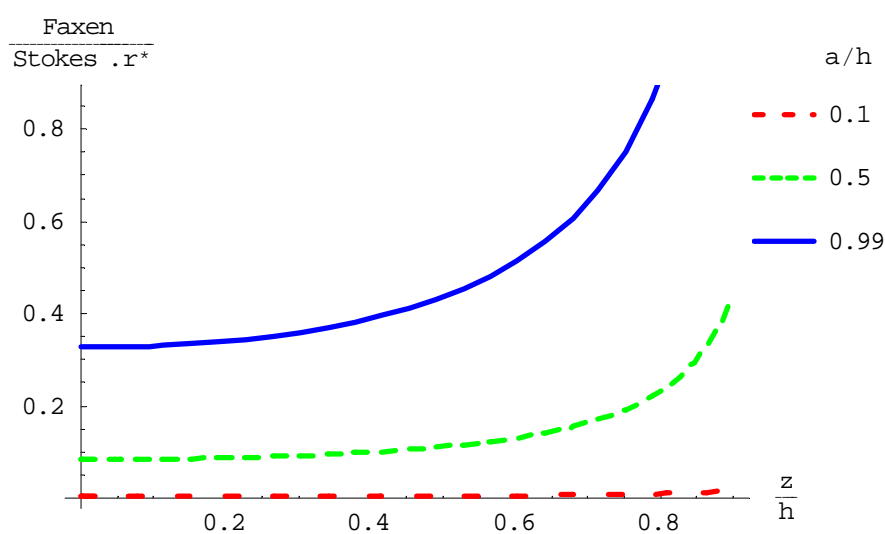


Figure 3.21: Relation of Faxen's force to Stokes' force for different ratios of particle size and half plate distance ( $a/h$ ) as a function of particle position in the gap ( $z/h$ ).

# Chapter 4

## Experimental validation of the fluid mechanical model

### 4.1 Introduction to the experiments

In order to verify the mathematical theory stated in the previous Chapter experimentally two sets of squeeze flow trials were carried out. The aim of the experiments was to show that a particle containing fluid has a characteristic stress field, meaning that different pressures are shown in areas with a particle than in the ones without a particle. From the mathematical model it can be obtained that ideally there should be a positive pressure in front (with respect to the moving direction of the fluid) of the particle and a negative pressure behind the particle.

In a first step the sensitivity of the pressure sensor, which was supposed to show the fluctuations, had to be determined. This was done by carrying out a pure squeeze flow trial and comparing the experimental data with the theoretical results of the Stefan equation (see Section 3.2.1). Pure squeeze flow provokes a parabolic pressure profile when plotted in dependence of the radius as previously demonstrated. This has been verified by other authors (Yates et al., 2001).

In a second step the stress field perturbations were investigated by adding a particle to the fluid. The size of the particle was chosen so that the disturbances caused by it are larger than the previously determined noise threshold of the sensor. Setting the threshold of the sensor equal to the complete stress for the bounded Green function ( $p + \tau_{zz}$ ) and solving for  $a$  gives the necessary particle radius  $a$ . All other parameters such as the plate velocity, fluid viscosity, particle position, plate distance, and sample point were known. This determination was done at the end of the previous Chapter, where the particle caused pressure disturbances  $p$  were plotted in dependence of the particle radius.

The idea was to draw conclusions from the experimental data about the stress field perturbations in-mouth and therefore grittiness perception. For the scaling from the instrumental to the in-mouth conditions see Section 4.3.1 (dimensional analysis).

## 4.2 Materials & methods

### 4.2.1 Experimental set-up

For the experimental set-up two parallel steel plates (PSP, see also Roussel & Lanos (2003) and Leider & Bird (1974)) of 5 cm radius were mounted to a Zwick Roells texture analyzer (model Z005). A Tekscan pressure sensor (model 5051, for further details concerning the sensor see below), was fixed to the middle of the bottom plate.

At the beginning two flat, plain parallel plates were mounted. The bottom plate was modified as described below. During the equilibration and calibration described below, it turned out that the contacting surfaces play a very important role, meaning that two steel plates contacting each other do not load enough sensels, and the ones, which are loaded, are not equally loaded. In order to have a compliant surface, a mouse-pad (neoprene) was attached onto the upper plate and covered with cling film for protection. In order to assure axissymmetric squeeze flow the fluid needs to cover the whole plate and be kept on the plate at the beginning. Therefore a different bottom

plate was made, which can be seen in Figure 4.1. This plate has a milled-out center piece but also a circular flute in which a separable ring can be placed. The ring disposes of a small slot, where the sensor can be slid in. In order to keep the sensor stable on the plate, wax was placed into the flute underneath the sensor to keep it from hanging down at the edge of the plate. The ring has a horizontal line at the height of 5 mm indicating the fill height.



Figure 4.1: Experimental set-up showing the soft coverage of the upper plate, split rings, wax, and the milled out center piece.

#### 4.2.2 Tekscan pressure sensor

Three different measuring ranges of the pressure sensor, i.e. 0 - 138 kPa (20 psi), 0 - 345 kPa (50 psi), and 0 - 517 kPa (75 psi) were purchased. The smallest sensor was used the most since it disposes of the finest resolution. Later the 345 kPa sensor was used as well since in contrast here the noise level should be less, but this is unfortunately on

the cost of the resolution. At the heart of each sheet sensor there is a squared, 0.1 mm thick measuring area containing 1936 measuring points arranged in form of a matrix. This is within an area of 5.6 cm x 5.6 cm resulting in a sensel spacing of 1.27 mm, see Figures 4.2 and 4.3.

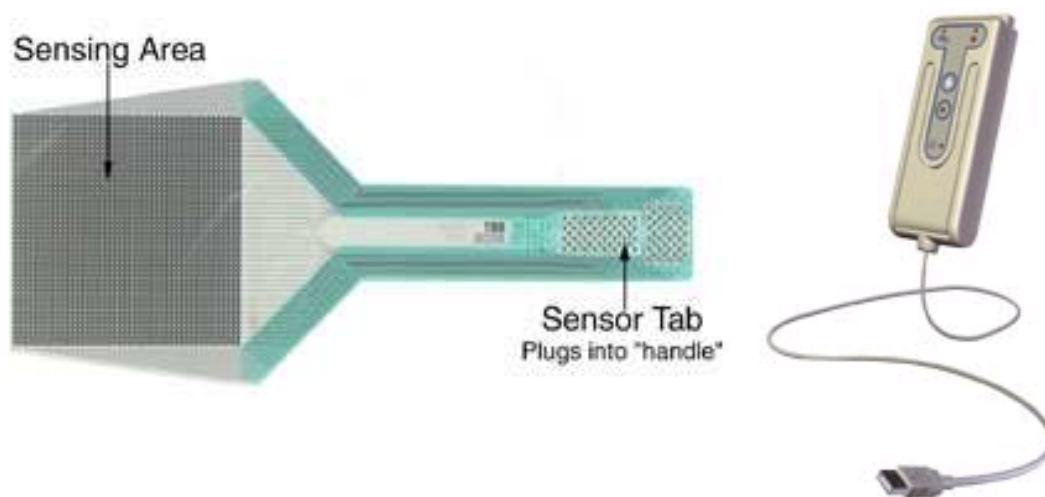


Figure 4.2: Tekscan pressure sensor and USB handle (Tekscan Inc., Boston, MA, USA).

The standard sensor consists of two thin flexible polyester sheets, which have silver electrodes (conductive) in row and column pattern spread across them. When they are put on top of each other, cross points turn into contact points/sensels. Between these two sheets there is also a semi-conductive ink (patented), which registers the changes in resistance at the intersection points, for an illustration of the composition of the sensor see Figure 4.4. These sensors work in real-time as they take up to 125 pictures per second. They can be used in combination with products such as food, and they are capable of recording static as well as dynamic measurements, as necessary within the framework of this project. The 2-D and 3-D displays show the location and magnitude of the forces exerted on the surface of the sensor at each sensing location. Force and pressure changes can be observed, measured, recorded, and analyzed throughout the test. The sensor is placed into a mobile handle, which is connected to a computer via a USB connection. The tools menu allows adjustment of the sensitivity range of the sensor. Eight different sensitivities are provided (here listed in descending order):

high-2 (maximum), high-1, mid-2, mid-1, default, low-3, low-2, low-1 (minimum).

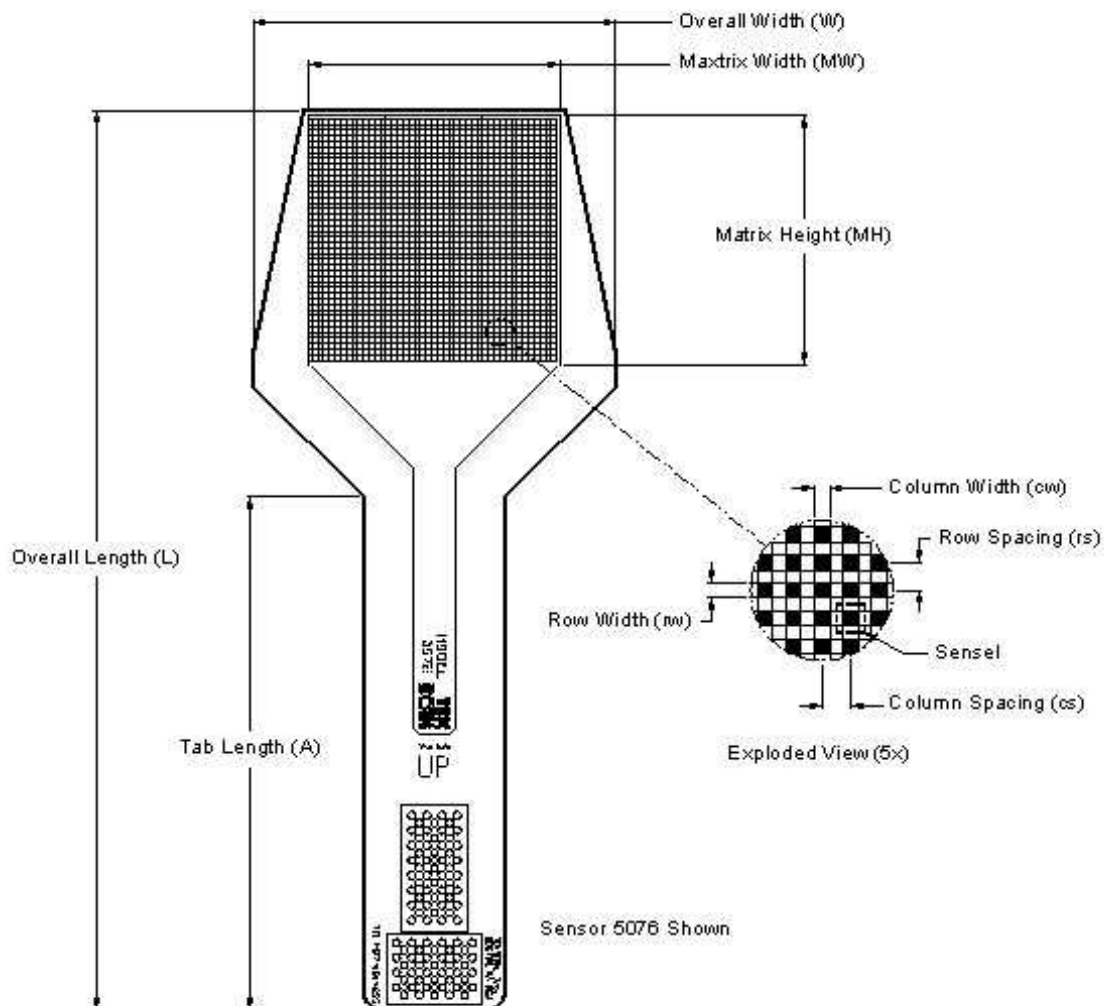


Figure 4.3: Dimensions of the Tekscan sensor (Tekscan Inc., Boston, MA, USA).

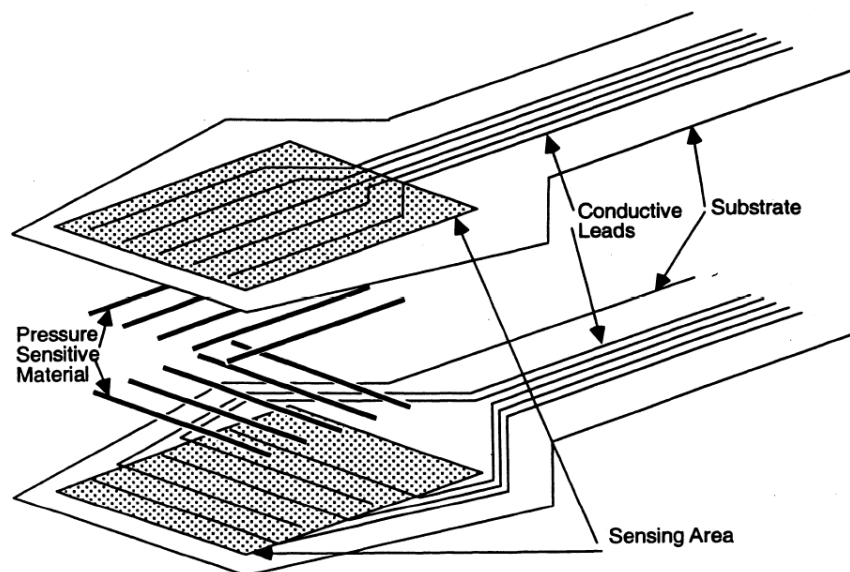


Figure 4.4: Composition of the Tekscan sensor: rows and columns of silver electrodes on polyester sheets with a semi-conductive coating (pressure sensitive ink, patented) between them (Tekscan Inc., Boston, MA, USA).

### 4.2.3 Fluid and particle materials

The fluid used in the majority of the trials (1-10) was a viscosity standard (silicon oil) from Brookfield Engineering Laboratories generally used for the calibration of rheometers. By using a standard it was assured that the viscosity of 30 Pas (measured at 25 °C) shows negligible variations. For this purpose the laboratory temperature is also kept constant and regularly controlled. In trial 11 a highly viscous, 300 Pas, silicon oil, from the Wacker Silicon Grease Series (Wacker AK 300 000) was used.

The particles were 1 mm in radius and made of polypropylene, specific gravity 0.95. In the calculations “equally buoyant” particles were assumed. This is the closest, which could be found to the specific gravity of the silicon oil used (0.94). They were obtained from Dejay Distribution Ltd, Wokingham, Berks, UK.

#### 4.2.4 Technical improvements of the system

The sensor is very thin with its thickness of  $100\ \mu\text{m}$  but still it sticks out from the surface and this caused the first problem. If the sensor is higher than the rest of the plate and non-compliant, all force is loaded on the sensor but not on the plate and the calculations done beforehand in the mathematical Section are not valid as they were done for a much larger and especially circular surface. Therefore, a film of the same thickness as the sensor was glued around the sensor leading to an even surface. The sensor and the leveling film around it were fixed on the plate with a small amount of silicon grease. Later it turned out that due to the stickiness of the test substance (highly viscous silicon oil) this was not very convenient. Hence, the shape of the sensor was milled out of the bottom plate (plate p2 changed to p3) see Figure 4.5 with a height of  $\approx 100\ \mu\text{m}$ , which corresponds to the thickness of the sensor. Milling out the shape of the sensor decreased the risk of an uneven surface, which might easily occur with the leveling film when mounting and removing the ring for sample loading.



Figure 4.5: Bottom plate of the set-up with milled-out center in the shape of the sensor, depth  $100\ \mu\text{m}$ .

## 4.2.5 Calibration & equilibration

### Technical calibration & equilibration

The calibration of the Zwick strain frame is rather simple. Before starting the measurements the force on the load cell has to be zeroed (software: machine/force zero) and the zero distance determined. The procedure for taring the crosshead is in the program menu under machine/verification/Crosshead SN162711. Here the distance to be approached has to be set beforehand. Once chosen the crosshead approaches this distance with a maximum speed of 10 mm/min until the predetermined force change of 2.5 N is registered. This point is then set as zero distance.

In order to use the Tekscan sensor with its maximum sensitivity and measuring range it has to be first *equilibrated*: loaded with an even load and all points have to be initialized so that they measure the same pressure, and afterwards *calibrated*, i.e. loaded with a known load, then the maximum measuring range is given by extrapolation and can be shown on the scale, which up to this point only shows raw data on a scale from 0 to 256. This does not yet correspond to SI units. For an overview of the equilibration and calibration methods described in the following, see Table 4.1

During the equilibration the full sensor has to be loaded. Since the supplier gave the advice to use surfaces similar to the test surfaces, the calibration bladder used later on was not used in the first calibrations but instead the top plate with its known weight was placed in direct contact with the bottom plate and the sensor, and additional weight was added (equilibration 1). Loading the sensor this way did not stimulate all sensels because the surface is not sufficiently compliant. Even the supplier's advice to increase the contract area by placing a piece of tissue between them (equilibration 1a) did not result in any satisfying results, see below. Therefore, afterwards the calibration bladder was used instead, providing a more homogenous load (equilibration 2). For this type of equilibration the sensor was clamped between parallel plates exerting pressure. The bladder used has a maximum pressure range of 35 kPa. Once the sensor had been placed between the plates and the valve was closed, the bladder was loaded with known

Table 4.1: Overview of possible equilibration and calibration methods.

<b>method</b>	<b>number</b>
<b>equilibration</b>	
direct contact with the steel plate	1
tissue between the steel plate and the sensor	1a
bladder	2
Zwick texture analyzer and mouse pad	3
<b>calibration</b>	
direct contact with the steel plate, additional load	1
tissue between the steel plate and the sensor, additional load	1a
squared cubes made from steel and caoutchouc	2
Zwick texture analyzer and mouse pad	3

weights, and the equilibration feature (Tekscan software: tools menu) was started. A waiting period of 30 seconds was set in order to give air bubbles in the sensor matrix the chance to escape. To support this aeration, small slits were cut into the sensor at the edges, where there were no wires. The equilibration file can be saved and loaded into the window. For an example of such a file see Figure 4.6. Here it can be clearly seen that the points are not tared to measure equally, fluctuations can be seen between individual points.

A third equilibration alternative (equilibration 3) was loading the sensor equally with the help of the Zwick strain frame, by placing a soft material such as a mouse-pad on the sensor, well aligning it on the plate and then descending the top plate. This way load can be applied in the desired range. Still this did not take care of the high variations between individual points. This was not a satisfying situation and is explained below.

When the equilibration had been done the calibration could be carried out. Whereas for the equilibration it is necessary to load the full sensor surface this is not necessary

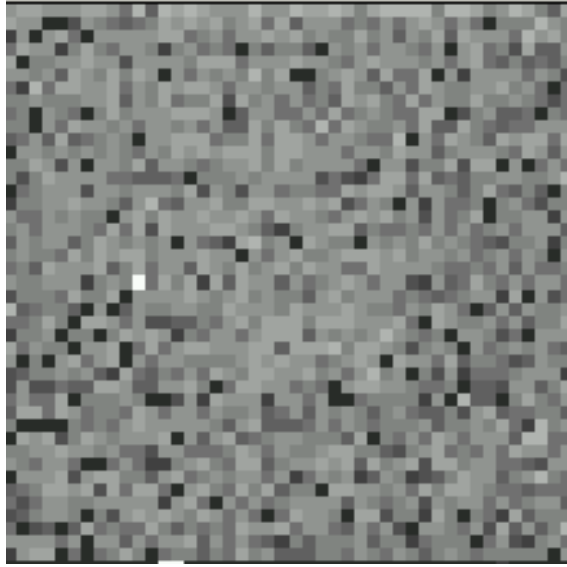


Figure 4.6: Example of an equilibration file.

for the calibration since the measuring range is extrapolated. Instead it is important to know the exact weight of the load. Nevertheless in a first approach (calibration 1, analog equilibration 1) the sensor was loaded over its full surface with the help of the top plate. This way of calibrating never let the sensor extrapolate its maximum range of e.g. 345 kPa (50 psi). This was due to insufficient contact area, same reasoning as previously explained. The sensors are scaled with rather soft surfaces when they are produced. Therefore, one option was to consider the measuring range printed on the sensor only as an order of magnitude but not as an absolute value. The advise given by the supplier was to test the effect of different contact surfaces for the load by placing varying objects onto the sensor such as caoutchouc, steel, and a neoprene patch (mouse pad) and loading them with additional weights (calibration 2). Hence, pieces of 4 cm<sup>2</sup> surface of these three materials were prepared, weighed, and then directly placed on the sensor before they were loaded with a weight of around 5 kg. The exact weight was noted as it needed to be entered into the system. Afterwards the calibration feature was started in the tools menu by adding a new calibration and entering the applied force in kilograms. A 30 second waiting period was also included in this procedure. Afterwards the saturation pressure was extrapolated and the unit scale determined

automatically. This file can also be saved and loaded into the real time window.

For calibration 2, due to the smaller surface of the load object in comparison to the sensor surface, not all sensels were loaded. Since there is a total of 1936 sensels on a surface of 31.36 cm<sup>2</sup> a load on 4 cm<sup>2</sup> of this sensor equals approximately 247 loaded sensels. When loaded again the values shown by the sensor were off. The explanation for this was that some sensels were overloaded during the calibration since the control measurements were always different by the same negative offset of e.g. 20 %. Once a sensel is overloaded only qualitative information is given but not the amount of overload. Hence, the calibration was done again for a lower weight, i.e. 2 kg instead of the previous 5 kg. Here values such as 36 kPa (when extrapolated from 904 loaded sensels) were given, e.g. for a 35 kPa sensor. The neoprene patch was excluded from the procedure since loading was too difficult. As for the equilibration the calibration could also be carried out by fully loading the sensor with the help of the Zwick strain frame (calibration 3). The load applied was accurately shown by the Zwick in this case.

Once acceptable equilibration (loaded with almost maximum weight possible on the bladder or with the help of the Zwick strain frame - both were tried) was obtained and good calibration data, i.e. the value mentioned as the maximum on the sensor had been extrapolated, was found, a measurement was carried out. No smooth data could be obtained. An example of the best equilibration/calibration, which could be obtained, can be seen in Figure 4.7. According to the Stefan equation a contour plot with concentric rings would be expected, where the highest value is close to the midpoint of the plate. This problem was tried to be solved with help of software (see next Section), since technically (manually) it did not seem possible.

### **Calibration & equilibration of the experimental data with the help of a MATLAB code**

During the experimental procedure it remained impossible to synchronize the Tekscan and the Zwick strain frame or to give a triggering signal to either one of the softwares,

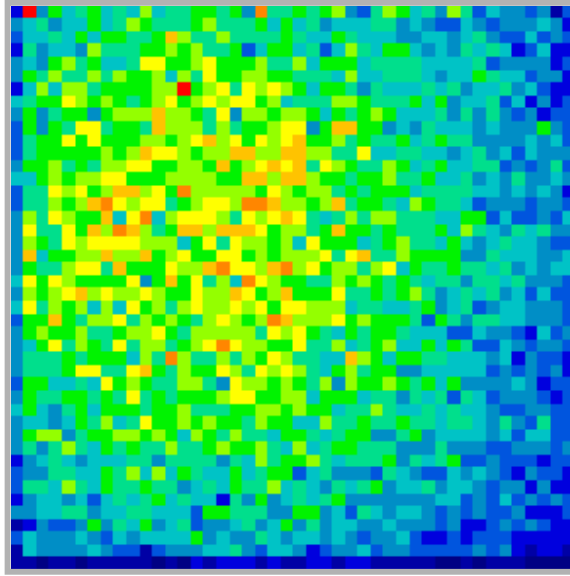


Figure 4.7: Tekscan frame showing the maximum of a measurement with equilibration 2 and calibration 2.

which would be understood by the other machine. Manual synchronization was also too time-consuming. Hence, the data evaluation was more difficult than expected and was carried out with the help of MATLAB. This program deals with vectors and matrices. Thus it seemed appropriate since the data from the Tekscan pressure sensor is given in form of matrices, where the rows and columns equal the map of the sensor. Each frame represents a different moment in time as can be seen in Figure 4.8.

In order to have the highest accuracy and possibility for synchronization, recordings of 10 frames per second were taken, allowing recording of 800 frames per film. The idea was to take the force correctly measured by the Zwick (the distance is, e.g. measured accurately up to  $0.1 \mu\text{m}$ , analog for the force) and impose a correction factor on the Tekscan grid.

For the synchronization of the data files, i.e. the data of the Zwick (consisting of the measured force, covered distance, remaining distance and time passed since trial begin) and the Tekscan pressure sensor (pressure at a given point at a known time), both files had to be renamed with the commands `nametek` and `namezwick` leading to, e.g. `nametek='SQF 2-1.asf'` and `namezwick='SQF 2-1.xls'`. The files were non-equilibrated

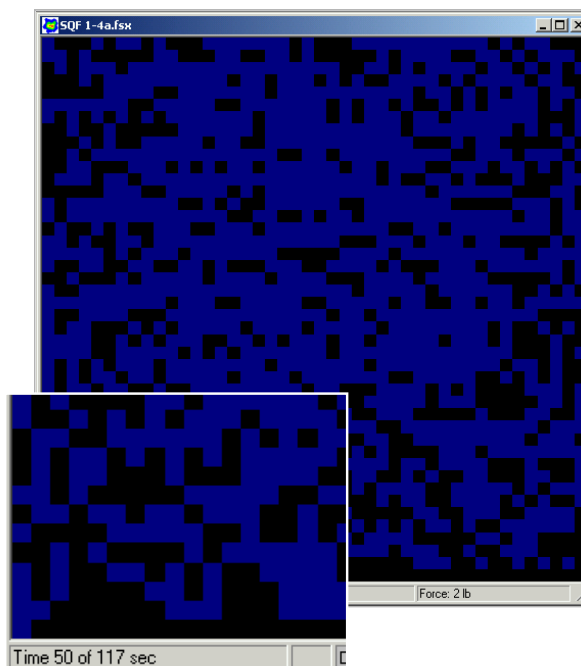


Figure 4.8: Example of a Tekscan time frame. The time is shown in the bottom left hand corner.

and non-calibrated when they were loaded into MATLAB with "tekreadnocal.m". Afterwards the following M-files were applied (the files can be found in the Appendix):

- timepoint.m\*: plots a particular point for all times
- timebase.m\*: function to find start, end, and maximum of all curves
- synchronise.m\*\* : function to set a common time frame for the Zwick and Tekscan data
- zwickforce.m\*\* : script to check the consistency of the Zwick data
- tekcorrection.m: function to do a point-wise automatic calibration of the Tekscan data to compensate for differing sensitivity between points
- crossfilter.m: function to smooth a matrix based on a cross shaped moving average kernel
- \* these files were loaded automatically when calling synchronise.m

- \*\* tekcorrection.m takes care of loading zwickforce.m and synchronise.m

The columns 1 to 9 mentioned in the files represent the following Zwick data (for an overview, see the list in the Appendix B): column one gives the force exerted on the Zwick crosshead while it moves downwards, column two shows the distance covered while descending, column three is the absolute distance, which is calculated by taking the original distance and subtracting the values of column two from it, and column four is the time which has elapsed since the beginning of the trial. The remaining columns five to nine contain data, which was determined with the help of the Stefan equation, see Chapter 2, such as the theoretical force on the crosshead, the theoretical plate distance, and values such as  $\frac{d}{a^3}$  or its cumulative integral. These calculations were all done within the zwickforce.m script.

The Stefan equation was assumed to be correct and taken as a reference. The Chapter carries the title “experimental verification of the FM model”. Hence, the verification refers to the assembly of the different established theories but not to the building blocks themselves. These have been extensively verified and are commonly accepted (see Chapter 3 for further details)

In the following the files are explained in more detail: the analysis of the data was started by loading the previously renamed Tescan (ASCII) and Zwick (Excel) files into MATLAB with the help of tekread.m. This script only extracts the desired information from the files and their headers. In order to compare the curves with each other and to synchronize them, common points on the curves had to be found, before a shift of one curve on the other could be carried out. This was done with the help of the M-file “timebase” (see Table B.1 in Appendix B for quick reference concerning the content of the files, and see also the Appendix for the complete files). Three points were targeted at in each curve: the beginning of the curve, the maximum, and the end. The  $x$  and  $y$  data is in form of a column vector. The beginning of the curve was found by approaching the curve from small  $x$  values. A threshold value of 10 % was set meaning that if while moving along the curve the increase from one  $y$ -value to the next is greater than 10 % (this value was empirically determined and agrees with the general

tolerance for errors; it assures that small changes due to inaccuracy of the system are not interpreted as changes) it was registered as the start. Continuing along the curve the endpoint was looked for, meaning the point where the change was not greater than 10 % (same reasoning as for the start point) anymore. The same procedure was taken for finding the maximum: the first value was set as the maximum and the loop continued along the curve until the found value was greater than the maximum, then this value was set to be the maximum and so on. This process continued until the point, where the following value was not larger anymore. This point was then determined to be the maximum. The curves have a steep maximum, meaning that only one frame in the film corresponds to the maximum and there are no ambiguities, the differences between the previous and following frame are clearly visible, see Figure 4.9. Here it can be seen that despite the visible color differences the raw sums of the data are different.

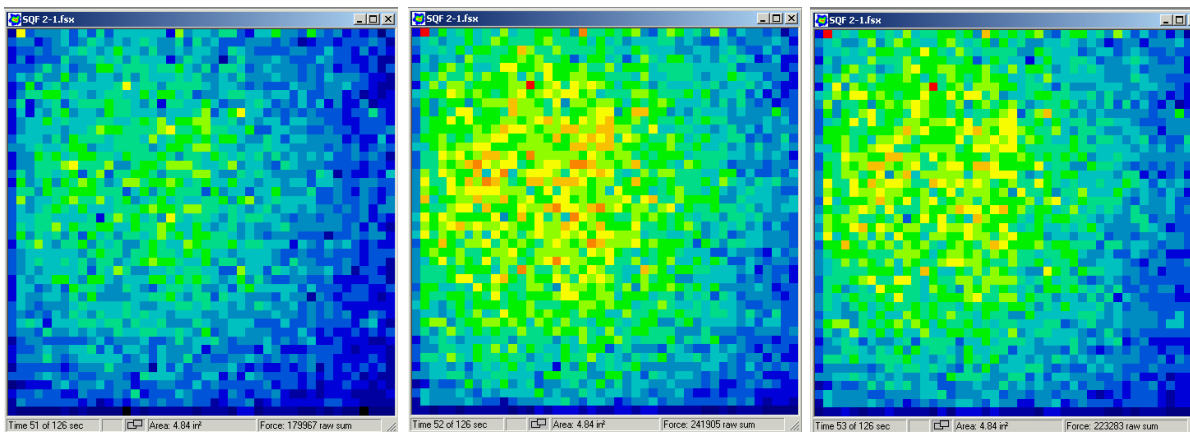


Figure 4.9: Illustration about the doubtlessness of finding the maximum frame: left 179967 raw units, middle 241905 raw units (maximum), right 223283 raw units.

A second function called `timepoint.m` (see appendix) made it possible to plot the Tekscan data taking single points and regarding their development over time. Afterwards the synchronization was carried out in order to set a common time frame for the Zwick and Tekscan data, see `synchronize.m` in the appendix. The basis for this synchronization is the previously mentioned `timebase.m` function giving three values of each curve: start, maximum, and end. By taking the end times of both sets of data and subtracting the Zwick time from the Tekscan time (since the Tekscan measurement was started earlier this value was bigger) the offset can be determined. Afterwards all

time values, i.e. the fourth column of Table B.1 of the Zwick files, had to be corrected by the offset.

The final but most complicated step was the synchronization of the data. This was done in four separate steps within the `tekcorrection.m` file:

1. checking of the Tekscan data since variations between the points can clearly be seen, e.g. Figure 4.8 or 4.9.
2. comparison of Tekscan and Zwick (which is believable due to its accuracy) data
3. construction of a matrix of values for all Tekscan sensels
4. multiplication of the Tekscan frame data by the corrected gain matrix from point (3)

Physical data like the viscosity (30 Pas) and the radius of the plates (0.05 m) was included in the file. Then the program files `zwickforce.m` and `synchronize.m` were applied. All old data was cleared. In order to complete step one, see above, a loop was programmed across all sensels. The radius of the sensor was the first value to be calculated. Where necessary a change of pressure units from psi to pa was applied. An offset was assumed for each of the points and added to the values. Afterwards once again the beginning, maximum, and end of the curves were found by running the `timebase.m` file on the Tekscan data. A control was done in order to assure that the sensels really worked. In step 2 (see list above) the stress in dependence of the radius  $r$  at a certain time was calculated for the Zwick data. Since the Zwick stopped recording at the moment where the top plate started moving upwards, there was less time data, hence this had to be carefully looked out for. The endpoint of the Tekscan might not necessarily be in accordance with the Zwick data, since the Tekscan was stopped manually once the Zwick had finished the compression. Therefore, if this was the case the last value of the Zwick was taken as the endpoint and a warning was issued: “not enough late Zwick time data for  $(x, y)$ ”. Analogical for early Zwick data. In the third step the multiplier for the Tekscan data was determined by dividing the value given

by the Zwick by the value given by the Tekscan. If the offsets of certain sensels were too big, their multiplier was set to be zero, hence, they were treated as not working and therefore excluded. In the fourth and last step the corrected gains and offsets were propagated frame by frame through all Tekscan data.

In order to check the effectiveness of the calibration (i.e. if points at e.g. the same radial distance measure the same pressures) a cross-filter can be applied afterwards. This cross-filter function averages over eight adjacent points, and therefore smoothes the surface of the data's graphic, see the appendix for the `crossfilter.m` file.

### 4.2.6 Trial procedure

At the beginning of each trial, before loading the sample, a routine was carried out for all trials. Once the sensor had been placed into its form on the plate the separable rings were inserted into the flute. Then the fluid (highly viscous silicon oil, see above) was placed onto the plate resembling a small cylinder up to the fill line of 5 mm. It was left on the plate for around 30 minutes to assure the escape of possible air bubbles. Afterwards the crosshead was moved down until a height of approximately 5 mm (the current position of the crosshead can be tracked in the Zwick programm once the zero point has been set correctly, see calibration Section). When the 5 mm limit was reached, i.e. the top plate touched the fluid and caused a change in force shown by the Zwick, the actual height of the crosshead, e.g. 5.004 mm, was noted. This was necessary to do the backwards calculation (if done manually) for the Zwick data later on. The software of the Zwick only gives the distance it has covered but not the absolute distance, which is needed for the Stefan equation. Once the upper plate touched the fluid, the separable ring could be removed because the fluid holds due to surface tension.

For manual as well as MATLAB calibration it had to be absolutely remembered that the Tekscan measurement needed to be started before the Zwick recording. Once the Tekscan had started its recording, the Zwick crosshead could start its downward movement at the speed of 0.0001 m/s.

For the pure fluid trials the crosshead moved down until it reached the distance  $25\ \mu\text{m}$ , before it went back to the initial length of 5 cm (this is called "LE" length in the software, a term originally coming from German and referring to extensional measurements). For trials with particles the crosshead moved down until the plate touched the particle.

During the MATLAB calibration it turned out that the expected force determined with the help of the Stefan equation (e.g. 0.2 kPa) was always lower than the experimental values (e.g 1.7 kPa), suggesting that the plates were in fact closer together than indicated by the Zwick. This was due to the neoprene patch (the difference in force corresponded to a gap difference of 1.5 mm, which was exactly the thickness of the patch). The patch was probably completely compressed during the zeroing process of the Zwick since it was loaded with a force of 2.5 N before the zero distance was set. Hence, it was decided to remove the patch since the instrumental equilibration and calibration where the non-compliant surface posed a problem were no longer necessary (due to MATLAB processing of the data).

### 4.3 Trials

For all trials the system was equilibrated and calibrated, except when stated otherwise. A list of the possible equilibration and calibration methods can be found in Table 4.1. Not all possible combinations of these methods were carried out since some of them were not successful and it is not reasonable to conduct a calibration of a previous unsuccessful equilibration. An overview of the trials carried out is given in Tables 4.2 and 4.3. After a preliminary squeeze flow trial (see no. 0), the first trial series focusing only on the equilibration and calibration conditions (see Table 4.2) was conducted. A second series dealing with pure squeeze flow (see Table 4.3, no. 0 - 8) and a third series incorporating particles (no. 9 - 11) were carried out afterwards. The equilibration and calibration methods used can be found in the last column of the Table, the numbers refer to the different methods described in Section 4.2.5 and also Table 4.1. The aim was to find a smooth curve following the pressure profile theoretically determined with

Table 4.2: Overview of the equilibration and calibration methods tried (for a full list of the possible methods see Table 4.1).

no.	equilibration and calibration method	equ./cal. no.
0	PSP (p1 & p2), sensor 138 kPa	none
A	upper plate contact for equilibration and calibration, extra weight, sensor 138 kPa	1/1
A1	upper plate, tissue contact for equilibration and calibration, extra weight, sensor 138 kPa	1a/1a
B	equilibration with the bladder, calibration with cubic objects plus extra weight , sensor 138 kPa	2/2
C	equilibration and calibration between Zwick plates, neoprene, sensor 138 kPa, sensitivity of the sensor "high-2"	3/3
C1	equilibration and calibration between Zwick plates, neoprene, sensor 138 kPa, sensitivity of the sensor "mid-1"	3/3

the help of the Stefan equation for the pure fluid. In the following cascade of trials the modifications for each trial were due to the results and conclusion of the precedent trial. This is explained in detail in the results Section of this Chapter and discussed afterwards. Trials A - C1 were conducted in order to evaluate different equilibration and calibration methods. All trials were carried out at least in triplicate in order to receive an idea about the variation of the retrieved data.

### 4.3.1 Dimensional analysis

A dimensional analysis aiming at the compatibility of the experimental set-up with the in-mouth situation was done. The dimensionless number, which was to be found, incorporated the variables contained in the Green functions, i.e. the pressure (threshold)  $\Delta p$ , the fluid viscosity  $\eta$ , the plate velocity  $\dot{d}(t)$ , the plate distance  $d(t)$ , and the

Table 4.3: Overview of squeeze flow trials with (no. 9 - 11) and without (0 - 8) particles.

<b>no.</b>	<b>trial description</b>	<b>equ./cal. no.</b>
0	parallel steel plates (PSP) (p1 & p2), sensor 138 kPa	none
1	PSP (p1 & p2), compliant top plate, sensor 138 kPa	1/1
2	PSP (p1 & p2), compliant top plate, sensor 138 kPa	2/2
3	PSP (p1 & p2), compliant top plate, levelling film, sensor 138 kPa	2/2
4	PSP (p1 & p3), compliant top plate, milled out center piece of the plate (new plate, named plate 3), sensor 138 kPa	2/2
5	PSP (p1 & p3), compliant top plate, sensor 138 kPa	none:(MATLAB)
6	PSP (p1 & p3), sensor 138 kPa	none:(MATLAB)
7	PSP (p1 & p3), sensor 138 kPa	3/3
8	PSP (p1 & p3), sensor 345 kPa	3/-
9	PSP (p1 & p3), sensor 138 kPa, particle with 1 mm radius	none
10	PSP (p1 & p3), sensor 138 kPa, particle with 1 mm radius	3/-
11	PSP (p1 & p3), sensor 345 kPa, particle with 1 mm radius, fluid 300 Pas	3/3

particle radius  $a$ . The following units according to SI units were considered

- $[\Delta p] = Pa$
- $[\eta] = Pas$
- $[\dot{d}(t)] = \frac{m}{s}$
- $[d(t)] = m$
- $[a] = m$

With these units Table 4.4 can be obtained from which the matrix  $A$  can be taken when considering the last three columns according to Rao (1996).

$$A = \begin{pmatrix} 1 & 1 & 0 \\ -1 & -1 & 1 \\ -2 & -1 & 0 \end{pmatrix} \quad (4.1)$$

The remaining two columns make up matrix  $B$

$$B = \begin{pmatrix} 0 & 0 \\ 1 & 1 \\ -1 & 0 \end{pmatrix}. \quad (4.2)$$

In order to obtain a third matrix  $C$  the inverse of matrix  $A$

$$A^{-1} = \begin{pmatrix} -1 & 0 & -1 \\ 2 & 0 & 1 \\ 1 & 1 & 0 \end{pmatrix} \quad (4.3)$$

needs to be multiplied with matrix  $B$  before the transpose is taken of this matrix product and the result is multiplied by minus one.

$$C = -(A^{-1} B)^T = \begin{pmatrix} -1 & 1 & -1 \\ 0 & 0 & -1 \end{pmatrix} \quad (4.4)$$

Table 4.4: Variables and units for the dimensional analysis.

	$\dot{d}$	$d$	$\Delta p$	$\eta$	$a$
M	0	0	1	1	0
L	1	1	-1	-1	1
T	-1	0	-2	-1	0

Table 4.4 has to be extended by this matrix by placing it underneath the rows, which correspond to matrix  $A$ . The part underneath matrix  $B$  is extended by an identity (square matrix). The new rows are labelled with  $\pi$  and its ascending indices (according to the Buckingham  $\pi$ -theorem (Buckingham, 1914)). This leads to Table 4.5 from which the dimensional quantities  $\pi$  can be easily read off, leading to

$$\pi_1 = \dot{d}^1 d^0 \Delta p^{-1} \eta^1 a^{-1} = \frac{\dot{d} \eta}{\Delta p a} \quad (4.5)$$

or the first dimensionless number and

$$\pi_2 = \dot{d}^1 d^0 \Delta p^{-1} \eta^1 a^{-1} = \frac{d}{a} \quad (4.6)$$

for the second dimensionless number.

Table 4.5: Variables and units for the dimensional analysis.

	$\dot{d}$	$d$	$\Delta p$	$\eta$	$a$
M	0	0	1	1	0
L	1	1	-1	-1	1
T	-1	0	-2	-1	0
$\pi_1$	1	0	-1	1	-1
$\pi_2$	0	1	0	0	1

Only  $\pi_1$  is further considered and referred to as  $\pi$  since  $\pi_2$  is only a length scaling not leading to any information considering pressure sensitivity or experimental variation.

If the dynamic viscosity in equation (4.5) is written in form of the kinematic viscosity  $\mu$  and density  $\rho$  and at the same time the equation is expanded by a factor  $\dot{d}$  it can easily be seen that the dimensionless number used is equal to the product of the reciprocal product of the Euler and Reynolds number.

$$\pi_1 = \frac{\dot{d}\eta}{\Delta p a} = \frac{\frac{\mu \rho \dot{d}}{a}}{\Delta p} = \frac{\rho \dot{d}^2 \frac{\mu}{\dot{d} a}}{\Delta p} = \frac{\rho \dot{d}^2}{\Delta p} \frac{\mu}{\dot{d} a} = \frac{1}{\text{Eu}} \frac{1}{\text{Re}} \quad (4.7)$$

Since it is a dimensionless number the inverse of the number, i.e. the product of the Reynolds and Euler number can be taken. In the following discussion  $\pi = \text{Eu Re}$ .

When evaluating in-mouth (subscript ‘im’) and instrument (subscript ‘instr’) parameters this number has to be the same due to its dimensionless character. For the in-mouth condition a pressure threshold of 10 kPa was assumed according to Johansson & Olsson (1976). More recently Booth et al. (2003) assumed 0.1 N for perceptive fields of  $20 \mu\text{m}^2$  leading to 5 kPa as a threshold value for in-mouth pressure, which is of the same order of magnitude. The velocity at which tongue and palate approach each other was set to be  $10^{-1}$  m/s (deducted from data of Mioche et al. (2002)). Furthermore it was assumed that fluids slightly higher viscous than water have the tendency to contain particles, i.e. the viscosity was thought to be  $10^{-2}$  Pas. The particles investigated were of 100  $\mu\text{m}$  radius. This lead to the following number for  $\pi_{im}$

$$\pi_{im} = \frac{10^4 \text{Pa} 10^{-4} \text{m}}{10^{-2} \text{Pas} 10^{-2} \text{m/s}} = \frac{1}{10^{-4}} = 10^4. \quad (4.8)$$

For the instrumental number different parameters were taken: the pressure threshold was assumed to be 3 kPa, which equals the sensitivity of the sensor, when taking into account the internal threshold and an additional security. Furthermore the plates were moving together at a speed of 0.0001 m/s in all trials. The viscosity of the sample fluid was 30 Pas in most trials, and the particle size 0.001 m in radius. This lead to the following relation for the instrumental set-up

$$\pi_{instr} = \frac{3 \cdot 10^3 \text{Pa} 10^{-3} \text{m}}{10^3 \text{Pas} 10^{-4} \text{m/s}} = \frac{1}{10^{-4}} = 10^4. \quad (4.9)$$

Since both values for  $\pi$  result in the same value the trial is generally suitable to prove the in-mouth situation. Unfortunately the indication on the sensor about its resolution was not reliable. If a sensor with the mentioned resolution (i.e. noise maximum of 3 kPa) can be found a realistic extrapolation from the experimental to the in-mouth situation should be possible.

## 4.4 Results & discussion of the trials

The trial series “0” was carried out for the general evaluation of the system. The idea was to check if the sensor records any changes when a fluid is posed on it and squeezed together between the parallel plates (final distance  $< 1$  mm). No equilibration or calibration was done for this trial. A pressure profile could be seen (see Figure 4.10) in the recording but the measurement was noisy. The white line represents the midpoint of the sensor. Going right and left from the midpoint on the  $x$ -axis the pressure profile should smoothly decay according to the Stefan equation. The variations from one cell to the next were of up to 50 raw units (knowing that the measuring range of the sensor is 138 kPa this can be determined to be approximately 30 kPa with the law of proportion).

For a sensor with a measuring range of 138 kPa and a resolution of 256 raw units the pressure variations from one cell to the next should be no more than 500 Pa (1.5 kPa if the preset threshold of the sensor, i.e. 3 raw units, is taken into account). In order to obtain this accuracy, equilibration and calibration were done. One complete series (see Table 4.1 and Table 4.2 for explanation of the methods) was carried out to investigate these two trial parameters.

### 4.4.1 Equilibration and calibration trials (A - C1)

As described in Section 4.3, the sensor was loaded with different contact surfaces for the equilibration. The results can be seen in Figure 4.11. For loading with the steel

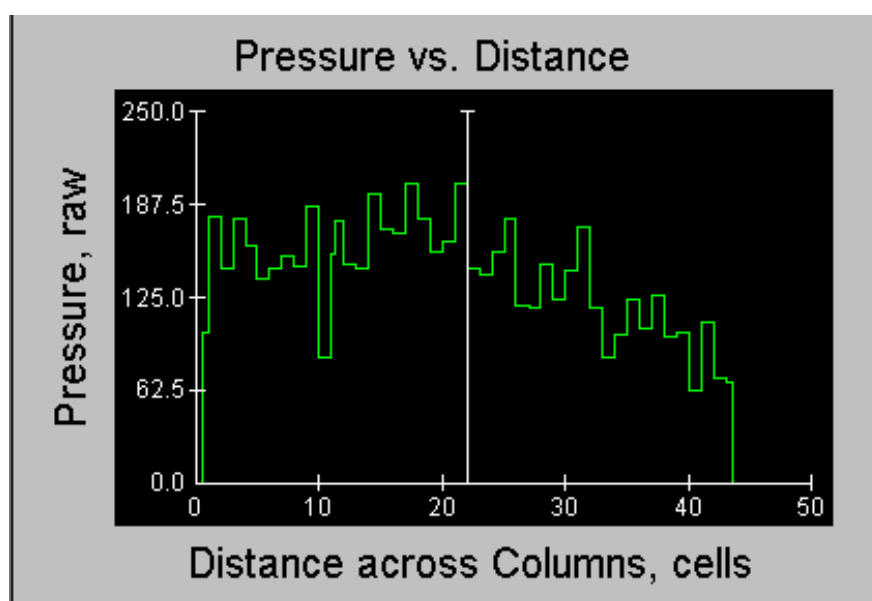


Figure 4.10: Pressure profile across the sensor middle shortly before the maximum pressure was reached (the white line represents the midpoint of the sensor), the system was unequilibrated, uncalibrated, trial 0.

plate (equilibration method 1, trial A) not a lot of sensels were stimulated (left). More sensels were stimulated when a tissue was placed between the plate and the sensor (trial A1) or when equilibration method 2, i.e. equilibration with the bladder (trial B), was used.

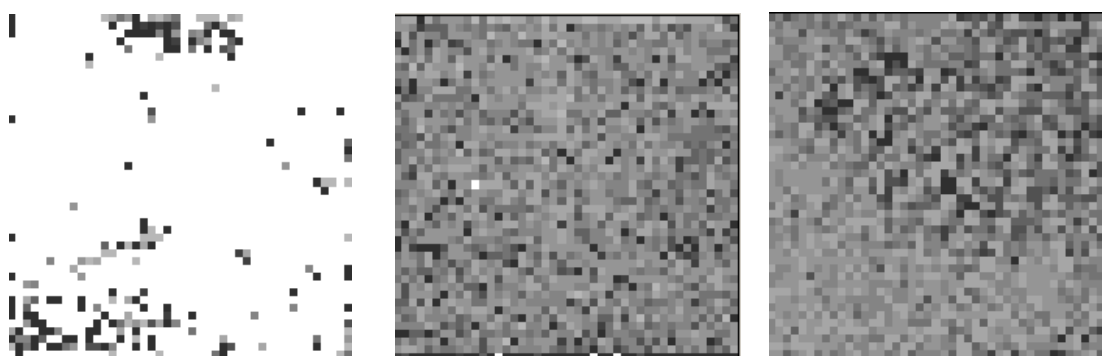


Figure 4.11: Comparison of different equilibration methods, from left to right: method 1 (steel plates), method 1a (steel plates and tissue), and method 2 (bladder).

For the calibrations following the above mentioned equilibrations, the results were

similar. Loading the steel plate (1.423 kg) in direct contact with the sensor with additional weight of 1.5 kg, so that a total load of 29.4 N was imposed on the sensor lead to an extrapolation of the measuring range of 596 kPa (trial A). This is unrealistic for a sensor labelled 138 kPa (explanation see above). Calibration for the plate and tissue set-up lead to extrapolation of 109 kPa (trial A1). This value was closer to the real value but still not correct. The calibration for the bladder equilibrated trial took place with caoutchouc cubes of 2 x 2 cm<sup>2</sup> surface area (the previously mentioned steel cubes did not result in a satisfactory contact area). The contact area of 4 cm<sup>2</sup> resulted in 256 loaded sensels, which is very close to the 251 sensels, i.e. the corresponding value for this contact area. The sensor extrapolated a saturation pressure of 138 kPa, i.e. the value noted on the sensor (trial B). This seemed like a very good result but not when keeping in mind that the equilibration file, which is ultimately the basis to see pressure disturbances, was not smooth (see Figure 4.11, right).

In the next step another equilibration was applied (trial C). For this the plates were mounted to the Zwick texture analyzer, a compliant surface (i.e. a neoprene patch such as a mouse-pad) was placed between them before they were moved together until contact was reached. In this case the load was distributed very evenly and at the same time the exact load could be read off from the Zwick. Another feature was tested in the framework of this trial: the sensitivity settings in the acquisition parameter menu of the Tekscan sensor were changed from "high-2" to "med-1" sensitivity (trial C1) from one trial to the next. The results can be seen in Figure 4.12. (The empty line in the right hand figure is due to a broken wire of the sensor). No significant difference can be seen between the graphs.

#### 4.4.2 Squeeze flow trials (1 - 11)

In the following step actual squeeze flow measurements were carried out. Since these turned out to be rather difficult even without particles, particles were only incorporated at the very last step (trials 9 and 10). The first trial in Table 4.3 is the preliminary trial mentioned previously but since it dealt with squeeze flow it is mentioned in this Table

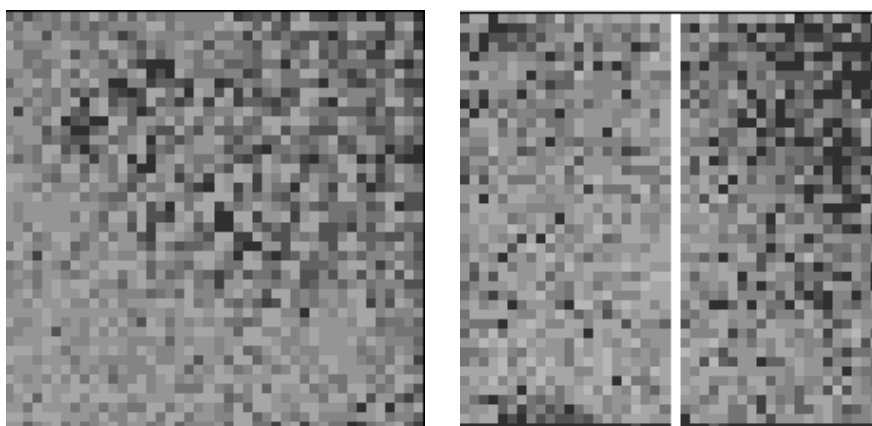


Figure 4.12: Equilibration method 3 (Zwick) and the influence of different sensitivity settings (high-2 and med-1) on the evenness of the equilibration file.

for completeness. Trial 1 used the calibration with the two steel plates (calibration method 1), but for the measurement a compliant surface (neoprene) was attached to the top plate. Trial 2 was identical except that equilibration was carried out with the bladder (equilibration method 2) and calibration with the caoutchouc cube (calibration method 2). Neither one of these trials resulted in less noise than trial 0, i.e. the trial without any equilibration or calibration.

The third trial (equilibration/calibration 2/2) differed by the added levelling film from the other trials (see Section 4.2.4). Still, even with the film no satisfactory smooth squeeze flow profile was obtained. In addition to that the film did not stay in its place and fluid went underneath, therefore a flat surface, which is absolutely necessary for parallel plate squeeze flow, could not be guaranteed.

For trial 4 (equilibration/calibration 2/2) the shape of the sensor was milled out from the plate in the thickness of the sensor (see Section 4.2.4). No significant differences from the 0 trial could be noticed, therefore, the graphs are not presented here.

Trials 5 and 6 were done without equilibration and calibration since this was done afterwards with the help of MATLAB (see Section 4.2.5). The difference between trial 5 and 6 was that the neoprene patch was removed for the sixth trial due to the reasons mentioned in Section 4.2.6. The differences between the uncalibrated (Figure 4.13) and

calibrated (Figure 4.14) profile were not satisfactory. The graphs are nearly identical.

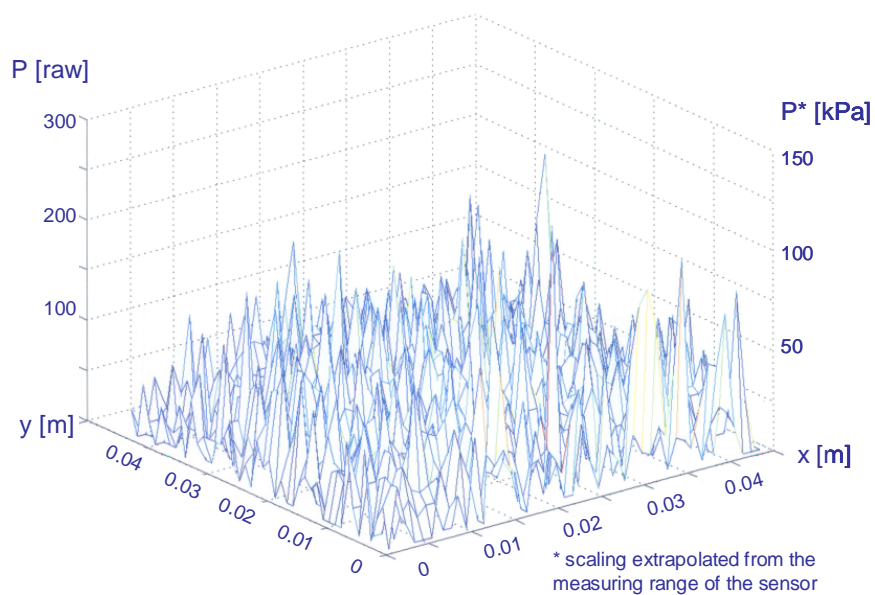


Figure 4.13: Pressure profile of uncalibrated squeeze flow (MATLAB) without neoprene patch.

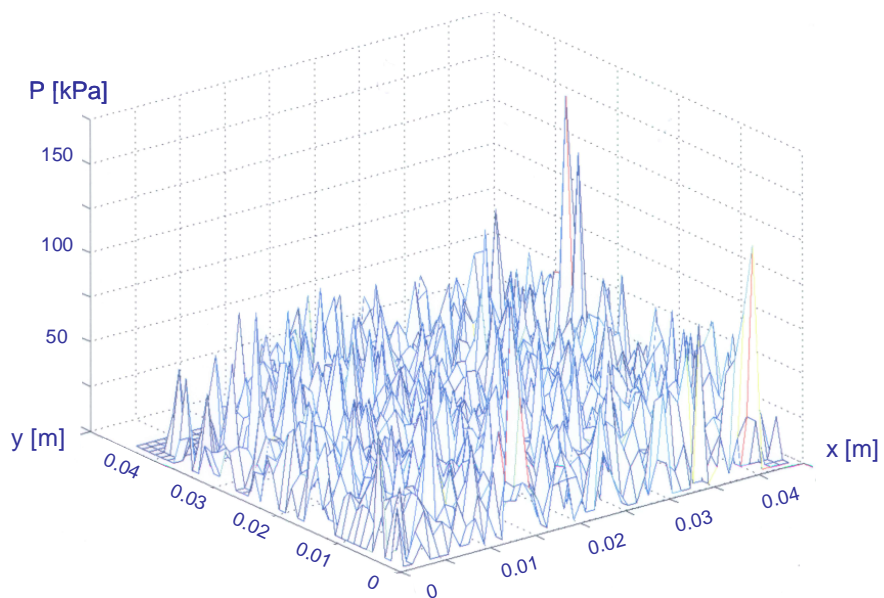


Figure 4.14: Pressure profile of squeeze flow calibrated retrospectively with MATLAB, without neoprene patch.

Not even the theoretical equilibration and calibration, which took into account the accurate and believable force data of the Zwick strain frame resulted in a profile smooth enough to include a particle, which could effectively be seen.

Therefore, in one more step (trial 7) the equilibration and calibration were carried out with the Zwick strain frame (see equilibration/calibration method 3/3). Different settings for the sensitivity were tried, starting with "default" and going up to "high-2" (maximum) sensitivity. As already stated previously for the pure equilibration and calibration this did not significantly change the outcome. Figures 4.15 and 4.16, which each show three repetitions of the same trial, make it possible to illustrate the influence equilibration and calibration have.

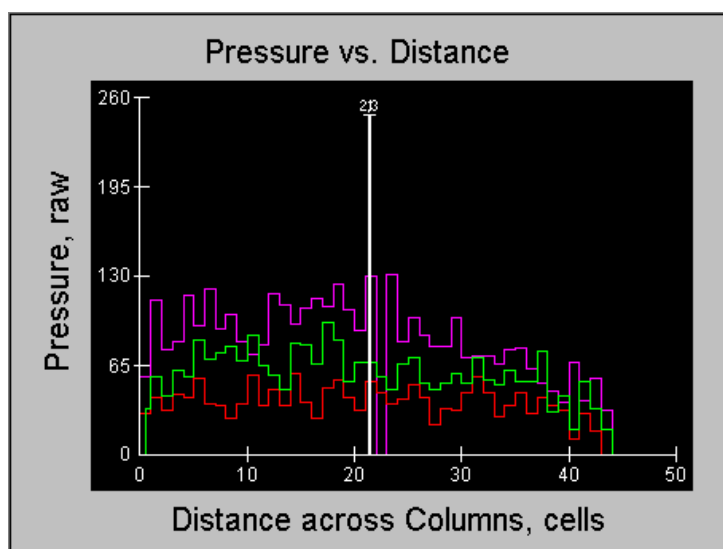


Figure 4.15: Squeeze flow between steel plates, not equilibrated or calibrated (trials as triplicates).

Attention is necessary because at the first look Figure 4.16 appears smoother and less noisy, but it has to be kept in mind that here the fluctuations are in kPa and there are fluctuations of around 30 kPa. The scale of Figure 4.16 is in raw units of pressure (the trial is not calibrated, hence, it is not possible to show units) so that that the noise level is in fact equal in both, when determined with the law of proportion.

At the same time the curves show that variation of the data is enormous. The three

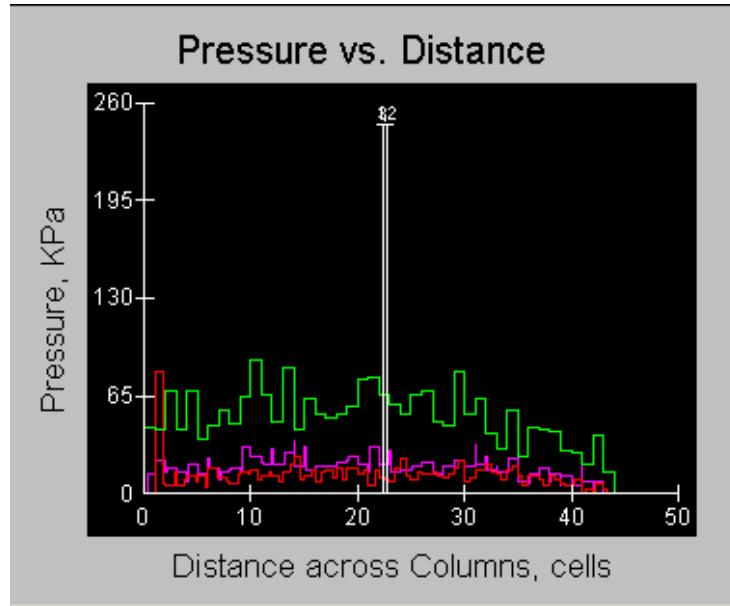


Figure 4.16: Squeeze flow between steel plates, equilibrated and calibrated according to 3/3.

curves in each graph represent identical trials. Hence, the curves should be the same. Even if the curves are not exactly at the same moment in time, they should still show the same profile with a certain offset. In order to check variation of the data in more detail, the data of trial 7 was exported into Excel and synchronized so that the three curves had the same start and end point. The curves were compared at the same moment in time, i.e. at a plate distance of 1.53 mm (see Figure 4.17). The Figure shows once more that the result is very noisy. The high fluctuations are not shown for the same sensels otherwise it could be concluded that certain sensels have a large offset. No regularity could be found in the data.

Up to here all trials were carried out with the 138 kPa (20 psi) sensor. As another option the 345 kPa (50 psi) sensor was used (trial 8) in order to see at which plate distance the profile is smooth enough to possibly see a particle. The 345 kPa sensor was only equilibrated (equilibration method 3). The particle size necessary to have a signal larger than the sensor noise needed to be determined afterwards. The smoothest profile that could be found can be seen in Figure 4.18, but even here raw pressure fluctuations of 35 units (equalling to approximately 45 kPa) could be found.

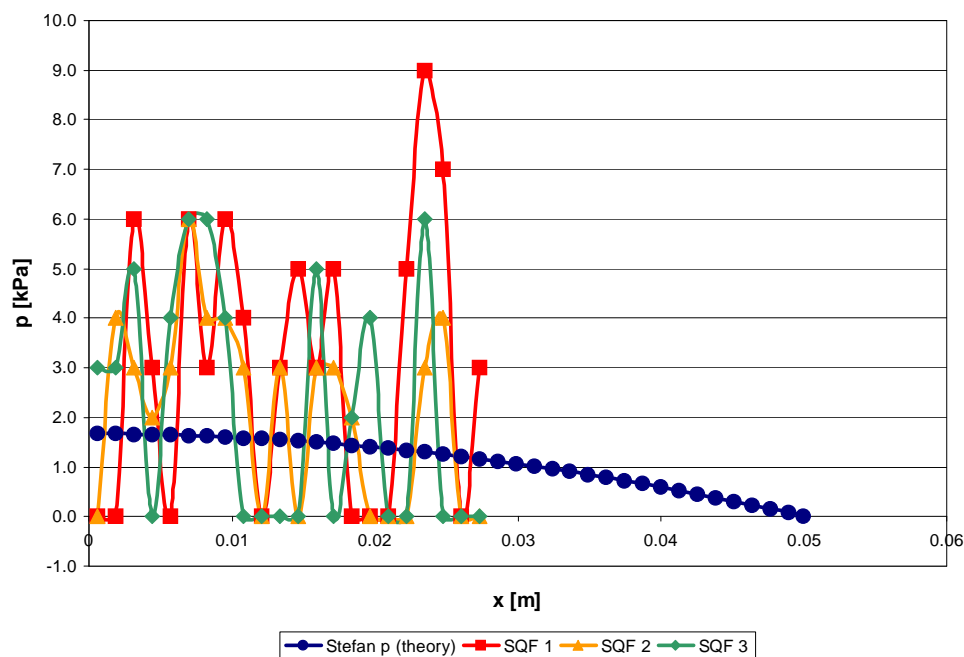


Figure 4.17: Squeeze flow between steel plates, calibrated according to 3/3.

Despite the fact that the trials with pure fluid were already very unsatisfactory a few trials were carried out in order to try the experiment with particles, i.e. to see if the movement of a particle can actually be seen on the sensor. Knowing that a particle of 0.001 m (1 mm) radius should cause a significant pressure field disturbance as determined at the end of Chapter 3, 1 - 3 particles of this size were added to the fluid (trial 9) before moving the upper plate down. They were placed into different quadrants of the sensor (Figure 4.19) in order to be sure they would not influence each other (for this case the theory is not valid). They were also placed in the outer triangle of the quadrant since the particle has more influence in this area (see Chapter 3). At least one quadrant was always left empty in order to have the zero comparison. Since the sensor allows evaluation of the data in several different manners one being the possibility to draw a horizontal line across one row of the patch, a gradually mounting line with its highest point in the middle due to the fluid profile was expected. There should have been a slowly increasing peak where the particle(s) is/are since the disturbance caused by the particle was supposedly to this extent larger. Ideally the radial movement of

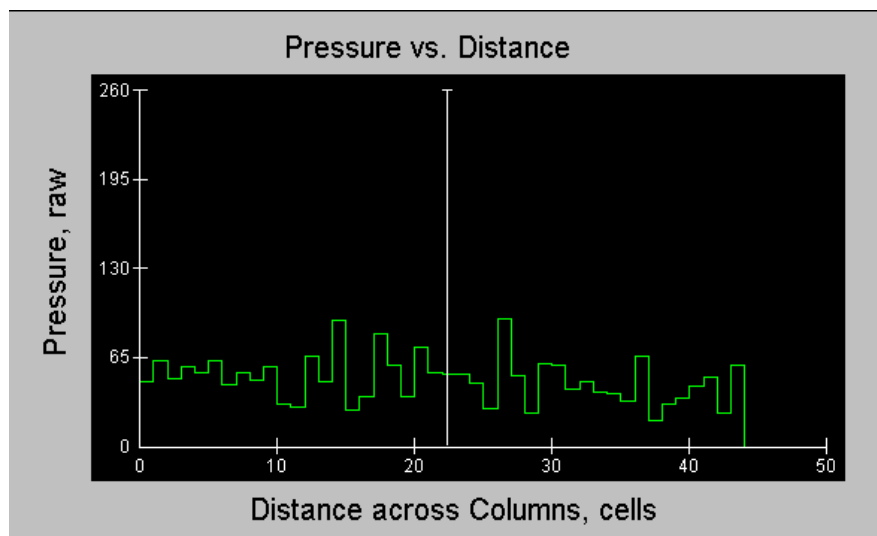


Figure 4.18: Investigation of a pressure sensor with a larger measuring range, 345 kPa, search for the smoothest profile.

the particle should be tracked across the sensels. If the sensor was sensitive enough the positive pressure in front of the particle and the negative pressure behind the particle relative to the fluid flow curve should even be seen. At the end the sensel should be saturated because the plates were moved so close together so that the particle got stuck. This was done in order to be able to know where to check for the particle disturbance when regarding the film. Trial 9 was carried out on an unequilibrated basis, whereas trial 10 investigated the same particle containing squeeze flow under equilibrated (equilibration method 3) conditions.

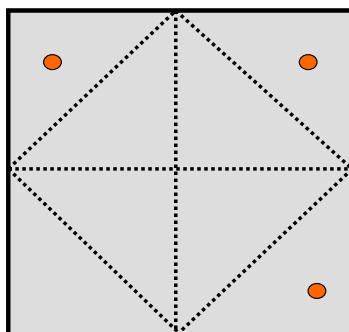


Figure 4.19: Particle layout on the sensor: one quadrant was left free for comparison purposes.

In both cases only one particle was included in the third (when counting clockwise) quadrant. The development of the flow field in time can be seen in Figures 4.20 and 4.21. Since not very many changes could be registered over time for the equilibrated situation only four frames were included. For both trials it can be concluded that the particle is only registered when it actually touches the plate because there are only four frames, i.e. one second, between the moment where no particle is seen and when saturation (red) occurs.

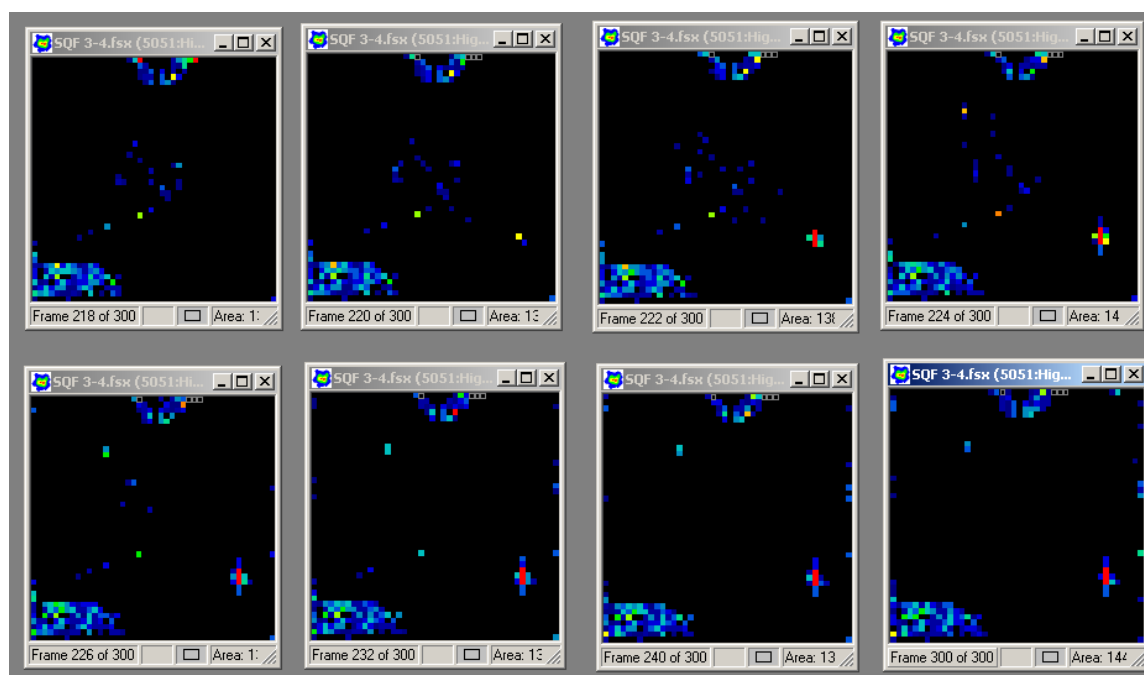


Figure 4.20: Tracking of a particle placed at the bottom right corner through a fluid under non-equilibrated conditions.

In trial 11 a fluid with higher viscosity, i.e. 300 Pas was used. The results can be seen in Figure 4.22. Pressure differences can be seen between the middle and the edge but neither the expected concentric rings nor the particle can be seen.

These findings clearly demonstrate that the Tekscan pressure system is not suitable to fulfill the experimental verification of the mathematical model despite the claims of the supplier. All possible equilibration and calibration were done without any satisfactory result. The particle sizes, which would according to the mathematical theory with

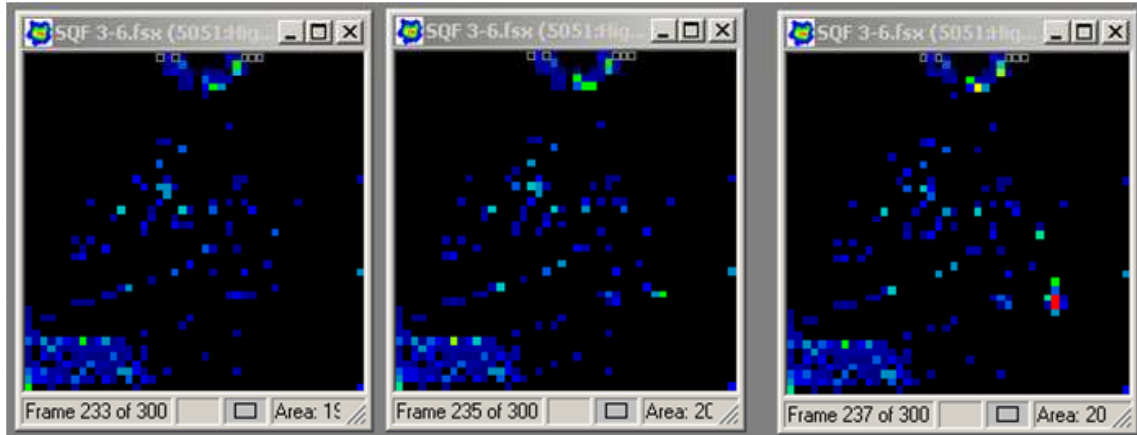


Figure 4.21: Tracking of a particle placed at the bottom right corner through a fluid under equilibrated conditions (equilibration method 3).

sureness cause a visible signal (hundreds of kPa), are in the  $\mu\text{m}$ -range and therefore impossible to handle as single particles. The resolution of the sensor is not sufficient to see variations between individual sensels as it would be necessary in order to actually track a particle.

Even if it was possible to handle particles in the  $\mu\text{m}$ -range, the resulting pressure fluctuation determined in Chapter 3 are orders of magnitude larger, but these stresses occur at very small surfaces. Hence, when the sensel on the sensor is stimulated this large stress might get evened out due to the surface of the sensels because the sensel does not differentiate between full surface stimulation and partial stimulation. The pressure will then be shown as a much smaller stress, which might not be capable to differ from the noise.

Yates et al. (2001), who used a similar set-up and the same sensor for their investigations on squeeze flow of pastes and also worked with the Stefan model obtained the curves shown in Figure 4.23. When evaluating the measured data Yates et al. (2001) used an algorithm, which averaged over the circumference. This was not possible in this study since such an algorithm would have also averaged out the peak caused by the presence of the particle. When looking at these curves it also becomes evident that the system shows very high fluctuations. The measuring points shown in the graphic

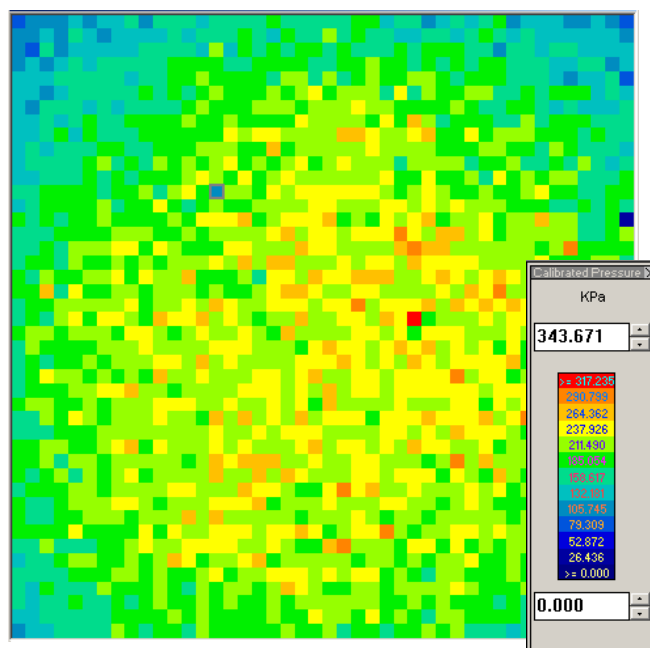


Figure 4.22: Squeeze flow for highly viscous (300 Pas) fluid containing a particle of 1 mm diameter.

already represent averages, still they fluctuate around the theoretical curves.

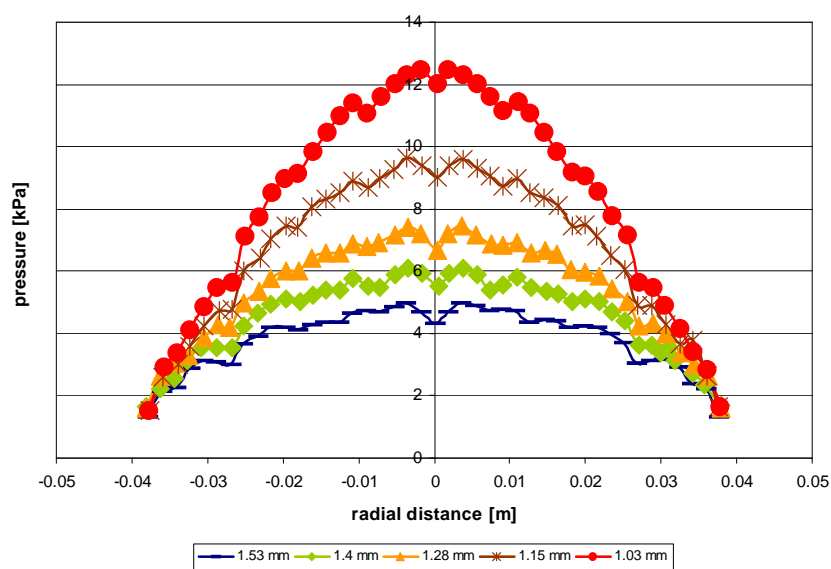


Figure 4.23: Squeeze flow trials conducted by Yates et al. (2001) with a similar trial set-up. The curves correspond to different plate distances in mm during the squeeze flow.

The dimensional analysis shown in Section 4.3.1 illustrates that generally with the parameters calculated with the help of the mathematical model the trial according to the described set-up should be possible and finally the extrapolation to the in-mouth situation as well.

# Chapter 5

## Conclusions and future aspects

The aim to understand textural perception in mouth is consistent with the claim made by Wansink (2005) concerning product development: “Just as marketing is too important to be left only to marketers, product development is too important to be left only to technical product developers”. The reason why a lot of new products fail is because the developers loose sight of the consumer. Products might be improved with great creativity and award-winning technology but if they do not correspond to the consumers’ needs, e.g. their preferred texture sensation, they will not be successful. This makes it evident why it is necessary to understand texture perception. Nevertheless very little is known about how the human mouth detects texture with the help of tongue and palate. Even for differences in the geometry of objects to be perceived in the mouth, such as differences in height and diameter, only little information is available.

The main aim of this work was to understand the mechanisms of texture perception. This is in order to be able to design foods with tailored texture properties or to adapt existing methods for the analysis of food texture to in-mouth conditions in the future. The sensitivity for geometrical differences and the detection mechanisms in the oral cavity, as discussed in Chapter 2, are the basis for the explanation of sensory attributes such as ”grittiness”. Chapter 3 and 4 deal with the perception of grittiness, which from a fluid dynamics point of view was postulated to be the perception of stress field

fluctuations. For this, existing theories were assembled in a new way in order to explain perturbations in a fluid caused by the presence of the particle.

This makes it possible to give answers to the six questions posed at the end of Chapter 1. The first three questions referred to the geometrical resolution in-mouth and the remaining questions to the perception of grittiness:

**How sensitive is the human mouth to geometric size differences when evaluated between tongue and palate?**

The in-mouth sensitivity in the horizontal or tangential direction is at least 1 mm and is consistent with anatomical data, such as the spacing of the mechanoreceptors. In vertical direction a discrimination threshold of 25  $\mu\text{m}$  was obtained. This value depends on the thickness range the disks originate from and on the structural resistance (thickness, diameter, and material).

**What are the detection processes?**

For the detection of the standard disks an unexpected non detectable range for which the differentiation threshold was much larger than 25  $\mu\text{m}$  resulted. Since differentiation above and below this range was possible it led to the hypothesis that there is a coexistence of two detection processes: Bending for thin and flexible disks (up to 125  $\mu\text{m}$  in thickness) and impressing into the tongue for thick or stiff disks (above 200  $\mu\text{m}$  in thickness), both for a material stiffness of 480 MPa. In the interval between these two ranges forces, which are physiologically not possible, would be needed for the deflection. At the same time the soft papillae on the tongue inhibit the sensitive judgement of the tongue deformation unless they are completely compressed (this is consistent with the papillae height, which is approximately 200  $\mu\text{m}$ ).

**How can these processes be expressed with the help of mathematical models?**

The process of alignment was described with a mathematical model based on Timoshenko's linear plate theory (Timoshenko & Woinoswky-Krieger, 1959).

This model allowed the calculation of the normal force intensities exerted on the disks as a function of the radius. Additionally, material parameters for additional trials aiming at the confirmation of the hypothesis could be determined. Evaluation of a stiffer and more compliant material confirmed the hypothesis about the existence of two detection processes, hence, validating the mathematical model.

Of course this does not mean that there are no other possible ways of approaching or explaining this problem, but so far no approach has led to a more plausible explanation. Additionally the *in vitro* confirmation of the disk bending, i.e. application of loads on the disks *ex vivo* has not been carried out within the framework of this thesis. Still a two-fold confirmation was conducted in order to test the mathematical model, which confirms the theory.

There are certain limitations of the proposed model. So far the process of impressing the disk into the tongue has not been modeled. This is mainly due to the lack of knowledge about the mechanical properties of the tongue. It is inevitable for these calculations but very difficult to determine due to the non-static character of the tongue body.

**How does a human being perceive grittiness in the oral cavity? Could it be the perception of stress field perturbations? What do these perturbations look like?**

The hypothesis was that particle caused stress field variations in the fluid are responsible for the sensation of “grittiness” in liquid foods.

The stress distribution for pure squeeze flow (no particles), which was described with the pressure form of the Stefan equation was considered as the blank value. This results in a parabolic profile of the pressure when plotted in dependence of the radius. In order to be able to identify particle related disturbances, these had to be larger than the noise of the sensor, which was attached to the bottom plate in a trial set-up. The force due to the presence of a particle was determined with Faxen’s law. The Green functions incorporating this point force allowed the characterization of the disturbed

stress and velocity field. With the experimental parameters used, i.e. fluid viscosity of 30 Pas, velocity of the upper plate =  $10^{-4}$  m/s, plate distance of 0.002 m, and a plate radius of 0.05 m, it could theoretically be determined that a particle of 0.001 m radius should cause stress fluctuations of at least 1000 kPa. The sample point has to be chosen so that it is not directly underneath the particle as this would result in a zero pressure due to the characteristic disturbance: the pressure is positive in front of and negative behind of the particle (with reference to the flow direction of the fluid). These stress field disturbances should be spotted by a sensor sensing normal stresses, which has an internal threshold of 3 raw units, with the resolution of 256 raw units and a pressure range of 138 kPa, since this leads to a noise threshold of approximately 1.5 kPa. Unfortunately the true noise level was much higher.

### **How well do the mathematical models agree with experimental data?**

Squeeze flow trials with particles, which finished by clamping the particle between the plates in order to show the particle position on the sensor were not able to track the movement of the particle before it touched the plate. The particles were positioned in the outer areas of the sensor. The fluid stress decays towards the edge of the plate, hence, the particle influence is enhanced. Smaller particles show larger fluctuations because they allow the plates to come closer together. Still, the experimental handling of single particles in the  $\mu\text{m}$  range is tedious.

A dimensional analysis (see 4.3.1) was carried out in order to compare the experimental set-up to common in-mouth conditions. In both cases the dimensionless number  $\text{EuRe}$  was in the range of  $10^{-4}$ . Hence, the experimental set-up is a reasonable approach in order to understand in-mouth processing, and the hypothesis that grittiness is sensed through stress field fluctuations possibly confirmed. Due to the high noise threshold of the sensor the experimental set-up did not work. For the future, a more sensitive means to measure the stress field fluctuations could be liquid crystals on top of a glass plate. The stress fluctuations indicated by the crystals need to be filmed with a camera from underneath the glass plate.

Once an experimental set-up works, other aspects such as the particle shape should

be taken into account. Particles in foodstuffs are often not spherical but rather irregular in shape (e.g. sugar crystals). Furthermore the fact that the palate is not a flat plate should be taken into consideration. The plates of the squeeze flow set-up could also be covered with different surfaces.

In the present study the sensation of stress field perturbations were assumed to be responsible for the perception of grittiness. Engelen et al. (2005) in contrast supposes that the particles are rather sensed by the means of friction or vibration. This would give another direction of possible investigation.

After the experimental verification of the theory, an in-vivo study should be conducted. For this, particles have to be incorporated in fluids of viscosities, which are realistic for consumption (e.g. coffee creamer  $10^{-2}$  Pas) and then evaluated by test subjects. Here even particle sizes in the  $\mu\text{m}$  range can be used, which also makes the handling much easier. The sensory study, carried out as a triangle test, has to show that the particles causing perturbations in the theoretical models also lead to a gritty feeling in the mouth.

**The overall goal to keep in mind should be to do accurate measurements of physical food properties and to determine how these relate to the dynamic perception of texture rather than to mimic sensory processes (Foegeding et al., 2003).**

# List of Figures

1.1	Difference between taste and texture in the perception process . . . . .	7
1.2	Long term aim of the project . . . . .	8
2.1	In-mouth processing of disks . . . . .	17
2.2	Distributed load across disks . . . . .	27
2.3	Radius of curvature of the palate . . . . .	27
2.4	Geometric basis for mathematical model . . . . .	28
2.5	Geometrical sketch of the Timoshenko theory . . . . .	30
2.6	Equilibrium on an element of the plate, i.e. internal reaction $M_r$ to external load $Q$ on the element . . . . .	32
2.7	Intervals of possible differentiation . . . . .	38
2.8	Load distribution across a disk . . . . .	39
2.9	Comparison of load profile for disks with different thicknesses but the same diameter . . . . .	40
2.10	Pressure gradients across different disks . . . . .	40
2.11	Thickness detection processes in-mouth . . . . .	45

2.12 Tongue papillae . . . . .	46
2.13 Oral mechanoreceptors . . . . .	47
3.1 Mathematical logical reasoning . . . . .	55
3.2 Coordinate frames overview . . . . .	57
3.3 Squeeze flow scheme . . . . .	58
3.4 Free space graphic illustration . . . . .	72
3.5 Illustration of image and real particle . . . . .	74
3.6 Single particle stress distribution $p$ , free space (contour) . . . . .	78
3.7 Single particle stress distribution $p$ , free space (3D) . . . . .	78
3.8 Single particle stress distribution $\tau_{zz}$ , free space (contour) . . . . .	79
3.9 Single particle stress distribution $\tau_{zz}$ , free space (3D) . . . . .	79
3.10 Single particle stress distribution $p$ , bounded (3D) . . . . .	81
3.11 Single particle stress distribution $p$ versus $\tau_{zz}$ , bounded . . . . .	81
3.12 Superposition of free space curves (particle at middle and edge) . . . . .	84
3.13 $p + \tau_{zz} + P$ (particle and fluid) versus $P$ (fluid), free space . . . . .	85
3.14 Comparison of $p + \tau_{zz}$ for free space and bounded (contour) . . . . .	87
3.15 Comparison of $p$ and $\tau_{zz}$ , bounded . . . . .	88
3.16 $p + \tau_{zz} + P$ (particle and fluid) versus $P$ (fluid), bounded . . . . .	88
3.17 $p + \tau_{zz} + P$ (particle and fluid) versus $P$ (fluid), zoomed, bounded, particle at the edge . . . . .	89

3.18	$p + \tau_{zz} + P$ (particle and fluid) versus $P$ (fluid), zoomed, bounded, particle close to the center . . . . .	89
3.19	Dependence of the disturbance on the particle radius . . . . .	90
3.20	Dependence of the disturbance on the particle position . . . . .	91
3.21	Force relation for different $a/h$ in dependance of $z/h$ . . . . .	92
4.1	Parallel plate set-up . . . . .	95
4.2	Tekscan pressure handle and sensor . . . . .	96
4.3	Overview Tekscan sensor . . . . .	97
4.4	Composition of the Tekscan sensor . . . . .	98
4.5	Bottom plate of the set-up . . . . .	99
4.6	Example of an equilibration file . . . . .	102
4.7	Tekscan frame for equilibrated and calibrated measurement . . . . .	104
4.8	Example of a Tekscan time frame . . . . .	105
4.9	Illustration of the maximum frame in the Tekscan film . . . . .	107
4.10	Unequilibrated and calibrated squeeze flow (trial 0) . . . . .	117
4.11	Equilibration effect of trial 1 to 2 . . . . .	117
4.12	Effect of sensitivity setting of the sensor . . . . .	119
4.13	Pressure profile of uncalibrated squeeze flow (MATLAB) . . . . .	120
4.14	Pressure profile of squeeze flow calibrated with MATLAB . . . . .	120
4.15	Repeatability of non-calibrated trials (no. 6) . . . . .	121

4.16	Repeatability of 3/3 calibrated trials (no. 7) . . . . .	122
4.17	Repeatability of 3/3 calibrated trials (no. 7), Excel . . . . .	123
4.18	Pressure sensor 345 kPa . . . . .	124
4.19	Particle layout on the sensor . . . . .	124
4.20	Squeeze flow with particle (non-equilibrated) . . . . .	125
4.21	Squeeze flow with particle (equilibrated) . . . . .	126
4.22	Squeeze flow with particle (non-equilibrated), 300 Pas . . . . .	127
4.23	Squeeze flow trials according to Yates et al. (2001) . . . . .	127

# List of Tables

2.1	Pretrial disk overview . . . . .	18
2.2	Main study disk overview . . . . .	19
2.3	Overview of all trial series . . . . .	22
2.4	Samples for constant thickness trials . . . . .	23
2.5	Samples for constant diameter trials . . . . .	23
2.6	Samples for finger-palm trials . . . . .	24
2.7	Diameter differences . . . . .	35
2.8	Thickness differences . . . . .	35
2.9	Results of finger-palm trial . . . . .	36
2.10	Results leading to a discrimination threshold of $25 \mu\text{m}$ . . . . .	37
2.11	Theoretical pressures in the disk middle . . . . .	41
2.12	Results indicating existence of an insecure interval . . . . .	41
2.13	Testing of different materials for the pair $150$ versus $180 \mu\text{m}$ . . . . .	42
2.14	Mechanoreceptor classification . . . . .	48

3.1	Parameters for force determination (current work vs. literature) . . . . .	68
3.2	Forces and force ratios (current work vs. literature) . . . . .	69
4.1	Overview of possible equilibration and calibration . . . . .	101
4.2	Overview of used equilibration and calibration . . . . .	111
4.3	Overview of squeeze flow trials . . . . .	112
4.4	Dimensions for the dimensional analysis 1 . . . . .	114
4.5	Dimensions for the dimensional analysis 2 . . . . .	114
B.1	MATLAB column explanation . . . . .	154
C.1	FEP characteristics . . . . .	169
C.2	APET characteristics . . . . .	170
C.3	Whey protein-glycerol film characteristics . . . . .	170

# Appendix A

## Mathematica code for the fluid mechanical model

In the following the Mathematica code (written in Mathematica 5.0) used in chapter 3 is listed. This code was used in order to determine the pressure profile for pure squeeze flow (Stefan), but also to determine the point force (Faxen), which was incorporated in the fluid (Green) and the resulting stress field and velocity field disturbances. Graphs were plotted in order to compare this data, which was finally used to set the parameters for the experimental validation.

# Particles in Fluids

Julia and Adam

---

## Introduction

Use of the single particle singularity functions from Blake et al to calculate the pressure distribution due to the presence of a particle in a squeeze flow between plates. The following two definitions are needed to avoid automatic replacement with later definitions. Saves from restarting the kernel every time the file is run.

```

Clear[r]
Clear[R]

Remove[ShowLegend]

Needs["Graphics`Legend`"]

```

---

## Newtonian Fluid between parallel moving plates

Stefan equation for flow between a pair of parallel plates at a distance  $2h$  apart. Cylindrical polar coordinates  $(r, z)$  with  $\theta$  symmetry) with  $z=0$  at the line of symmetry between the two plates.

```

stefanvelocity = ustefan →
  Function[{r, z, t}, {1 / (2 η) (D[pstefan[r, z, Rp, t], r]) (z^2 - h^2), -D[h[t], t]}]
stefanpressure = pstefan → Function[{r, z, Rp, t},
  3 η D[h[t], t] / (4 h[t]^3) (r^2 - Rp^2)]

ustefan[r, z, t] /. stefanvelocity
% /. stefanpressure

```

---

## Faxen's First Law

Calculates the effective force experienced by a particle in a fluid based on the undisturbed (i.e. no particle in the fluid) velocity and pressure fields.

```

Faxen = F → Function[{uparticle, ustefan},
  6 π η a (ustefan[r, z, t] - uparticle[r, z, t]) + η π a^3 Δ[ustefan[r, z, t]]

```

Because it is a low Re flow, the Stokes equation  $\nabla p = \eta \Delta u$  can be used to directly replace the Laplacian  $\eta \Delta u$  of the velocity field by the pressure gradient  $\nabla p$ .

```

Evaluate[(F[uparticle, ustefan] /. Faxen) /.
  Δ → Function[{u}, 1/η grad[pstefan[r, z, Rp, t]]]]
operator = grad → Function[{x}, {D[x, r], D[x, z]}]
Faxen2 = F → Function[{uparticle, ustefan, pstefan}, Evaluate[%]]

(F[uparticle, ustefan, pstefan, {r, z, Rp, t}] /. Faxen2);
% /. operator;
Faxen3 = F → Function[{uparticle, ustefan, pstefan}, Evaluate[%]]

(F[uparticle, uparticle, pstefan] /. Faxen3)
particleforce = Fp → Evaluate[% /. stefanpressure]

```

Which is the force experienced by a particle in the Stefan flow between the parallel plates. N.B. only the pressure gradient matters since the shear part vanishes because the particle convects at the same speed as the fluid. The force on the particle thus depends only on  $r$  and the instantaneous position and velocity of the plates.

We also create another function that works in coordinates fixed at the bottom of the plate for use at the end.  $pv$  is velocity of the plates,  $halfgap=h[t]$  which is half the plate separation at time  $t$

```

xforce = Fx → Function[{xp, a, pv, μ, halfgap},
  Evaluate[(Fp /. particleforce)[[1]]] /. {r → xp, h[t] → halfgap, h'[t] → pv, η → μ}]

```

---

## Particle in a fluid close to a boundary

This is a particle in a fluid close to a planar boundary with no slip at the boundary. The coordinate system has its origin at the particle centre. There are results for the pressure and the velocity field available in Blake and Chwang 1973, which will allow the calculation of the stress. The pressure field will contribute directly, but the velocity field will contribute through the deviatoric part of the stress tensor. i.e. the differential of the velocity field will also contribute to the stress tensor. For the moment the velocity field contribution will be ignored and the focus will just be on the pressure part.

OseenBlake is the complementary vector for the scalar product with force vector

$len[r_j]$  is the length of the vector  $r_j$  from the centre of the particle

The stationary boundary is the plane of  $z=0$ , with the origin at the centre of the plates (i.e.  $r=0$  for the Stefan equation - don't confuse with  $r$  below which is something else!).

$x$  is the vector from the origin to the sample point

$r$  is vector from the sample point  $x$  to the position of the real particle

$R$  is vector from the sample point  $x$  to the position of the image particle

CAREFUL - THIS IS IN CARTESIAN COORDINATES SO ALL 3 X,Y,Z DIRECTIONS are needed

```

particlepressure = ppart → Function[{F}, Dot[F / (4 π), OseenBlake[r, R, x]]]
distance = len → Function[{x}, (Dot[x, x])^(1/2)]
OBvector = OB → Function[{r, R, x}, r / len[r]^3 - R / len[R]^3]
OBtensbit = tens → Function[{x}, -2 x[[3]] {{1, 0, 0}, {0, 1, 0}, {0, 0, -2}}]
lastbit =
  lastvec → Function[{R}, {D[R[[3]], x], D[R[[3]], y], D[R[[3]], z]} / len[R]^3 -
    3 R[[3]] / len[R]^5 Dot[{{D[R[[1]], x], D[R[[1]], y], D[R[[1]], z]},
      {D[R[[2]], x], D[R[[2]], y], D[R[[2]], z]},
      {D[R[[3]], x], D[R[[3]], y], D[R[[3]], z]}}, {R[[1]], R[[2]], R[[3]]}]
OBtensor = OseenBlake → Function[{r, R, x}, OB[r, R, x] - Dot[tens[x], lastvec[R]]]

```

Note that lastvec simplifies considerably

```
Clear[R]; Clear[r];
lastbit = lastvec →
  Function[{R}, {0, 0, 1} / len[R]^3 - 3 R[[3]] {R[[1]], R[[2]], R[[3]]} / len[R]^5]
```

Combining all terms together leads to the pressure function

```
Off[Part::partd];
OB[{r[[1]], r[[2]], r[[3]]}, {R[[1]], R[[2]], R[[3]]}, {x, y, z}] /. OBvector
Dot[tens[{0, 0, r[[3]]}], lastvec[{R[[1]], R[[2]], R[[3]]}]] /. lastbit /. OBtensbit
OBtensor = OseenBlake → Function[{r, R, x}, Evaluate[% - %]]
OseenBlake[r, R, {x, y, z}] /. OBtensor;
particlepressure =
  ppart → Function[{r, R, F}, Evaluate[Dot[{F[[1]], F[[2]], F[[3]]} / (4 π), %]]]

blakestress = blaketauzz →
  Function[{x, y, z, px, py, pz, imx, imy, imz, h, F1}, Evaluate[2 μ %[[2]]]]
```

for comparison the same procedure is carried out just for a single particle (Blake Chwang p. 24, equation 2)...BEWARE F is a vector here!!!

```
singleparticlepressure = sppart → Function[{fx, x, y, z},
  Evaluate[Dot[{fx, 0, 0} / (4 π), r / len[r]^3 /. r → {x, y, z} /. distance]]]
```

## ■ Test for a particle which is above the origin

Choose the r axis to be aligned with the x axis so that the force is only in the x direction.

```
ppart[{-x, -y, h - z}, {-x, -y, -h - z}, {fx, 0, 0}] /. particlepressure
```

Tells the pressure anywhere in x, y, z (the coordinate system is fixed to the center of the bottom plate)

Now the effect of the particle on the boundary plane at z=0 will be calculated.

The force in the equation is the force Fp from Faxen's law

If the force is set equal to one and z is left as it is: the pressure anywhere is

If z=0--> pressure 0

```
ppart[{-x, -y, h - z}, {-x, -y, -h - z}, {1, 0, 0}] /. particlepressure
```

```
ppart[{-x, -y, h}, {-x, -y, -h}, {1, 0, 0}] /. particlepressure
```

Now the comparison for a single particle: Here (x, y, z) has it's origin at the center of a particle (not the plates). But the position of the particle is (0,0,a) in the plate based coordinate system is such that the pressure field in plate coordinates comes from

```
sppart[fx, x, y, z - a] /. singleparticlepressure
```

Hence there is a pressure disturbance around the particle, which is positive upstream and negative downstream of the particle motion. Since the plate is at z=0 the function describing the pressure field on a plate is

```
platefield = sppressfield →
  Function[{fx, x, y, a}, Evaluate[sppart[fx, x, y, a] /. singleparticlepressure]]
```

```
sppressfield[1.8*10^-6, x, y, 2.10^-4] /. platefield
Max[Table[sppressfield[1.8*10^-6, x, y, 2.10^-4] /. platefield,
  {x, -0.05, 0.05, 0.001}, {y, -0.05, 0.05, 0.001}]]
legndB = Table[{Graphics[{GrayLevel[1 - i], Rectangle[{0, 0}, {1, 1}]}], StringForm[
  "`", PaddedForm[ScientificForm[-2 (%) (i - 0.5)], {2, 3}]}], {i, 0, 1, .1}]
ShowLegend[ContourPlot[sppressfield[1.8*10^-6, x, y, 2.10^-4] /. platefield,
  {x, -0.05, 0.05}, {y, -0.05, 0.05}, TextStyle -> {FontSize -> 14}],
  {legndB, LegendLabel -> "p [Pa]", LegendPosition -> {1.2, -0.6},
  TextStyle -> {FontSize -> 14}, LegendSize -> {1.1, 1.5}}]
```

Tested for real values:

```
Plot3D[-sppressfield[1.8*10^-6, x, y, 2.10^-4] /. platefield,
  {x, -0.001, 0.001}, {y, -0.001, 0.001}, AxesLabel -> {x[m], y[m], p[Pa]},
  PlotRange -> All, TextStyle -> {FontSize -> 17}, PlotPoints -> {100, 100}]
```

It has to be determined, where the particle is in the Stefan flow system:

what is x, y, z in particle based coordinates is (0,0,a) (a is what used to be h but could be confused with h (=plate distance in Stefan), therefore renamed "a")

in plate based coordinates, this makes it (0,0,a-z) in cylindrical polar coordinates of the Stefan situation, calculate the velocity at this point for Stefan. h is what is referred to as "d" in the mathematical chapter.

Since the pressure equation at a sample point resulted in zero pressure the velocity gradient has to be looked at..

For this only the first part (representing a particle in an infinite fluid) of the equation will be taken.

Now the previously mentioned contribution of the velocity field to the stress tensor will be investigated in the following

Next steps

- 1)Take the gradient of the velocity:
- 2)Test for a particle which is above the origin

1): free space Green's function:

```
r = {x - px, y - py, z - pz}
R = {x - imx, y - imy, z - imz}
truelength = t1 -> Function[{w}, Sqrt[w[[1]]^2 + w[[2]]^2 + w[[3]]^2]]
uzz = (1 / (8 π μ)) ((r[[1]] F1 / t1[r]^3) - (3 (r[[3]])^2 r[[1]] F1 / t1[r]^5) )
% /. truelength
freespacestress = fstauzz -> Function[{x, y, z, px, py, pz, F1}, Evaluate[2 μ %[[2]] ]]
```

Plot this out for a particle above the origin and an arbitrary force of 1 (This is in the plane of xy - i.e the bottom plate)

```
Max[Table[fstauzz[x, y, 0, 0, 0, 2*10^-4, 1.8*10^-6] /. freespacestress,
  {x, -0.05, 0.05, 0.001}, {y, -0.05, 0.05, 0.001}]]
legndB = Table[{Graphics[{GrayLevel[1 - i], Rectangle[{0, 0}, {1, 1}]}], StringForm[
  "`", PaddedForm[ScientificForm[-2 (%) (i - 0.5)], {2, 3}]}], {i, 0, 1, .1}]
ShowLegend[ContourPlot[fstauzz[x, y, 0, 0, 0, 2*10^-4, 1.8*10^-6] /.
  freespacestress, {x, -0.05, 0.05}, {y, -0.05, 0.05}, TextStyle -> {FontSize -> 14}],
  {legndB, LegendLabel -> "τzz[Pa]", LegendPosition -> {1.2, -0.6},
  TextStyle -> {FontSize -> 14}, LegendSize -> {1.1, 1.5}}]
```

```
Plot3D[fstauzz[x, y, 0, 0, 0, 2*10^-4, 1.8*10^-6] /. freespacestress,
  {x, -0.001, 0.001}, {y, -0.001, 0.001}, AxesLabel -> {x[m], y[m],  $\tau_{zz}$ [Pa]},
  PlotRange -> All, TextStyle -> {FontSize -> 17}, PlotPoints -> {100, 100}]
```

Now the same thing for the Blake (bounded version)

```
r = {x - px, y - py, z - pz}
R = {x - imx, y - imy, z - imz}
F = {Fx, 0, 0}
truelength = t1 -> Function[{w}, Sqrt[w[[1]]^2 + w[[2]]^2 + w[[3]]^2]]
uzzblake =
  (1 / (8  $\pi$   $\mu$ )) (r[[1]] F1 / t1[r]^3 - R[[1]] F1 / t1[R]^3 - 3 r[[3]]^2 r[[1]] F1 / t1[r]^5 +
    3 R[[3]]^2 R[[1]] F1 / t1[R]^5 - 6 h^2 R[[1]] F1 / t1[R]^5 - 30 h R[[3]]^2 R[[1]]
    F1 / t1[R]^7 - 6 h R[[3]] F1 R[[1]] / t1[R]^5 - 18 h R[[3]] F1 R[[1]] / t1[R]^5)
  % /. truelength /. {imx -> px, imy -> py, imz -> -pz} /. h -> pz /. F1 -> Fx
blakestress = blaketauzz -> Function[{x, y, z, px, py, pz, Fx}, Evaluate[2  $\mu$  %[[2]] ]]
```

Plotted out for a particle above the origin (This is in the plane of xy - i.e the bottom plate.)

```
Max[Table[blaketauzz[x, y, 0, 0, 0, 2*10^-4, 1.8*10^-6] /. blakestress,
  {x, -0.05, 0.05, 0.001}, {y, -0.05, 0.05, 0.001}]]
legndB = Table[{Graphics[{GrayLevel[1 - i], Rectangle[{0, 0}, {1, 1}]}], StringForm[
  "``", PaddedForm[ScientificForm[-2 (%) (i - 0.5)], {2, 3}]}], {i, 0, 1, .1}]
ShowLegend[ContourPlot[blaketauzz[x, y, 0, 0, 0, 2*10^-4, 1.8*10^-6] /. blakestress,
  {x, -0.05, 0.05}, {y, -0.05, 0.05}, TextStyle -> {FontSize -> 14}],
  {legndB, LegendPosition -> {1.2, -0.7}, LegendLabel -> " $\tau_{zz}$ [Pa]",
  TextStyle -> {FontSize -> 14}, LegendSize -> {1.2, 1.8}}]

Plot3D[blaketauzz[x, y, 0, 0, 0, 2*10^-4, 1.8*10^-6] /. blakestress,
  {x, -0.001, 0.001}, {y, -0.001, 0.001}, AxesLabel -> {x[m], y[m],  $\tau_{zz}$ [Pa]},
  PlotRange -> All, TextStyle -> {FontSize -> 17}, PlotPoints -> {100, 100}]
```

Total stress due to a single particle is the sum of (-) the pressure (negative foresign due to sign convention) and the normal stress component.

First step: single particle free space version

Creation of a new pressure function which works in terms of the plate coordinate system, so as to be compatible with the normal stress function.

```
spartpressfull = sppress -> Function[{x, y, z, px, py, pz, Fx},
  Evaluate[sppart[Fx, x - px, y - py, z - pz] /. singleparticlepressure]]

Max[Table[-(sppress[x, y, 0, 0, 0, 2*10^-4, 9*10^-5] /. spartpressfull) +
  (fstauzz[x, y, 0, 0, 0, 2*10^-4, 9*10^-5] /. freespacestress),
  {x, -0.05, 0.05, 0.001}, {y, -0.05, 0.05, 0.001}]]
legndB = Table[{Graphics[{GrayLevel[1 - i], Rectangle[{0, 0}, {1, 1}]}], StringForm[
  "``", PaddedForm[ScientificForm[-2 (%) (i - 0.5)], {2, 3}]}], {i, 0, 1, .1}]
ShowLegend[ContourPlot[
  -(sppress[x, y, 0, 0, 0, 2*10^-4, 9*10^-5] /. spartpressfull) +
  (fstauzz[x, y, 0, 0, 0, 2*10^-4, 9*10^-5] /. freespacestress),
  {x, -0.05, 0.05}, {y, -0.05, 0.05}, TextStyle -> {FontSize -> 14}],
  {legndB, LegendPosition -> {1.2, -0.65}, TextStyle -> {FontSize -> 14},
  LegendLabel -> "p+ $\tau_{zz}$ [Pa]", LegendSize -> {1.0, 1.6}}]
```

```

Plot3D[-(sppress[x, y, 0, 0, 0, 2*10^-4, 9*10^-5] /. spartpressfull) +
  (fstauzz[x, y, 0, 0, 0, 2*10^-4, 9*10^-5] /. freespacestress),
{x, -0.001, 0.001}, {y, -0.001, 0.001}, AxesLabel -> {x[m], y[m], p +  $\tau_{zz}$  [Pa]},
TextStyle -> {FontSize -> 14}, PlotRange -> All, PlotPoints -> {100, 100}]

Plot[{- (sppress[x, 0, 0, 0, 0, 2*10^-4, 1.8*10^-6] /. spartpressfull),
  (fstauzz[x, 0, 0, 0, 0, 2*10^-4, 1.8*10^-6] /. freespacestress)},
{x, -0.005, 0.005}, AxesLabel -> {x[m], stress [Pa]}, PlotRange -> All,
TextStyle -> {FontSize -> 14}, PlotPoints -> 500, PlotLegend -> {"p", " $\tau_{zz}$ "},
LegendPosition -> {0.40, 0.2}, LegendSize -> {0.4, 0.4}, LegendShadow -> None,
PlotStyle -> {{AbsoluteThickness[3], Dashing[{0.03, 0.02}], RGBColor[1, 0, 0]},
  {AbsoluteThickness[3], RGBColor[0, 1, 0]}}]

```

Now for the bounded version:

```

ppart[r, R, F] /. particlepressure /. distance

blakepressfull = blakepress -> Function[{x, y, z, px, py, pz, Fx}, Evaluate[
  ppart[r, R, F] /. particlepressure /. distance /. {imx -> px, imy -> py, imz -> -pz}]]

N[blakepress[x, y, 0, 0, 0, 1, 1] /. blakepressfull]

blaketauzz[x, y, z, px, py, pz, Fx] /. blakestress
Simplify[blaketauzz[x, y, 0, 0, 0, 1, 1] /. blakestress]

Max[Table[-(blakepress[x, y, 0, 0, 0, 2*10^-4, 9*10^-5] /. blakepressfull) +
  (blaketauzz[x, y, 0, 0, 0, 2*10^-4, 9*10^-5] /. blakestress),
{x, -0.05, 0.05, 0.001}, {y, -0.05, 0.05, 0.001}]]

legndB = Table[{Graphics[{GrayLevel[1 - i], Rectangle[{0, 0}, {1, 1}]}], StringForm[
  "`", PaddedForm[ScientificForm[-2 (%) (i - 0.5)], {2, 3}]}], {i, 0, 1, .1}]

ShowLegend[ContourPlot[-(blakepress[x, y, 0, 0, 0, 2*10^-4, 9*10^-5] /.
  blakepressfull) + (blaketauzz[x, y, 0, 0, 0, 2*10^-4, 9*10^-5] /. blakestress),
{x, -0.05, 0.05}, {y, -0.05, 0.05}, TextStyle -> {FontSize -> 14}],
{legndB, LegendPosition -> {1.2, -0.68}, LegendLabel -> "p +  $\tau_{zz}$  [Pa]",
  TextStyle -> {FontSize -> 14}, LegendSize -> {1.0, 1.6}]]

Plot3D[-(blakepress[x, y, 0, 0, 0, 2*10^-4, 9*10^-5] /. blakepressfull) +
  (blaketauzz[x, y, 0, 0, 0, 2*10^-4, 9*10^-5] /. blakestress),
{x, -0.001, 0.001}, {y, -0.001, 0.001}, AxesLabel -> {x[m], y[m], p +  $\tau_{zz}$  [Pa]},
TextStyle -> {FontSize -> 14}, PlotRange -> All, PlotPoints -> {100, 100}]

Plot[{- (blakepress[x, 0, 0, 0, 0, 2*10^-4, 1.8*10^-6] /. blakepressfull),
  (blaketauzz[x, 0, 0, 0, 0, 2*10^-4, 1.8*10^-6] /. blakestress)},
{x, -0.005, 0.005}, PlotPoints -> 500, AxesLabel -> {x[m], stress [Pa]},
PlotRange -> All, TextStyle -> {FontSize -> 14}, PlotLegend -> {"p", " $\tau_{zz}$ "},
LegendPosition -> {0.40, 0.2}, LegendSize -> {0.4, 0.4}, LegendShadow -> None,
PlotStyle -> {{AbsoluteThickness[3], Dashing[{0.03, 0.02}], RGBColor[1, 0, 0]},
  {AbsoluteThickness[3], RGBColor[0, 1, 0]}}]

```

In the above equations  $F_x$  from Faxen's law needed to be calculated for the position of the particle and substituted into the last bit.

This is the free particle.

The force acting on the particle is

```
Fx[x, a, pv,  $\mu$ , halfgap] /. xforce
```

The pressure between the plates due to the unperturbed fluid (Stefan equation) is (Rp is the radius of the plates)

```
pstefan[x, z, Rp, t] /. stefanpressure
fluidpressure = fluidP  $\rightarrow$ 
  Function[{x, Rp, pv,  $\mu$ , halfgap}, Evaluate[% /. h'[t]  $\rightarrow$  pv /. h[t]  $\rightarrow$  halfgap /.  $\eta \rightarrow \mu$ ]]

Max[Table[-(sppress[x, y, 0, 0.0049, 0, 2*10^-4, 9*10^-5] /. spartpressfull) +
  (fstauzz[x, y, 0, 0.01, 0, 0.01,
    (Fx[0.049, 10^-4, -.0001, 30, 2*10^-4] /. xforce) /. freespacestress),
  {x, -0.05, 0.05, 0.001}, {y, -0.05, 0.05, 0.001}]]

legndB = Table[{Graphics[{GrayLevel[1 - i], Rectangle[{0, 0}, {1, 1}]}], StringForm[
  "`", PaddedForm[ScientificForm[-2 (%) (i - 0.5)], {2, 3}]}], {i, 0, 1, .1}]
ShowLegend[ContourPlot[-(sppress[x, y, 0, 0.0049, 0, 2*10^-4, 9*10^-5] /.
  spartpressfull) + (fstauzz[x, y, 0, 0.01, 0, 0.01,
    (Fx[0.049, 2*10^-4, -.0001, 30, 2*10^-4] /. xforce) /. freespacestress),
  {x, -0.05, 0.05}, {y, -0.05, 0.05}], {legndB, LegendPosition  $\rightarrow$  {1.2, -0.4},
  LegendSize  $\rightarrow$  {1.20, 1.5}}]

Plot3D[-(sppress[x, y, 0, 0.049, 0.049, 2*10^-4, 9*10^-5] /. spartpressfull) +
  (fstauzz[x, y, 0, 0.01, 0, 0.01,
    (Fx[0.049, 10^-4, -.0001, 30, 2*10^-4] /. xforce) /. freespacestress),
  {x, 0.048, 0.05}, {y, 0.048, 0.05}, TextStyle  $\rightarrow$  {FontSize  $\rightarrow$  14},
  AxesLabel  $\rightarrow$  {x[m], y[m], p +  $\tau_{zz}$ [Pa]},
  PlotPoints  $\rightarrow$  {100, 100}, PlotRange  $\rightarrow$  All]

Plot[[-(sppress[x, 0, 0, 0.049, 0, 2*10^-4,
  (Fx[0.049, 10^-4, -.0001, 30, 2*10^-4] /. xforce) /. spartpressfull),
  (fstauzz[x, 0, 0, 0.049, 0, 2*10^-4,
    (Fx[0.049, 10^-4, -.0001, 30, 2*10^-4] /. xforce) /. freespacestress),
  -(sppress[x, 0, 0, 0.049, 0, 2*10^-4, (Fx[0.049, 10^-4, -.0001, 30, 2*10^-4] /.
    xforce) /. spartpressfull) + (fstauzz[x, 0, 0, 0.049, 0, 2*10^-4,
    (Fx[0.049, 10^-4, -.0001, 30, 2*10^-4] /. xforce) /. freespacestress)},
  {x, 0.045, 0.055}, PlotRange  $\rightarrow$  All, TextStyle  $\rightarrow$  {FontSize  $\rightarrow$  14},
  AxesLabel  $\rightarrow$  {x[m], stress[Pa]},
  PlotLegend  $\rightarrow$  {"p", " $\tau_{zz}$ ", "p +  $\tau_{zz}$ "},
  LegendPosition  $\rightarrow$  {0.40, 0.2},
  LegendSize  $\rightarrow$  {0.4, 0.4},
  LegendShadow  $\rightarrow$  None,
  PlotStyle  $\rightarrow$  {{AbsoluteThickness [3], Dashing[{0.01, 0.01}], RGBColor[1, 0, 0]},
    {AbsoluteThickness [3], Dashing[{0.03, 0.02}], RGBColor[0, 1, 0]},
    {AbsoluteThickness [3], RGBColor[0, 0, 1]}}
```

```

Plot[{- (sppress[x, 0, 0, 0.049, 0, 2*10^-4,
      (Fx[0.049, 10^-4, -.0001, 30, 2*10^-4] /. xforce) /. spartpressfull) +
      (fstauzz[x, 0, 0, 0.049, 0, 2*10^-4, (Fx[0.049, 10^-4, -.0001, 30, 2*10^-4] /.
      xforce) /. freespacestress) +
      fluidP[x, 0.05, -0.0001, 30, 2*10^-4] /. fluidpressure,
      fluidP[x, 0.05, -0.0001, 30, 2*10^-4] /. fluidpressure},
{x, -0.05, 0.05}, AxesLabel -> {x[m], stress[Pa]},
PlotRange -> All,
PlotLegend -> {"p+τzz+P", "P"},
LegendPosition -> {0.60, -0.2},
LegendSize -> {0.6, 0.4},
LegendShadow -> None,
TextStyle -> {FontSize -> 14},
PlotStyle -> {{AbsoluteThickness [3], Dashing[{0.03, 0.02}], RGBColor[1, 0, 0]},
{AbsoluteThickness [3], RGBColor[0, 0, 1]}}]

Plot[{- (sppress[x, 0, 0, 0.049, 0, 2*10^-4,
      (Fx[0.049, 10^-4, -.0001, 30, 2*10^-4] /. xforce) /. spartpressfull) +
      (fstauzz[x, 0, 0, 0.049, 0, 2*10^-4, (Fx[0.049, 10^-4, -.0001, 30, 2*10^-4] /.
      xforce) /. freespacestress) +
      fluidP[x, 0.05, -0.0001, 30, 2*10^-4] /. fluidpressure,
      fluidP[x, 0.05, -0.0001, 30, 2*10^-4] /. fluidpressure},
{x, 0.047, 0.05}, AxesLabel -> {x[m], P[Pa]},
PlotLegend ->
{"p+τzz+P", "P"},
LegendPosition -> {-0.15, 0.2},
LegendSize -> {0.6, 0.4},
LegendShadow -> None,
TextStyle -> {FontSize -> 14},
PlotStyle -> {{AbsoluteThickness [3], Dashing[{0.03, 0.02}], RGBColor[1, 0, 0]},
{AbsoluteThickness [3], RGBColor[0, 0, 1]}}]

```

NB the last graph compares the Stefan solution (blue), without the particle, to the one of the perturbed flow (red).

The graph before shows the influence of the hydrostatic pressure (red), the viscous stress (green), and both together (blue).

Finally the same thing for Blake, i.e. the bounded situation.

```

Max[Table[
  -(blakepress[x, y, 0, 0.049, 0, 2*10^-4, (Fx[0.049, 10^-4, -.0001, 30, 2*10^-4] /.
    xforce) /. blakepressfull) + (blaketauzz[x, y, 0, 0.049, 0, 2*10^-4,
    (Fx[0.049, 10^-4, -.0001, 30, 2*10^-4] /. xforce) /. blakestress),
  {x, -0.01, 0.05, 0.001}, {y, -0.05, 0.05, 0.001}]]
legndB = Table[{Graphics[{GrayLevel[1 - i], Rectangle[{0, 0}, {1, 1}]}], StringForm[
  "`", PaddedForm[ScientificForm[-2 (%) (i - 0.5)], {2, 3}]}], {i, 0, 1, .1}]
ShowLegend[ContourPlot[- (blakepress[x, y, 0, 0.049, 0, 2*10^-4,
  (Fx[0.049, 10^-4, -.0001, 30, 2*10^-4] /. xforce) /. blakepressfull) +
  (blaketauzz[x, y, 0, 0.049, 0, 2*10^-4,
  (Fx[0.049, 10^-4, -.0001, 30, 2*10^-4] /. xforce) /. blakestress),
{x, -0.01, 0.05}, {y, -0.05, 0.05}], {legndB, LegendPosition -> {1.2, -0.4},
LegendLabel -> "p+τzz [Pa]",
TextStyle -> {FontSize -> 14},
LegendSize -> {1.20, 1.5}}]

```

```

Plot3D[-(sppress[x, y, 0, 0.049, 0.049, 2*10^-4, 9*10^-5] /. spartpressfull) +
  (fstauzz[x, y, 0, 0.01, 0, 0.01,
    (Fx[0.049, 10^-4, -.0001, 30, 2*10^-4] /. xforce)] /. freespacestress),
{x, -0.01, 0.01}, {y, -0.01, 0.01}, TextStyle -> {FontSize -> 14},
AxesLabel -> {x[m], y[m], p +  $\tau_{zz}$  [Pa]},
PlotPoints -> {100, 100}, PlotRange -> All]

Plot3D[-(blakepress[x, y, 0, 0.049, 0.049, 2*10^-4,
  (Fx[0.049, 10^-4, -.0001, 30, 2*10^-4] /. xforce)] /. blakepressfull) +
  (blaketauzz[x, y, 0, 0.049, 0, 2*10^-4,
    (Fx[0.049, 10^-4, -.0001, 30, 2*10^-4] /. xforce)] /. blakestress),
{x, 0.048, 0.05}, {y, 0.048, 0.05}, TextStyle -> {FontSize -> 14},
AxesLabel -> {x[m], y[m], stress[Pa]},
PlotRange -> All,
PlotPoints -> {100, 100}]
Display["file.ps", %]

Plot[
  -(blakepress[x, 0, 0, 0.049, 0, 2*10^-4, (Fx[0.049, 10^-4, -.0001, 30, 2*10^-4] /.
    xforce)] /. blakepressfull), (blaketauzz[x, 0, 0, 0.049, 0, 2*10^-4,
    (Fx[0.049, 10^-4, -.0001, 30, 2*10^-4] /. xforce)] /. blakestress),
  -(blakepress[x, 0, 0, 0.049, 0, 2*10^-4, (Fx[0.049, 10^-4, -.0001, 30, 2*10^-4] /.
    xforce)] /. blakepressfull) + (blaketauzz[x, 0, 0, 0.049, 0, 2*10^-4,
    (Fx[0.049, 10^-4, -.0001, 30, 2*10^-4] /. xforce)] /. blakestress)},
{x, 0.046, 0.052}, AxesLabel -> {x[m], stress[Pa]},
PlotRange -> All,
TextStyle -> {FontSize -> 14},
PlotLegend -> {"p", " $\tau_{zz}$ ", "p+ $\tau_{zz}$ "},
LegendPosition -> {0.40, 0.2},
LegendSize -> {0.4, 0.4},
LegendShadow -> None,
PlotStyle -> {{AbsoluteThickness [3], Dashing[{0.04, 0.04}], RGBColor[1, 0, 0]},
  {AbsoluteThickness [4], Dashing[{0.3, 0.02}], RGBColor[0, 1, 0]},
  {AbsoluteThickness [3], RGBColor[0, 0, 1]}}]

Plot[
  -(blakepress[x, 0, 0, 0.049, 0, 2*10^-4, (Fx[0.049, 10^-4, -.0001, 30, 2*10^-4] /.
    xforce)] /. blakepressfull) + (blaketauzz[x, 0, 0, 0.049, 0, 2*10^-4,
    (Fx[0.049, 10^-4, -.0001, 30, 2*10^-4] /. xforce)] /. blakestress) +
  fluidP[x, 0.05, -0.0001, 30, 2*10^-4] /. fluidpressure,
  fluidP[x, 0.05, -0.0001, 30, 2*10^-4] /. fluidpressure},
{x, -0.05, 0.05}, PlotLegend -> {"p+ $\tau_{zz}$ +P", "P"},
LegendPosition -> {0.60, 0.2},
LegendSize -> {0.8, 0.4},
LegendShadow -> None,
AxesLabel -> {x[m], stress[Pa]},
PlotRange -> All,
TextStyle -> {FontSize -> 13},
PlotStyle -> {{AbsoluteThickness [3], Dashing[{0.03, 0.02}], RGBColor[1, 0, 0]},
  {AbsoluteThickness [3], RGBColor[0, 1, 0]}}]

```

Particle close to the middle

```

Plot[
  {-(blakepress[x, 0, 0, 0.001, 0, 2*10^-4, (Fx[0.001, 10^-4, -.0001, 30, 2*10^-4] /.
    xforce) /. blakepressfull) + (blaketauzz[x, 0, 0, 0.001, 0, 2*10^-4,
    (Fx[0.001, 10^-4, -.0001, 30, 2*10^-4] /. xforce) /. blakestress) +
    fluidP[x, 0.05, -0.0001, 30, 2*10^-4] /. fluidpressure,
    fluidP[x, 0.05, -0.0001, 30, 2*10^-4] /. fluidpressure},
  {x, 0.00, 0.01}, PlotLegend -> {"p+ $\tau_{zz}$ +P", "P"},
  LegendPosition -> {0.50, 0.2},
  LegendSize -> {0.44, 0.4},
  LegendShadow -> None,
  AxesLabel -> {x[m], stress[Pa]},
  PlotRange -> All,
  TextStyle -> {FontSize -> 14},
  PlotStyle -> {{AbsoluteThickness [3], Dashing[{0.03, 0.02}], RGBColor[1, 0, 0]},
    {AbsoluteThickness [3], RGBColor[0, 1, 0]}}]

```

### Particle close to the edge

```

Plot[
  {-(blakepress[x, 0, 0, 0.049, 0, 2*10^-4, (Fx[0.049, 10^-4, -.0001, 30, 2*10^-4] /.
    xforce) /. blakepressfull) + (blaketauzz[x, 0, 0, 0.049, 0, 2*10^-4,
    (Fx[0.049, 10^-4, -.0001, 30, 2*10^-4] /. xforce) /. blakestress) +
    fluidP[x, 0.05, -0.0001, 30, 2*10^-4] /. fluidpressure,
    fluidP[x, 0.05, -0.0001, 30, 2*10^-4] /. fluidpressure},
  {x, 0.047, 0.05}, PlotLegend -> {"p+ $\tau_{zz}$ +P", "P"},
  LegendPosition -> {-0.50, 0.2},
  LegendSize -> {0.45, 0.4},
  LegendShadow -> None,
  AxesLabel -> {x[m], stress[Pa]},
  PlotRange -> All,
  TextStyle -> {FontSize -> 14},
  PlotStyle -> {{AbsoluteThickness [3], Dashing[{0.03, 0.02}], RGBColor[1, 0, 0]},
    {AbsoluteThickness [3], RGBColor[0, 1, 0]}}]

```

This graph illustrates the influence of the pressure part (red), the velocity part (green), and both together (blue)

As before, in the last graph blue refers to the unperturbed Stefan flow field, red shows the influence of the particle.

So with the right parameters in the Blake solution one ought to be able to 'see' a particle...

The added pressures for the single particle (free space) & the Blake situation (bounded) are shown in the following:

Free space:

```

Totalfreestress =
  totfree -> Function[{x, y, z, px, py, pz, Fx, Rp, pv,  $\eta$ , d}, Evaluate[Simplify[
    -(spress[x, y, 0, px, py, pz, Fx] /. spartpressfull) + (fstauzz[x, y, z, px, py,
    pz, Fx] /. freespacestress) + fluidP[x, Rp, pv,  $\eta$ , d] /. fluidpressure]]]
Simplify[%]

```

And for the Blake bounded situation:

```
Totalboundedstress =
totbound → Function[{x, y, z, px, py, pz, Fx, Rp, pv, η, d}, Evaluate[Simplify[
- (blakepress[x, y, z, px, py, pz, Fx] /. blakepressfull) + (blaketauzz[x, y, z, px,
py, pz, Fx] /. blakestress) + fluidP[x, Rp, pv, η, d] /. fluidpressure]]]
```

From now on only Blake will be used. The magnitude of p and tau has to be considered as they need to be larger than the noise of the sensor

```
particleinfluence = partinf → Function[{x, y, z, px, py, pz, Fx},
Evaluate[- (blakepress[x, y, z, px, py, pz, Fx] /. blakepressfull) +
(blaketauzz[x, y, z, px, py, pz, Fx] /. blakestress)]]]
```

In the following the pure Stefan profile will be plotted for a 5cm radius disc → 0.05m, plate velocity of 6 mm/min = 0.0001 m/s, viscosity = 30 Pas, and plate distance = 2.5mm = 0.0025m (x, Rp, pv, eta, halfgap), the result is in Pa

```
Plot[{fluidP[x, 0.05, -0.0001, 30, 0.001] /. fluidpressure},
{x, -0.05, 0.05}, AxesLabel → {x, P}, PlotStyle → {Thickness [0.01]}]

Evaluate[fluidP[0, 0.05, -0.0001, 30, 0.001] /. fluidpressure]

Plot[{fluidP[x, 0.05, -0.0001, 30, 0.00153] /. fluidpressure,
fluidP[x, 0.05, -0.0001, 30, 0.001] /. fluidpressure},
{x, -0.05, 0.05}, AxesLabel → {"x [m]", "P [Pa]"}, PlotStyle →
{{Thickness [0.01], RGBColor[1, 0, 0]}, {Thickness [0.01], RGBColor[0, 1, 0]}}]
```

The following function substitutes Faxen's force (dependent of particle position xp, particle radius a, plate velocity pv, viscosity η, and plate distance d) into the sum of Blake pressure and Blake stress

```
particleinfluenceFAXEN =
partinfFAXEN → Function[{x, y, z, px, py, pz, a, pv, η, d}, Evaluate[
- (blakepress[x, y, z, px, py, pz, Fx[x, a, pv, η, d] /. xforce] /. blakepressfull) +
(blaketauzz[x, y, z, px, py, pz, Fx[x, a, pv, η, d] /. xforce] /. blakestress)]]]
```

With a given threshold (given by the sensor sensibility) the partinf function needs to be so that the resulting value is greater than the threshold, i.e. threshold < partinf, the particle radius a for which this is valid with a given viscosity, plate velocity, particle position, plate distance, and sample point x has to be found  
Example for viscosity 30Pas, plate velocity 0.0001 m/s, particle position (1,1,1), plate distance, 0.0012 m, sample point 1

Force is largest on particle as it gets near to the edge of the plate...also F is proportional to the cube of the particle radius

Force is largest for high viscosities (second graph)

```
Plot[Fx[0.03, a, 0.0001, 30, .001] /. xforce,
{a, 0, .001}, AxesLabel → {a, Fx}, PlotStyle → {Thickness [0.01]}]
Plot[Fx[0.03, 0.001, 0.0001, η, .001] /. xforce, {η, 10^-3, 10^3},
AxesLabel → {a, Fx}, PlotStyle → {Thickness [0.01]}]
```

```

partinfFAXEN[0.03, 0, 0, 0.029, 0, a 1.1, a, -0.0001, 30, 2*a] /.
particleinfluenceFAXEN
Newfunc = pfunc → Function[{a}, Evaluate[%]]
Plot[{pfunc[a] /. Newfunc, fluidP[0.03, 0.05, -0.0001, 30, 0.001] /. fluidpressure},
{a, 0.00, 0.01}, AxesLabel → {"a [m]", "stress [Pa]"},
PlotLegend → {"p+ $\tau_{zz}$ +P", "P"}, LegendPosition → {0.40, 0.1},
LegendSize → {0.7, 0.4}, LegendShadow → None, TextStyle → {FontSize → 14},
PlotStyle → {{AbsoluteThickness [3], Dashing[{0.03, 0.02}], RGBColor[1, 0, 0]},
{AbsoluteThickness [3], RGBColor[0, 1, 0]}}]

partinfFAXEN[x, 0, 0, x - 0.0015, 0, a 1.1, a, -0.0001, 30, 2*a] /.
particleinfluenceFAXEN /. a → 0.001
Newfunc = pfunc → Function[{x}, Evaluate[%]]
Plot[{pfunc[x] /. Newfunc, fluidP[x, 0.05, -0.0001, 30, 0.002] /. fluidpressure},
{x, 0.00, 0.05}, AxesLabel → {"x [m]", "stress [Pa]"},
PlotLegend → {"p+ $\tau_{zz}$ +P", "P"}, LegendPosition → {0.50, -0.1},
LegendSize → {0.7, 0.4}, LegendShadow → None, TextStyle → {FontSize → 14},
PlotStyle → {{AbsoluteThickness [3], Dashing[{0.03, 0.02}], RGBColor[1, 0, 0]},
{AbsoluteThickness [3], RGBColor[0, 1, 0]}}]

```

# Appendix B

## MATLAB code for the theoretical equilibration and calibration

The MATLAB code described in the following refers to the MATLAB version no. 7.0.1.

In order to start the MATLAB correction procedure the relevant files have to be loaded. For this the Tekscan file needs to be renamed with the `nametek` command, e.g. `nametek='SQF 2-1.asf'`, and the Zwick file with `namezwick`, e.g. `namezwick='SQF 2-1.xls'`. Afterwards they can be loaded and processed with the following files. The columns the files refer to are listed in Table B.1.

### Tekreadsnocal.m

```
% tekreadnocal.m – script to read a TekScan ASCII file into  
    matlab data  
% structures  
% Adam & Julia , May 2005  
  
% assume the variable name includes the file path  
% e.g. command line such as
```

Table B.1: Contents of the different columns referred to in the MATLAB files

column no.	described value
1	force in N
2	distance covered in mm
3	absolute distance remaining in mm
4	time passed since the beginning of the trial
5	velocity of the upper plate in m/s
6	force calculated with the Stefan equation, see chapter ??
7	true distance calculated with the Stefan equation
8	$\dot{d}/d^3$
9	cumulative integral of column 8

```
% nametek='test.dat'
```

```
%open the Zwick file (excel)
```

```
% assume the variable name includes the file path
```

```
% e.g. command line such as
```

```
% namezwick='test.dat'
```

```
% open the file and read in the header to appropriate  
variables
```

```
file_id = fopen(nametek, 'r');
```

```
% skip first two lines of header
```

```
out=textscan(file_id, '%[^\n]', 1);
```

```
out=textscan(file_id, '%[^\n]', 1);
```

```
% now get the filename on TekScan system
```

```

% more robust this way as ignores spaces in file path
out=textscan(file_id , '%s_%#[^\n]' ,1);
% note that this is a cell array so we need to index it with
    curly brackets
% if we want to see the contents
filename=out{1,2};

% more interesting data from header
% semicolons just stop it echoing to the screen during
    execution
out=textscan(file_id , '%s_%d' ,1);
sensor_model=out{1,2}
out=textscan(file_id , '%s_%d' ,1);
rows=out{1,2}
out=textscan(file_id , '%s_%d' ,1);
cols=out{1,2}
out=textscan(file_id , '%s_%f_%s' ,1);
row_pitch_mm=out{1,2}
out=textscan(file_id , '%s_%f_%s' ,1);
col_pitch_mm=out{1,2}
out=textscan(file_id , '%s_%f_%s' ,1);
sensor_area_mm2=out{1,2}
out=textscan(file_id , '%s_%f' ,1);
noise_threshold=out{1,2}
out=textscan(file_id , '%s_%f' ,1);
frame_time_s=out{1,2}

% skip line
out=textscan(file_id , '%#[^\n]' ,1);

% more data from header

```

```

out=textscan(file_id , '%s_%^[^\\n]' ,1);
when=out{1,2}

% skip 1 line
out=textscan(file_id , '%^[^\\n]' ,1);

% need to set this to a dummy value so that later files don't
  complain
pressure_unit={'RAW' };

% more data from header
out=textscan(file_id , '%s_%d' ,1);
start_frame=out{1,2}
out=textscan(file_id , '%s_%d' ,1);
end_frame=out{1,2}

% skip 4 lines
out=textscan(file_id , '%^[^\\n]' ,1);
out=textscan(file_id , '%^[^\\n]' ,1);
out=textscan(file_id , '%^[^\\n]' ,1);
out=textscan(file_id , '%^[^\\n]' ,1);

% erase any old frame data first
clear frames;

% now we can read the frame data
for frame=start_frame:end_frame

    % read a single frame
    out=textscan(file_id , '%s_%d' ,1);
    frame_num=out{1,2}

```

```

% read one frame into a matrix frame
A=zeros(rows,cols);
for i=1:rows
    temp = fscanf(file_id, '%f, ');
    A(i,:) = temp;
end % single frame loop

% bung each frame in an indexed cell array
frames(frame)={A};
% to read these back as arrays we need to use the command
% A=frames{x}, where x is the frame number (NB curly
    brackets)

end % all frames loop

% remember to close the file again (i.e. clean up)
fclose(file_id);

%open the Zwick file (excel)
% assume the variable name includes the file path
% e.g. command line such as
% namezwick='test.dat'
[zwickvalue, zwickheader]=xlsread(namezwick);

```

## Timepoint.m

```

% timepoint.m - plots a particular point for all times
% Adam & Julia, April 2005

function f=timepoint(frames, row, col)

```

```

% f is the value returned

[cols rows]=size(frames);

for i=1:rows
    f(i,1)=i; % frame number
    f(i,2)=frames{i}(row,col); % value
end

```

## Timebase.m

```

% timebase.m- function to find start and end of curves.
% Adam & Julia , May 2005

% set a threshold value as 10% of the average value then count
% from each
% end to find start and finish of curve...

function f=timebase(curve , thresh)
% curve is a (:,2) column vector of x and y data for the curve
% threshold of average value in %

largest=max(curve(:,2)); % average y value
thresh=thresh*largest/100; % threshold value

[row , col]=size(curve);
start=0;
starti=-1;
finishi=-1;
mx=1;

```

```

finish=0;

% loop through all the points in the curve
for i=1:row
    if ((curve(i,2)>thresh)&(start==0)) start=curve(i,1);
        starti=i;
    end
    if ((curve(i,2)>thresh)) finish=curve(i,1); finishi=i;
    end
    if ((curve(i,2)>curve(mx,2))) mx=i;
    end
end

% add the maximum value as well
f=[start , curve(mx,1) , finish , starti ,mx, finishi ];

```

## Synchronise.m

```

% synchronise.m- function to set a common time frame for the
% Zwick and the
% Tekscan data
% Adam & Julia May, 2005

% create a vector of velocity vs time from Zwick data
% and find start and end of curve
temp=[zwickvalue(:,4) zwickvalue(:,5) ];
c = timebase(temp,10);
zendtime=c(3)

% now do the same thing for the tekscan data
% take a random point

```

```

% may not be robust if this point is not stable , so better to
    take a few and use
% the average , but do this later...
temp = 1/4*(timepoint(frames,26,25)+timepoint(frames,10,10)+
    timepoint(frames,30,10)+timepoint(frames,10,30));
c = timebase(temp,10);
tekindtime=c(3)

% calculate the offset between zwick end time (when the
    velocity stops)
% and tekscan end time (when the velocity stops)
offset = tekindtime - zendtime

% adjust all of the zwick times to the tekscan time frame
zwickvalue(:,4) = zwickvalue(:,4) + offset;

```

## Zwickforce.m

```

% zwickforce.m- script to check the consistency of Zwick data
% Adam & Julia , May 2005

% column 5 is velocity (m/s)
% column 6 is force (kg.m/s^2) from Stefan equation (with no
% mouse mat cols 6 and 1 should be identical)
% column 7 is true distance back calculated from Stefan
    equation
% column 8 is hdot/h^3
% column 9 is the cumalulative integral of col 8

[row col]=size(zwickvalue);
for i=1:row-1

```

```

    temp=zwickvalue(i+1, :)-zwickvalue(i, :);
    vel(i)=-1e-3.*temp(3)./temp(4);
end

vel=vel';
% add last velocity so size matches zwickvalue
vel(row)=0;
zwickvalue(:,5) = vel;

%calculate the force with Stefan equation
constant1= 3*30*3.14*0.05^4/2;
zwickvalue(:,6)=constant1*(zwickvalue(:,5)./(1e-3 *(zwickvalue
    (:,3))).^3); % 1/(m^2.s)

% calculate the 'true h' assuming F is correctly measured by
    Zwick (in mm)
zwickvalue(:,7)=1000*(constant1*zwickvalue(:,5) ./ zwickvalue
    (:,1)).^(1/3);
% this is wrong for the first few point because the velocity
    is zero, so we
% need to patch it up
temp=[zwickvalue(:,4) zwickvalue(:,5)];
c = timebase(temp,10);
vstart=c(4); % number of first point with non zero velocity
zwickvalue(1:vstart,7) = zwickvalue(vstart+1,7);
vend=c(6); % number of last point with non zero velocity
zwickvalue(vend:row,7) = zwickvalue(vend-1,7);

% calculate hdot/h^3
zwickvalue(:,8) = real((zwickvalue(:,5))./(zwickvalue(:,7).*1
    e-3).^3);

```

```

% calculate the cumulative numerical integral of hdot/h^3 dt
[row, col]=size(zwickvalue);
dt = (zwickvalue(row,4)-zwickvalue(1,4))/row;
zwickvalue(:,9) = cumtrapz(zwickvalue(:,8));
% cumtraz assumes dt=1 so multiply all by dt
zwickvalue(:,9) = zwickvalue(:,9)*dt;

```

## Tekcorrection.m

```

% tekcorrection.m- function to do a pointwise automatic
    calibration of the
% Tekscan data to compensate for differing sensitivity between
    points
% Adam & Julia , May 2005

% 3 steps to success...
% (1) check what the tekscan sensor thinks it measures
% (2) compare with the zwick data (which we believe) and
    calculate the
% true gain from the difference (i.e. Zwick value/ tekscan
    value
% (3) Build a matrix of values for all of the tekscan sensor (
    measuring
% point)
% (4) multiply all of the tekscan frame data by the corrected
    gain matrix from (3)

% sorry that was 4 points...

% physical data

```

```

nu = 30; % dynamic viscosity Pa.s
R = 50e-3; % plate radius m

thresh = 50; % threshold value for curve start end etc

zwickforce; % calculate the zwick derived data
synchronise; % ensure that timebases are common between the
    datasets

% clear out any old data
clear ('cal');
clear ('offset');

% loop through all the sensors
for x=1:double(rows)
    for y=1:double(cols)

        % step (1)
        % what is the radius of the sensor
        r = sqrt(((double(rows)/2.-x)*row_pitch_mm)^2 + ((
            double(cols)/2.-y)*col_pitch_mm)^2);
        r = r./1000; % convert to m
        % extract the stress time curve for the point (x,y)
            from the Tekscan data
        tekpointdat=timepoint(frames,x,y);
        % convert PSI to Pa if required for tekscan yankee
            units
        if(strcmp(pressure_unit{1}, 'PSI'))
            tekpointdat(:,2) = tekpointdat(:,2).*(1e+5)./14.5;
            %to Pa
        end
    end
end

```

```

% be careful as some sensors have a permanent offset
% we assume that all sensors have an offset and that
    the value of
% the stress for the first and last few points is zero
[ro ,co]=size(tekpointdat);
[roz ,coz]=size(zwickvalue);
offset(x,y) = -(1/5)*(sum(tekpointdat(1:3,2))+sum(
    tekpointdat(ro-1:ro,2)));

% patch up tekpointdat for rest of this calculation
tekpointdat(:,2) = tekpointdat(:,2) + offset(x,y);

% find the start end and max values of this curve
% and take the mean between the start end end points (
    above the threshold)
% don't use mean function as time bases could be
    different
tekcurvestat=timebase(tekpointdat ,thresh);

% check that the sensor actually works at point (x,y)
if(( tekcurvestat(4) >0.0)&(tekcurvestat(3)-tekcurvestat
    (1) >0.0))

    tekmeanstress=sum(tekpointdat(tekcurvestat(4):
        tekcurvestat(6) ,2))./( tekcurvestat(3)-
        tekcurvestat(1));

% step (2)
% calculate the stress at radius r based on the
    Zwick data

```

```

% calculate the prefactor for the integral
pf=3*nu*(R^2-r^2)./(tekcurvestat(3)-tekcurvestat
    (1)); % Pa.m^2
% find and interpolate the value of the integral
    at time
% t2 = tekcurvestat(3)
y2 = interp1(zwickvalue(:,4),zwickvalue(:,9),
    tekcurvestat(3));

% check to see if we run out of time data
% if so then set y2 to the last point and issue a
    warning
if (isnan(y2))
    y2 = interp1(zwickvalue(:,4),zwickvalue(:,9),
        zwickvalue(roz,4)); % make y2 the last
        point available
    warning('Not_enough_late_Zwick_time_data_for_
        (%d,%d)',x,y);
end

% similarly for t1 = tekcurvestat(1)
y1 = interp1(zwickvalue(:,4),zwickvalue(:,9),
    tekcurvestat(1));
% check that we have zwick data in this timeframe
if (isnan(y1))
    y1=interp1(zwickvalue(:,4),zwickvalue(:,9),
        zwickvalue(1,4));; % make y1 the first
        point available
    warning('Not_enough_early_Zwick_time_data_for_
        (%d,%d)',x,y);
end

```

```

% so the stress integral of zwick data is
stresszwick = pf*(y2-y1);

% step (3)
% calculate the multiplier to calibrate the
    tekscan sensor
cal(x,y) = stresszwick/tekmeanstress;
if(offset(x,y)>1) cal(x,y)=0; end % remove all
    points with offsets
if(offset(x,y)<-0.1) cal(x,y)=0; end % remove all
    points with offsets

else % sensor is broken
    warning('Sensor_(%d,%d)_is_broken',x,y)
    cal(x,y) = 0;
end % for the if
end % for the y loop
end % for the x loop

% loop through all the sensors to remove any excessive gains
typical = mean(mean(cal));
for x=1:double(rows)
    for y=1:double(cols)
        if cal(x,y) > 2*typical
            cal(x,y)=0; % bad sensor
        end % if clause
    end % for the y loop
end % for the x loop

```

```

% plot the two shifted curves as a check
% plot(zwickvalue(:,4),(pf*(tekcurvestat(3)-tekcurvestat(1)))
    .* zwickvalue(:,8),tekpointdat(:,1),tekpointdat(:,2))

if(strcmp(pressure_unit{1}, 'PSI'))
    warning('Dodgy American units have been detected in
        Tekscan data - this has been rectified', 'NRC::BUSH')
end

% step (4) propagate the corected gains and offsets through
    all the
% tekscan data in frames

% loop through all frames
for f=1:frame_num
    % loop through rows
    for i=1:double(rows)
        % loop through columns
        for j=1:double(cols)
            calframes{f}(i,j) = (frames{f}(i,j)-offset(i,j))
                *cal(i,j);
        end % columns loop
    end % rows loop
end % frames loop

```

## Crossfilter.m

```

% crossfilter.m - smooth a matrix based on a cross shaped
% moving average kernel
% Adam & Julia, April 2005

```

```
function f=crossfilter(data)
% S is the frame
% f is the value returned

[rows cols]=size(data);

for i=2:rows-1
    for j=2:cols-1
        f(i,j)=1/8*(4*data(i,j)+data(i-1,j)
            +data(i+1,j)+data(i,j-1)+data(i,j+1));
    end end
```

# Appendix C

## Specification of the films

Table C.1: Properties of *DuPont FEP* fluorocarbon film

<b>Application</b>	<b>Food packaging</b> "Teflon" chemically inert food grade solvent resistant
<b>Dimensions</b>	
Thickness sheets	12.5, 25, 50, 75, 125, 190, 250, 375, 500, 750, 1500, 2300, 3125, 4750 $\mu\text{m}$
<b>Physical properties</b>	<b>Value</b>
Young's modulus	480 MPa
Specific gravity	2150 $\text{kg}/\text{m}^3$
Melting temperature	250 - 280 $^{\circ}\text{C}$

Table C.2: Properties of *APET 4500.00.000 Klöckner Pentaplst*

<b>Application</b>	<b>Food packaging</b> biocompatible ecologically disposable good barrier characteristics can be gamma sterilized recycling possible
<b>Dimensions</b>	
Thickness sheets	150 $\mu\text{m}$ to 800 $\mu\text{m}$
Width	max. 850 mm
Length	max. 1200 mm
coloring	as desired
<b>Physical properties</b>	<b>Value</b>
Young's modulus	2060 MPa
Specific gravity	1335 $\text{kg}/\text{m}^3$
Glass transition temperature	63 $^{\circ}\text{C}$
Melting temperature	250 $^{\circ}\text{C}$

Table C.3: Properties of *whey protein-glycerol films NIZO Food Research*

<b>Application</b>	food grade
<b>Dimensions</b>	
Thickness sheets	34 $\mu\text{m}$ to 186 $\mu\text{m}$
size	10 cm diameter
composition whey protein : glycerol	70:30 (series 1) and <b>65:35 (series 2)</b>
<b>Physical properties</b>	<b>Value</b>
Young's modulus	approx. 130 MPa (series 1) approx. 90 MPa (series 2)

# Appendix D

## Determination of the elastic modulus of the flexible film

The following equation gives the pressure profile in dependence of the radius  $r$ , a preset deflection  $\lambda$ , the flexural rigidity  $D$  (which is a function of the disk thickness  $h$ , the Young's modulus  $E$  and the Poisson ratio  $\nu$ ) and the disk radius  $R_0$ . This equation needs to be solved for the elastic modulus  $E$  when the pressure is known.

$$P(r) = \frac{64D\lambda^2((R_0^8 + 4R_0^6\lambda^2 - 2r^4\lambda^4 + 4r^2\lambda^6 + \lambda^8))}{(R_0^4 - 4r^2\lambda^2 + 2R_0^2\lambda^2 + \lambda^4)^3\sqrt{-4r^2 + \frac{(R_0^2 + \lambda^2)^2}{\lambda^2}}} + \frac{64D\lambda^2(R_0^4(4r^2\lambda^2 + 6\lambda^4) + 4R_0^2(2r^2\lambda^4 + \lambda^6))}{(R_0^4 - 4r^2\lambda^2 + 2R_0^2\lambda^2 + \lambda^4)^3\sqrt{-4r^2 + \frac{(R_0^2 + \lambda^2)^2}{\lambda^2}}} \quad (\text{D.1})$$

$$E = \frac{3P(R_0^4 - 4r^2\lambda^2 + 2R_0^2\lambda^2 + \lambda^4)^3\sqrt{-4r^2 + \frac{(R_0^2 + \lambda^2)^2}{\lambda^2}}(-1 + \nu^2)}{16h^3\lambda^2(R_0^8 + 4r^2R_0^4\lambda^2 + 4R_0^6\lambda^2 - 2r^4\lambda^4 + 8r^2R_0^2\lambda^4 + 6R_0^4\lambda^4 + 4r^2\lambda^6 + 4R_0^2\lambda^6 + \lambda^8)} \quad (\text{D.2})$$

With the help of equation D.1 the pressure necessary to deflect a disk with the following characteristics can be determined: 3 mm diameter, 75  $\mu\text{m}$  thickness, made from FEP, Poisson's ratio of 0.5, and an Young's modulus of 480 MPa, deflected to a  $\lambda$  of 0.112289 mm. Taking this pressure, i.e. 176 Pa, and assuming that it is sufficient to bend a 190  $\mu\text{m}$  thick disc of a more flexible material, the necessary elastic modulus

can be determined with the help of equation D.2, when  $r = 0$  m,  $R_0 = 1.5$  mm,  $\lambda = 0.112289$  mm  $h = 190$   $\mu\text{m}$ ,  $\nu = 0.5$ , and  $P(0) = 176$  Pa. A value of 30 MPa results from these conditions. Films of 30 MPa are very brittle and hard to get, hence, it was decided that the available 90 MPa, which was already an order of magnitude more flexible, were sufficient.

# Bibliography

- Agrawal, K., Lucas, P., Prinz, J., & Bruce, I. (1997). Mechanical properties of foods responsible for resisting food breakdown in the human mouth. *Archives of Oral Biology*, 42, 1–9.
- Association Francaise de Normalisation (1995a). *Controle de la qualite des produits alimentaires: Analyse sensorielle*. AFNOR. ISO 5492: 1992 (E/F) 3.51 Texture.
- Association Francaise de Normalisation (1995b). *Controle de la qualite des produits alimentaires: Analyse sensorielle*. AFNOR. ISO 5492: 1992 (E/F) 3.60 Grittiness.
- ASTM-D882-02 (2005). *D882-02 Standard test method for tensile properties of thin plastic sheeting*. ASTM International. Books of Standards.
- Batchelor, B. (1970). The stress system in a suspension of force-free particles. *Journal of Fluid Mechanics*, 41, 545–570.
- Bird, R., Stewart, W., & Lightfoot, E. (1960). *Transport Phenomena*. Wiley.
- Blake, J. (1972). A model for the micro-structure in ciliated organisms. *Journal of Fluid Mechanics*, 55, 1–23.
- Blake, J. & Chwang, A. (1974). Fundamental singularities in viscous flow. *Journal of Engineering Mathematics*, 8(1), 23–29.
- Booth, D., Earl, T., & Mobini, S. (2003). Perceptual channels for the texture of food. *Appetite*, 40, 69–76.

- Bourne, M. (2002). *Food Texture and Viscosity: Concept and Measurement*. Academic Press. 2nd.
- Bourne, M., Heath, R., & Hector, M. (2002). Food texture: Perception and measurement. *Conference Report of an International Workshop*. De Wageningse Berg, Wageningen.
- Brenner, H. (1964). The Stokes resistance of an arbitrary particle- IV. Arbitrary fields of flow. *Chemical Engineering Science*, 19, 703–2–727.
- Buckingham, E. (1914). *Physical Review*, IV, 345.
- Burbidge, A. & Servais, C. (2004). Squeeze flows of apparently lubricated thin films. *Journal of Non-Newtonian Fluid Mechanics*, 124, 115–127.
- Campanella, O. & Peleg, M. (1988). On food compression by soft machines. *Journal of Texture Studies*, 19, 39–50.
- Chanasattru, W., Corradini, M., & Peleg, M. (2002). Determination of practically significant differences in the sensorily perceived consistency of semiliquid foods. *Journal of Texture Studies*, 33, 445–460.
- Chiba, Y., Motoyoshi, M., & Namura, S. (2003). Tongue pressure on loop of transpalatal arch during delgution. *Orthodontics and Dentofacial*, (pp. 29–34).
- Conner, C. & Johnson, K. (1992). Neural coding of tactile texture: Comparison of spatial and temporal mechanisms for roughness perception. *The Journal of Neuroscience*, 12(9), 3414–3426.
- Cook, C., Hollowood, T., Linforth, R., & Taylor, A. (2003). Oral shear stress predicts flavor perception in viscous solutions. *Chemical Senses*, 28, 11–23.
- Corradini, M., Engel, R., & Peleg, M. (2001). Sensory thresholds of consistency of semiliquid foods: evaluation by squeezing flow viscometry. *Journal of Texture Studies*, 32, 143–154.
- Cutler, A., Morris, E., & Taylor, L. (1983). Oral perception of viscosity in fluid foods and model systems. *Journal of Texture Studies*, 14(4), 377–395.

- De Wijk, R., Engelen, L., & Prinz, J. (2003a). The role of intra-oral manipulation in the perception of sensory attributes. *Appetite*, 40, 1–7.
- De Wijk, R. & Prinz, J. (2005). The role of friction in perceived oral texture. *Food Quality & Preference*, 16, 121–129.
- De Wijk, R., van Gemert, L., Terpstra, M., & Wilkinson, C. (2003b). Texture of semi-solids; sensory and instrumental measurements on vanilla custard desserts. *Food Quality & Preference*, 14(4), 305–317.
- Deen, W. (1998). *Analysis of Transport Phenomena*. Oxford University Press.
- Dickie, A. & Kokini, J. (1983). An improved model for food thickness from non-newtonian fluid mechanics in mouth. *Journal of Food Science*, 48, 57–65.
- Dove, R., Fright, R., Martin, C., Price, B., Scally, K., & Remewan, R. (1994). Tracking jaw movement. *Medical & Biological Engineering & Computing*, 32, 584–588.
- Dunnewind, B., Janssen, A., van Vliet, T., & Weenen, H. (2005). Relative importance of cohesion and adhesion for sensory stickiness of semisolid foods. *Journal of Texture Studies*, 35, 603–620.
- Engelen, L. (2004). *A rough guide to texture; oral physiology and texture perception of semi-solids*. PhD thesis, VLAG Wageningen University Research Centre.
- Engelen, L., Prinz, J., & Bosman, F. (2002). The influence of density and material on oral perception of ball size with and without palatal coverage. *Arch. of Oral Biology*, 47, 197–201.
- Engelen, L., van der Bilt, A., Schipper, M., & Bosman, F. (2005). Oral size perception of particles: effect of size, type, viscosity and method. *Journal of Texture Studies*, 36, 373–386.
- Engelen, L., Wijk, R., Prinz, J., Janssen, A., van der Bilt, A., Weenen, H., & Bosman, F. (2003a). A comparison of the effects of added saliva, amylase and water on texture perception in semisolids. *Physiology & Behavior*, 78, 805–811.

- Engelen, L., Wijk, R., Prinz, J., van der Bilt, A., & Bosman, F. (2003b). The relation between salivary flow after different stimulations and the perception of flavor and texture attributes in custard desserts. *Physiology & Behavior*, 78, 165–169.
- Engmann, J., Servais, C., & Burbidge, A. (2005). Squeeze flow theory and applications to rheometry: a review. *Journal of Non-Newtonian Fluid Mechanics*, 132(1-3), 1–27.
- Finney, M. & Meullenet, J. (2005). Measurement of biting velocities at predetermined and individual crosshead speed instrumental imitative tests for predicting sensory hardness of gelatin gels. *Journal of Texture Studies*, 20, 114–129.
- Foegeding, E., Brown, J., Drake, M., & Daubert, C. (2003). Sensory and mechanical aspects of cheese texture. *International Dairy Journal*, 13, 585–591.
- Goh, S. & Charalambides, M. (2003). Large strain time dependent behavior of cheese. *Journal of Rheology*, 47, 701–716.
- Guinard, J.-X. & Mazzucchelli, R. (1996). The sensory perception and mouth-feel. *Trend in Food Science & Technology*, 7, 213–219.
- Harrison, M. & Hills, B. (1996). A mathematical model to describe flavor release from gelatine gels. *International Journal of Food Science & Technology*, 31, 167–176.
- Hartmann, C. & Delgado, A. (2003). Effects of pure elongational flow on particle aggregates. *Journal of Mechanics B/Fluids*, 22(2), 155–166.
- Hartmann, C., Höfer, C., Delgado, A., & Schantz, N. (2003). Deformation von Belebtschlammbecken in Dehnströmungen. *GVC/DECHEMA Fachbereich Umweltschutz und Umweltverfahrenstechnik (ed.)*, 5. GVC Abwasser Kongress, 79–86.
- Hartmann, C., Özmutlu, O., Petermeier, H., Fried, J., & Delgado, A. (2006). Analysis of the flow field induced by the sessile peritrichous ciliate operacularia asymmetrica. *Journal of Biomechanics*, (article in press).
- Hatch, J., Shinkai, R., Sakai, S., Rugh, J., & Paunovich, E. (2000). Determinants of masticatory performance in dentate adults. *Archives of Oral Biology*, 46, 641–648.

- Hayakawa, I., Watanabe, I., Hirano, S., Nagao, M., & Seki, T. (1998). A simple method for evaluating masticatory performance using a color-changeable chewing gum. *The International Journal of Prothodontics*, 11(2), 173–176.
- Henze, N. (1997). *Stochastik für Einsteiger*. Vieweg.
- Hiiemae, K. (2004). Mechanisms of food reduction, transport and deglutition. *Journal of Texture Studies*, 35, 171–200.
- Hiiemae, K., Heath, M., Heath, G., Kazazoglu, E., Murray, J., Sapper, D., & Hamblett, K. (1996). Natural bites, food consistency and feeding behaviour in man. *Archives of Oral Biology*, 41, 175–189.
- Hiiemae, K. & Palmer, J. (1999). Food transport and bolus formation during complete feeding sequences on foods of different initial consistency. *Dysphagia*, 14, 31–42.
- Hoebler, C., Devaux, M.-F., Karinthi, A., Belleville, C., & Barry, J.-L. (2000). Particle size of solid food after human mastication and in vitro simulation of oral breakdown. *International Journal of Food Sciences and Nutrition*, 51, 353–366.
- Hough, G., Martinez, E., & Contarini, A. (1988). Sensory and objective measurement of sandiness in dulce de leche, a typical argentine dairy product. *Journal of Dairy Science*, 73, 604–611.
- Imai, E., Hatae, K., & Shimada, A. (1995). Oral perception of grittiness: effect of particle size and concentration of the dispersed particles and the dispersion medium. *Journal of Texture Studies*, 26, 561–576.
- Jacobs, R., Wu, C.-H., Goossens, K., van Loven, K., & van Hees, J. and van Steenberghe, D. (2002). Oral mucosal versus cutaneous sensory testing: a review of the literature. *Journal of Oral Rehabilitation*, 29, 923–950.
- Johansson, R. & Olsson, K. (1976). Microelectrode recordings from human oral mechanoreceptors. *Brain Research*, 118, 307–311.

- Johansson, R., Trulsson, M., Olsson, K., & Westberg, K. (1988). Mechanoreceptor activity from human face and oral mucosa. *Experimental Brain Research*, 72, 204–208.
- Johansson, R. & Vallbo, A. (1979). Detection of tactile stimuli. Threshold of afferent units related to psychophysical threshold in the human hand. *Journal of Physiology*, 297, 405–422.
- Johnson, K. (2001). The roles and functions of cutaneous mechanoreceptors. *Current Opinion in Neurobiology*, 11, 455–461.
- Jones, C., Billington, R., & Pearson, G. (1994). The in vivo perception of roughness of restorations. *British Dental Journal*, 196(1), 42–45.
- Kilcast, D. & Clegg, S. (2002). Sensory perception of creaminess and its relationship with food structure. *Food Quality & Preference*, 13, 609–623.
- Kobayashi, K., Kumakura, M., Shinkai, H., & Ishii, K. (1994). Three-dimensional fine structure of the lingual papillae and their connective tissue. *Kaibogaku Zasshi*, 69, 624–635.
- Kullaa-Mikkonen, A. & Sorvari, T. (1985). A scanning electron microscopic study of the dorsal surface of the human tongue. *Acta anat.*, 123, 114–120.
- Lawless, H. & Heymann, H. (1999). *Sensory evaluation in food: principles and practices*. Springer.
- Leider, P. & Bird, R. (1974). Squeezing between parallel disks. I. Theoretical analysis. *Industrial Engineering & Chemistry Fundamentals*, 13(4), 7336–341.
- Lindinger, C. (2003). *Private communications*.
- Lucas, P., Prinz, J., Agrawal, K., & Bruce, I. (2004). Food texture and its effect on ingestion mastication and swallowing. *Journal of Texture Studies*, 35, 159–170.
- Malone, M., Appelaqvist, I., & Norton, I. (2003). Oral behavior of food hydrocolloids and emulsions. Part I. Lubrication and eposition considerations. *Food Hydrocolloids*, 17, 763–773.

- Mathmann, K., Kowalczyk, W., Petermeier, H., Eberhard, M., Baars, A., & Delgado, A. (2006). The impact of rheological properties on mouthfeeling caused by food. *Proceedings of the International Symposium on Food Rheology and Structure*, 4, 459–464.
- Mioche, L., Hiiemae, K., & Palmer, J. (2002). A postero-anterior videofluorographic study of the intra-oral management of food in man. *Archives of Oral Biology*, 47, 167–280.
- Mojet, J. & Köster, E. (2005). Sensory memory of food texture. *Food Quality & Preference*, 16, 251–266.
- Morrison, F. (2001). *Understanding Rheology*. Oxford University Press.
- Napadow, V., Chen, Q., van Weeden, J., & Gilbert, R. (1999). Intramural mechanics of the human tongue in association with physiological deformations. *Journal of Biomechanics*, 32, 1–12.
- Netter, F. & Kamina, P. (2004). *Atlas d'anatomie humaine*. Masson.
- Nicosia, M. & Robbins, J. (2001). The fluid mechanics of bolus ejection from the oral cavity. *Journal of Biomechanics*, 34, 1537–1544.
- Nirschl, H. (1994). *Mikrofluidmechanik - Numerische und experimentelle Untersuchung zur Umströmung kleiner Körper*. PhD thesis, Technische Universität München.
- Nirschl, H. (1997). *Partikelbewegungen in Scherströmungen ohne und mit Berücksichtigung des Einflusses angrenzender Wände*. PhD thesis, Technische Universität München.
- Ono, T., Hori, K., & Nokubi, T. (2004). Pattern of tongue pressure on hard palate during swallowing. *Dysphagia*, 19, 259–264.
- Oseen, C. (1974). *Hydrodynamik*. Leipzig.
- Palmer, J., Hiiemae, K., & Liu, J. (1997). Tongue-jaw linkages in human feeding: a preliminary videofluorographic study. *Archives of Oral Biology*, 42, 429–441.

- Paulsen, F. & Thale, A. (1998). Epithelial connective tissue boundary in the oral part of the human soft palate. *Journal of Anatomy*, 193, 453–467.
- Peyron, M.-A., Maskawi, K., Woda, A., Tanguay, R., & Lund, J. (1997). Effects of food texture and sample thickness on mandibular movement and hardness assessment during biting in man. *Journal of Dental Research*, 76(3), 789–795.
- Peyron, M.-A., Micoche, L., Woda, K., Tanguay, R., & Lund, J. (1996). Masticatory jaw movement recordings: a new method to investigate food texture. *Food Quality & Preference*, 7, 229–237.
- Pnueli, D. & Gutfinger, C. (1992). *Fluid Mechanics*. Cambridge University Press.
- Pollen, N., Daubert, C., Prabhasankar, P., Drake, M., & Gumpertz, M. (2005). Quantifying fluid food texture. *Journal of Texture Studies*, 35, 643–657.
- Prinz, J. & Lucas, P. (1995). Swallow thresholds in human mastication. *Archives of Oral Biology*, 40, 401–403.
- Prinz, J. & Lucas, P. (1997). An optimization model for mastication and swallowing in mammals. *Proceedings Biological Sciences. Royal Society*, 264, 1715–1721.
- Prinz, J. & Lucas, P. (2001). The first bite of the cherry: intra-oral manipulation in humans. *Journal of Oral Rehabilitation*, 28, 614–617.
- Pusey, P. (1991). in *Liquids, Freezing and the Glass Transition*. Elsevier, Amsterdam.
- Rao, N. (1996). Dimensional analysis, keeping track of length, mass, time... *Resonance*, (pp. 29–41).
- Roininen, K., Fillion, L., Kilcast, D., & Lahtenmaki, L. (2004). Exploring difficult textural properties of fruit and vegetables for the elderly in Finland and the United Kingdom. *Food Quality & Preference*, 15, 517–530.
- Roussel, N. & Lanos, C. (2003). Plastic fluid flow parameters identification using a simple squeezing test. *Applied Rheology*, 13, 132–141.

- Sakada, S. (1983). Physiology of mechanical senses of the oral structure. *Frontiers of oral Physiology*, 4, 1–32.
- Schlereth, T., Magerl, W., & Treede, R. (2001). Spatial discrimination threshold for pain and touch and human hairy skin. *Pain*, 92, 187–194.
- Segre, P., Meeker, S., Pusey, P., & Poon, W. (1995). Viscosity and structural relaxation in suspensions of hard-sphere colloids. *Physical Review Letters*, 75(5), 958–961.
- Smith, K. & Kier, W. (1989). Trunks, tongues, and tentacles: moving with skeletons of muscle. *American Scientist*, 77, 29–35.
- Stefan, J. (1874). Versuche über die scheinbare Adhäsion. *Sitzung Kaiserliche Akademie der Wissenschaften Mathematik Natur*, Wien, 69, 713–735.
- Steffe, J. (1992). *Rheological methods in food process engineering*. Freeman Press.
- Stokes, G. (1851). *Transactions Cambridge Philosophical Society*, 9, 8.
- Stone, M., Davis, E., Douglas, A., & Aiver, M. (2001). Modelling the tongue surface contours from CINE-MRI images. *Journal of Speech, Language, and Hearing Research*, 44, 1024–1040.
- Szczesniak, A. (2002). Texture is a sensory property. *Food Quality & Preference*, 13, 215–225.
- Takahashi, J. & Nakazawa, F. (1991a). Effects of viscosity of liquid foods on palatal pressure. *Journal of Texture Studies*, 22, 13–24.
- Takahashi, J. & Nakazawa, F. (1991b). Palatal pressure patterns of gelatin gels in the mouth. *Journal of Texture Studies*, 22, 1–11.
- Ten Cate, A. (1994). *Oral Histology. Development, structure and functions*. Mosby, St. Luis. 4th ed.
- Terpstra, M., Janssen, A., Prinz, J., de Wijk, R., Weenen, H., & van der Linden, E. (2005). Modelling of thickness for semisolid foods. *Journal of Texture Studies*, 36, 213–233.

- Timoshenko, S. & Woinoswky-Krieger, S. (1959). *Theory of plates and shells*. McGraw-Hill Book Company.
- Trulsson, M. & Essick, G. (1997). Low-threshold mechanoreceptive afferents in the human lingual nerve. *Journal of Neurophysiology*, 77, 737–748.
- Underwood, S., Taylor, J., & van Megen, W. (1994). *Langmuir*, 10, 3550.
- van Boven, R. & Johnson, K. (1994). The limit of tactile spatial resolution in humans: grating orientation discrimination at the lip, tongue, and finger. *Neurology*, 44, 2361–2366.
- van der Bilt, A., Weijnen, F., Bosman, F., van der Glas, H., & Kuks, J. (2001). Controlled study of EMG activity of the jaw closers and openers during mastication in patients with myasthenia gravis. *European Journal of Oral Sciences*, 109, 160–164.
- van Ruth, S., Grossmann, I., Geary, M., & Delahunty, C. (2001). Interactions between artificial and 20 aroma compounds in water and oil model systems. *Journal of Agricultural & Food Chemistry*, 49, 2409–2413.
- van Vliet, T. (2002). On the oral relation between texture perception and fundamental mechanical parameters for liquids and time dependent solids. *Food Quality & Preference*, 13, 227–236.
- Wansink, B. (2005). Consumer profiling and the new product development toolbox: a commentary on van Kleef, van Trijp, and Luning. *Food Quality & Preference*, 16, 217–221.
- Weipert, D., Tscheuschner, H.-D., & Windhab, E. (1993). *Rheologie der Lebensmittel*. Behr's.
- Wilkinson, C., Dijksterhuis, G., & Minekus, M. (2000). From food structure to texture. *Trends in Food Science & Technology*, 11, 442–450.
- Williams, P., Warwick, R., Dyson, M., & Bannister, L. (1998). *Gray's Anatomy*. Edinburgh London Melbourne New York: Churchill Livingstone.

- Wood, F. (1968). Psychophysical study on the consistency of liquid foods. *Society of Chemical Industry Monograph*, 27, 40–47.
- Wood, F. (1974). Approach to understanding creaminess. *Stärke*, 26(4), 127–130.
- Yates, N., Barigou, M., Fryer, P., & Moore, S. (2001). Squeeze flow of food pastes. *6th World Congress of Chemical Engineering*, Melbourne, Australia, 23–27 September.
- Zima, B., Kowalczyk, W., Hartmann, C., & Delgado, A. (2005). Influence of velocity distribution in the multiphase flow on the building of aerobic granules in a sequencing batch reactor (SBR). *Proceedings in Applied Mathematics and Mechanics PAMM*, 5, 603–604.

# Julia Annette Strassburg

## PERSONAL INFORMATION

---

- Date of Birth: 09 July 1978
- Nationality: German
- Place of Birth: Hannover, Germany
- Marital Status: Single

## EDUCATION/WORK EXPERIENCE

---

- since 10/2006 Nestlé Product Technology Center Orbe (CH), Coffee Department
- 2003/2006 PhD thesis (scholarship) at the Nestlé Research Center Lausanne, (CH)  
Supervised by the Technical University of Munich, Weihenstephan, (D)  
Chair of Fluid Dynamics  
  
Title: “Mechanical Effects in Human Oral Texture Perception”
- 1998-2003 Engineering degree in “Technology and Biotechnology of Foods  
(Dipl.-Ing.)” Technical University of Munich, Weihenstephan  
Diploma work at the Nestlé Product Technology Center York, (GB)  
  
Title: “Influence of Tempering, Cooling Tunnel Time and Storage Temperature  
on the Crystallization of Chocolate”

## INTERNSHIPS/STUDENT JOBS

---

- 2002 Staatliche Molkerei Weihenstephan (dairy)  
Student job (1 semester)
- 2001 Chair of Economics, Technical University of Munich, Weihenstephan  
Student job (1 semester)
- 2001 Nestlé Chokoladenwerk (chocolate factory), Hamburg (6 weeks)  
Trainee
- 2000 Frankenheim Alt Privatbrauerei (brewery), Neuss (5 weeks)  
Trainee
- 1999 Döhler Natural Food Ingredients, Darmstadt (4 weeks)  
Trainee
- 1998 Döhler Natural Food & Beverage Ingredients, Darmstadt (13 weeks)  
Trainee

## LANGUAGES

---

- German: mother tongue
- English: fluent
- French: fluent
- Spanish: basic
- Latin

## STAYS ABROAD

---

- Since May 2003 PhD thesis at Nestlé in Lausanne, Switzerland
- 2002-2003 Diploma work at Nestlé in York, England (6 months)
- 1996 Student exchange, St. Malo, France (3 weeks)
- 1994-1995 High School Year in Kalida, Ohio, USA (1 year)  
Graduation with official American High School diploma
- 1991-1993 Student exchange, Tacoma, Washington, USA (4 weeks)  
Student exchange, Brighton, England (3 weeks)  
Student exchange, Bournemouth, England (3 weeks)

## CONFERENCES/WORKSHOPS

---

- International Symposium on Food Structure and Rheology ISFSR 06,  
“Geometrical resolution limits in the human mouth” (Oral presentation)  
Zürich (CH), 20-23<sup>rd</sup> February 2006
- German Engineering Association, Annual meeting of the Association of Chemical and  
Process Engineers, Department of Food Process Engineering,  
“Sandigkeitsempfindung im Mund –ein fluidmechanisches Modell im Mikromaßstab”  
(Oral presentation)  
Berlin (D), 7-9<sup>th</sup> March 2005
- 1<sup>st</sup> International Workshop on Materials & Sensations,  
“Mechanics of Oral Texture Perception” (Oral presentation)  
Pau (F), 27-29<sup>th</sup> October 2004

## PUBLICATIONS

---

- Strassburg, J., Ziegleder, G., Beckett, S. When are chocolates really finished?  
*New Food*
- Strassburg, J., Hartmann, C., Burbidge, A., Delgado, A. Geometrical resolution limits  
and detection mechanisms in the oral cavity. *Journal of Biomechanics*  
(submitted)
- Strassburg, J., Burbidge, A., Hartmann, C., Delgado, Mechanisms and sensitivity of  
object dimensional perception through human touch. *Journal of Comparative Physiology A*  
(submitted)